Durham E-Theses

Optical polarimetry of star forming regions

Gledhill, Timothy Michael

How to cite:

Gledhill, Timothy Michael (1987) *Optical polarimetry of star forming regions*, Durham theses, Durham University. Available at Durham E-Theses Online: http://etheses.dur.ac.uk/6757/

Use policy

Optical Polarimetry of Star Forming Regions

Timothy Michael Gledhill, B.Sc.

A thesis submitted to the University of Durham
for the degree of Doctor of Philosophy

Physics Department December 1987

Optical Polarimetry of Star Forming Regions

T.M. Gledhill

The work presented in this thesis details the polarimetric investigation of nebulosity associated with low mass pre-mainsequence (PMS) stellar objects. Three regions of on-going star formation are considered, specifically, the Haro 6-5 and the HL/XZ Tau systems—both associated with dark clouds in the Taurus complex—and the PV Cephei nebulosity near NGC7023. The work is based on CCD observations at optical wavelengths using the Durham Imaging polarimeter.

Theories of PMS stellar evolution have developed rapidly over the last three years in tandem with observational discoveries and so a review of current ideas, necessary for the interpretation of the data, is given. The viability of the Davis-Greenstein grain alignment mechanism in regions of star formation is also briefly examined.

In each region, the imaging observations suggest bipolarity in the optical structure of the nebulosity and the polarimetric data are used to determine the locations of the illuminating sources. Evidence is found for the association of circumstellar discs of obscuration with the PMS objects Haro 6-5A (FS Tau), Haro 6-5B, HL Tau and PV Cephei. In each case the polarimetric data suggest that the local magnetic field has played an important role in the evolution of the star and the circumstellar material. Examination of the source region polarisation maps suggests that at least one of the objects considered is surrounded by a dust grain-aligning magnetic field which has a predominantly toroidal geometry in the plane of the circumstellar disc and the implications for current theories of outflow acceleration and cloud evolution are discussed.

Contents Page

Figures

Tables

With the exception of the 1984 Jun and 1984 Aug PV Cephei observations, all the data presented in this thesis were recorded by the author at the Wise Observatory, Israel and the Isaac Newton Telescope, La Palma between 1984 Nov and 1987 Jan. With the exception of the 1984 Jun PV Cephei observations, all data reduction is by the author. The Wise observatory data presented in chapter four have been published as Gledhill *et al.* 1986 and outlined in conference proceedings as Scarrott *et al.* 1985 *'Cosmical Gas Dynamics'* and Scarrott *et al.* 1986. The data presented in chapter 6 have been accepted for publication as Gledhill *et al.* 1987 and have also been outlined in conference proceedings as Scarrott *et al.* 1986 and Scarrott *et al.* 1987d. In each case, the analysis and final interpretation of the data in this thesis is the author's own.

Chapter 1

Star Formation in the Galaxy

In order to investigate the process of star formation (SF), the conditions under which it occurs and the mechanisms responsible for its induction, a knowledge of the nature and distribution of star-forming material on a Galactic scale is required. It is known that stars form within the confines of molecular clouds and associations of molecular clouds (often called giant molecular clouds or GMCs). Hence, although the distribution of the total gas content of the interstellar medium (ISM) is of considerable interest, this discussion will concentrate on the molecular component of the ISM which is expected to be a reliable tracer of potential SF.

1.1 The Distribution of Molecular Material

The most abundant element in the Galaxy is hydrogen and, therefore, the molecular phase of the ISM is dominated by H_2. Extinction by interstellar dust considerably limits the horizon of optical observations in the plane of the Galaxy, requiring any survey on a Galactic scale to be conducted in the radio frequency regime. The distribution and mass of atomic hydrogen (HI) in the Galaxy is well documented and may be inferred directly from measurement of the 21cm line. However, the molecular transitions of the H_2 molecule are forbidden to occur by electric dipole radiation and so H_2 has no detectable radio line. The quantitative detection of H_2 must then necessarily proceed by a more circuitous route. An indirect assessment of the presence of H_2 is possible by means of the carbon monoxide (CO) molecule which exists in great abundance in all molecular clouds.

The J= 1 → 0 lowest rotational transition of CO at 2.6mm is readily detectable and provides good angular resolution with moderately sized telescopes. The 2.6mm line is collisionally excited by H_2 for a threshold in kinetic energy which is usually assumed to correspond to densities in the range $n(H_2) \geq 100 \rightarrow 300 \text{cm}^{-3}$ (Scoville and Solomon 1974). The threshold for the effective self-shielding of H_2 corresponds to a total gas density of $n(HI) + 2n(H_2) > 100 \text{cm}^{-3}$ (Solomon and Wickramasinghe 1969) and so the CO line is expected to be an excellent tracer of H_2 in molecular clouds.

The indirect nature of this approach necessitates the introduction of various assumptions concerning the relationship between the integrated CO intensity and the column density of H_2. It is thought that these two quantities may be related by a 'constant' of proportionality, the determination of which would render the two distributions directly comparable. However, this seemingly simple assumption represents, in fact, a considerable bone of contention and a serious impediment to progress in the understanding of the nature of molecular clouds.

1.1.1 The Conversion from CO to H_2

It is generally assumed that the CO integrated intensity and the column density of H_2 are related by a 'constant' of proportionality such that

$$N(H_2) = C \int T_A^{12} dv \qquad (1.1)$$

where T_A^{12} is the antenna temperature for ^{12}CO emission, v is velocity and C is a constant with units of molecules $\text{cm}^{-2}\text{K}^{-1}$ $(\text{km s}^{-1})^{-1}$.

The first problem inherent in this assumption is the determination of C. The values that have been adopted for this parameter over the last few years vary considerably reflecting, perhaps, the different arguments employed in their derivation. A second and potentially more serious problem is that C is probably not constant at all. There is a growing body of evidence to suggest that C is at least dependent on Galactocentric radius and is most likely a complicated function of local physical parameters.

Several different methods have been employed in the estimation of C both locally and elsewhere in the Galaxy and include measurements at X-ray, Gamma-ray and IR wavelengths as well as estimates from visual extinction and application of the virial theorem. A review of such techniques

Source	C $(cm^{-2}K^{-1}km^{-1}s)$	Region
Bhat *et al.* (1986)	$\approx 0.25 \times 10^{20}$	Galactic centre
"	$\leq 0.9 \times 10^{20}$	6kpc radius
"	$1 \times 10^{20} \rightarrow 2 \times 10^{20}$	10kpc radius
Lebrun and Huang (1984)	1.1×10^{20}	locally
Blitz and Shu (1980)	1.8×10^{20}	everywhere
SSS	3.6×10^{20}	everywhere

Table 1.1: Some values of the parameter C defined by Equation 1.1 indicating the region of the Galaxy in which they are assumed to hold. For a more extensive tabulation see Bhat *et al.* (1986) and SSS.

is given by Bhat *et al.* (1986) who suggest that they are all consistent with a local value of C between 1×10^{20} and 2×10^{20}. They discuss the evidence for a decrease in this value to $\approx 0.25 \times 10^{20}$ at the Galactic centre. These figures are consistently lower than that adopted by Sanders, Solomon and Scoville 1984 (hereafter SSS) who assume C to be constant throughout the Galaxy (Table 1.1).

If C is assumed to be constant throughout the Galaxy, then the discrepant values will merely scale the H_2 distribution. However, if C is positionally dependent then the form of the distribution will change. In both cases, estimates of the mass of H_2 can vary radically but, more importantly, the ratio H_2/HI will remain uncertain. It will be seen later that this ratio is a crucial factor in the interpretation of the lifetimes and formation mechanisms of molecular clouds. It follows, therefore, that caution must be exercised when interpreting the distribution of CO emission in the Galaxy in terms of the abundance of H_2

1.1.2 The Radial Distribution

In an early survey of CO emission in the plane of the Galaxy, Scoville and Solomon (1975) came to the striking conclusion that the molecular gas is concentrated into a ring like structure, symmetric about the Galactic centre, between radii of 5 and 8 kpc. Since the width of this molecular annulus is considerably greater than the thickness of a spiral arm, this result infers that molecular material is not confined to the spiral arms and so must

have a significant presence in the inter-arm regions. Since 1975, extensive surveying of the Galaxy in CO (Burton and Gordon 1978 (BG); Cohen *et al.* 1980; SSS) has confirmed the earlier results and extended them to three dimensions, providing information on the distribution in z (height above the plane of the Galaxy). The main conclusions from these surveys concerning the distribution of molecular material are outlined below.

- There is a general agreement that the radial distribution of the surface density of CO shows a dominant peak in the nuclear region of the Galaxy and a subsidiary peak at 6kpc corresponding to a molecular ring or annulus. The azimuthally averaged radial CO distribution obtained by BG is shown in Figure 1.1. The half maxima of the ring lie at 4 and 8 kpc, with the inner edge being more sharply defined than the outer (BG). Bania (1977) shows that the depletion of CO extends inwards from the inner edge of the ring to a radius of $\approx$ 400pc. These molecular data are seen to contrast with the results of 21cm line studies (*e.g.* Gordon and Burton 1976) which show the radial distribution of atomic hydrogen (HI) to be rather flat over a large region of the Galaxy ($4 < R < 13$kpc). The degree of contrast depends on the value adopted for C (see Figure 1 of Bhat *et al.* 1985 and Table 1.2 below). BG directly compare the radial abundances of CO and HI and note that, although the distributions are largely disparate, both HI and CO appear to be depleted in the region $0.4 < R < 4$kpc suggesting that this region exhibits a paucity of all gas.

- The survey of SSS indicates that more than 90 per cent of the total mass of H_2 exists within the solar radius ($R < 10$kpc) compared with only 30 per cent in the case of HI (Table 1.2) and that very little of the H_2 exists outside a radius of 12kpc. As mentioned previously, there is a body of evidence supporting consistently lower (and variable) values of C than the (fixed) value adopted by SSS. The use of such lower values does affect the H_2 distribution (as can be seen from Table 1.2).

- SSS conclude that the Galactic nucleus appears to be almost exclusively molecular by a factor of 50 or so. This factor is drastically reduced when the value for C suggested by Bhat *et al.* (1986) is used. More important still is the reduction in the ratio of H_2 to HI in the molecular ring region.
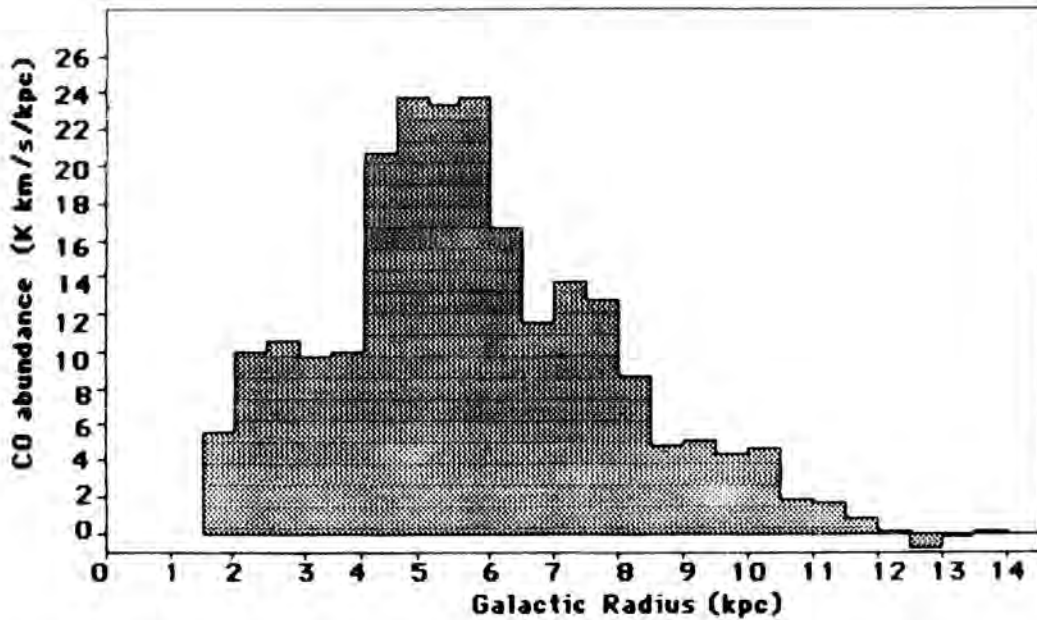
Figure 1.1: The radial distribution of azimuthally averaged CO intensity from Burton and Gordon 1978.

- SSS suggest that H_2 may be 6 times more abundant than HI in the molecular ring region. Using the lower value of C however allows H_2 and HI to be in roughly equal abundance (Table 1.2). An equal abundance would be in agreement with the conclusions of Blitz and Shu (1980) who also reassessed the value of C.

- SSS suggest that the scale height of the z distribution of molecular material is very similar to the z distribution of young stars, implying that young stars are still closely associated with the material from which they formed. However, the distribution of HI with z appears to be more diffuse, perhaps extending a factor of 2 further out of the Galactic plane.

Although the existence of molecular material in the inter-arm region has been established, this result does not preclude the possibility of spiral structure in the distribution. The commonly accepted delineators of the spiral arms are young high mass stars and stellar associations and HII regions. An indication of the degree to which spiral structure exists in the reservoir

Mass	R (kpc)			Total (M_T)
	0-1.5	1.5-10	10-16	
M(HI)	$1 \times 10^7 M_\odot$	$0.9 \times 10^9 M_\odot$	$2 \times 10^9 M_\odot$	$3 \times 10^9 M_\odot$
M/M_T (HI)	0.3%	30%	67%	100%
C^1	3.6	3.6	3.6	
M(H_2)	$0.5 \times 10^9 M_\odot$	$2.7 \times 10^9 M_\odot$	$0.3 \times 10^9 M_\odot$	$3.5 \times 10^9 M_\odot$
M/M_T (H_2)	14%	77%	9%	100%
M(H_2)/M(HI)	50	3.0	0.15	1.17
C^2	0.25	1.0	1.5	
M(H_2)	$3.5 \times 10^7 M_\odot$	$7.6 \times 10^8 M_\odot$	$1.3 \times 10^8 M_\odot$	$9.3 \times 10^8 M_\odot$
M/M_T (H_2)	4%	82%	14%	100%
M(H_2)/M(HI)	3.5	0.8	0.07	0.3

[1](SSS)

[2](Bhat *et al.* 1986, selected from the range specified in Table 1.1)

Table 1.2: The total disc mass of atomic and molecular hydrogen at $R = 0 \rightarrow 16$kpc (adapted from Sanders, Solomon and Scoville 1984). The total and fractional masses of H_2 and the ratio of H_2 to HI are shown for two sets of values of C.

of molecular material out of which these stars form is important, therefore. in determining the nature of molecular clouds and GMCs in general and star forming clouds in particular and in understanding the transition from molecular cloud to star.

1.1.3 Spiral Structure

Does spiral structure exist in the distribution of molecular material in the Galaxy? The question as posed allows one of three outcomes; either molecular gas is confined to the spiral arms, it exists both in the spiral arms and in the inter-arm regions or it exists only in the inter-arm regions. Since young O stars and attendant HII regions are known to be tracers of spiral arm structure, this must, to some extent, be true of their predecessors—molecular clouds. Hence the last postulate of the three can be discarded. If molecular clouds are not confined to the spiral arms and have a much wider distribution, then theories concerning their formation and lifetimes will consequently be affected.

Scoville, Solomon and Sanders (1979) plotted the results of their 'broad latitude' CO survey in Galactocentric coordinates of radius and azimuth and noted that "most of the clouds cannot be situated within a regular pattern of spiral arms". They did, however, find an excellent correlation between GMCs and HII regions, with almost every HII region having a detectable molecular component associated with it. The reverse is not true, since the number of molecular clouds greatly exceeds that of HII regions (by at least a factor of 50). The conclusion from this is that molecular clouds (whether giant or otherwise) exist both in the arm and inter-arm regions.

BG tentatively suggest that there is "some higher order arrangement of dark clouds within the Galaxy, be it simple clustering or a large scale design such as spiral structure" but this is certainly not evidence for confinement to the spiral arms.

Cohen *et al.* (1980) adopt a more extreme position and conclude that CO and molecular clouds are, in fact, excellent tracers of spiral arms. They suggest that little of the inter-arm material is in the form of molecular clouds which must, therefore, be disrupted in some way as they leave the spiral arm regions.

Sanders, Scoville and Solomon (1985) compare the distribution of 315

clouds with diameters > 10pc with the locations of radio HII regions. They conclude that the population of molecular clouds may be resolved into two components according to core temperature. The 'warm' clouds appear closely associated with HII regions (and hence with spiral structure) whereas the 'cold' clouds (constituting about $\frac{2}{3}$ of the total sample) are much more widely distributed. This suggests that, in general, the inter-arm clouds are colder than those seen in the spiral arms and (therefore) more difficult to detect, introducing a possible observational bias towards clouds in the arms.

Although the issue is confused to some degree, the consensus of opinion is that molecular material (clouds) exists both in the arm and inter-arm regions with perhaps a greater abundance in the arms than between them.

1.1.4 CO Observations of M51

The nearly face on Sc galaxy M51 shows pronounced spiral structure with dust lanes concentrated at the inner edges of the spiral arms. Using a 33 arcsec beam, Rydbeck *et al.* (1985) concluded that there is a qualitative agreement between the distribution of CO emission and that of Hα in M51. They also suggest that there is a 20 per cent enhancement of CO emission in the spiral arm regions (over the inter-arm regions).

In a 7 arcsec resolution interferometric study of M51, Lo *et al.* (1987) find an excellent correlation between the CO emission and the radio continuum ridges (which they interpret as indicators of shock regions associated with spiral density waves). They show that the distribution of molecular emission (and hence, presumably, discrete molecular clouds) closely follows the optical spiral arm structure, appearing especially coincident with the trailing (dusty) edges of the inner spirals. Assuming that the velocity dispersion of the gas inside and outside the arms is the same and that the column density of H_2 is proportional to the integrated CO intensity, Lo *et al.* infer from their measurements that the ratio of $N(H_2)$ in the arms to that between the arms lies in the range $3 \rightarrow 15$.

In order to explain the observation of molecular clouds in the inter-arm regions, both Rydbeck *et al.* (1985) and Lo *et al.* (1987) advocate the theory of cloud formation by coagulation and collisional growth in these regions (§1.2.2.1)

1.2 Molecular Clouds

The distribution of molecular material, described in the previous section, is usually interpreted as the distribution of molecular clouds. This interpretation is supported by the observations of Sanders *et al.* (1985) of discrete CO cloud features which indicate that the radial distribution of cloud number density is very similar to that of emissivity.

The term 'Giant Molecular Cloud' is used to label clouds varying in size from 5 to > 100pc. It will be seen shortly that arguments concerning the formation of molecular clouds do hinge critically upon the size and mass of clouds that can be formed and so a more accurate parameterisation of large, small or typical GMCs is advantageous.

1.2.1 The Cloud Size and Mass Distributions

One of the problems in the determination of the properties of discrete molecular clouds lies in the resolution of the near-far distance ambiguity. Sanders, Scoville and Solomon (1985) combat this impediment by constructing a sample consisting of clouds lying well away from the Galactic plane. Their sample may, therefore, be more representative than most. These authors analysed 80 clouds with diameters > 10pc lying in a wedge shaped sector of the Galaxy. The lower size limit of $D > 10$pc means that all of the clouds considered lie within the broad category of GMC and no information is given on small low mass clouds which are expected to be sites of low mass SF. These authors find that their size distribution can be adequately fitted by a power law of the form $N(D) = aD^b$ with $a = 1.34 \times 10^{4.1\pm0.3}$ and $b = -2.3 \pm 0.2$ where N is the number of clouds of diameter D. These parameters appear to be in agreement with previous determinations of the size distribution which suggest that $-2.6 > b > -3.3$ for $15 < D < 95$pc (Sanders *et al.* 1985). Similar calculations concerning the mass distribution of molecular clouds suggest that more than half of the total cloud mass resides in clouds with diameters greater than 48pc. Also (according to Sanders *et al.* 1985) more than 80 per cent of the molecular mass resides in clouds with mass greater than $10^5 M_\odot$ for a sample of clouds with $D > 10$pc and that 85 per cent of the H_2 in the inner Galaxy exists in the form of clouds with a diameter > 22pc and mass > $10^5 M_\odot$, which are defined as GMCs. Assuming a population of GMCs of mass $5 \times 10^5 M_\odot$, the

upper limit on their number will lie in the range 1600 → 6400, depending on the value accepted for the total mass of H_2 in the inner Galaxy. In a theoretical simulation Kwan (1979) infers that 70 per cent of the mass is in clouds with $10^4 < M < 2 \times 10^5 M_\odot$.

Such a population of large and massive clouds in the Galaxy will clearly dominate the distribution of interstellar matter and hence the process of SF.

1.2.2 The Formation of Molecular Clouds

The identification of a widespread disc population of large molecular clouds places severe constraints on theories attempting to explain their formation. Closely allied to the formation debate is the discussion on how long, once induced, the GMC phase lasts for, *i.e.* what is the lifetime of a GMC (t_{GMC})? If GMCs form in the Galactic spiral shock, then for them to be observed in the inter-arm regions they must have a lifetime greatly in excess of previous estimates ($> 10^8$yrs instead of $\sim 10^7$yrs). If we cannot countenance such a long lifespan (perhaps because of the problems in supporting the cloud against gravitational contraction) then we must conclude that GMCs are already in existence in a dense phase when the Galactic shock passes by. The free-fall timescale for GMCs is usually taken to be $\sim 10^6$yrs but t_{GMC} may be much larger than this. An upper limit can be defined by the time it would take for all of the observed interstellar material in the form of GMCs to be converted into stars. Assuming a SF rate of 5 → $10M_\odot$yr^{-1} this could be as large as 10^9yrs so that $10^6 < t_{GMC} < 10^9$yrs. For GMCs to exist between the spiral arms they must either exist for longer than an arm crossing time ($\approx 5 \times 10^7$yrs) without undergoing high mass SF or form frequently in the inter-arm region.

1.2.2.1 Formation by Coagulation

Kwan and Valdes (1983) suggest that GMCs are formed by mergers during collisions between smaller molecular clouds. They show that as a distribution of molecular clouds passes through a spiral gravitational potential of amplitude 5 per cent, the rate of growth of massive clouds (GMCs) near the potential minimum is enhanced by a factor of between 3 and 6 (de-

pending on the parameters of the initial distribution). Although clouds will form in an axisymmetric potential, the presence of the spiral potential seems to have a major effect on the high mass ($> 10^5 M_\odot$) end of the cloud mass spectrum, promoting the formation of large GMCs. According to this scheme, molecular clouds can form and grow by coagulation in the inter-arm regions, but the coagulation into the largest structures (GMCs) occurs predominantly in the spiral arms. The lifetime of a GMC includes the time taken to form the cloud from smaller clouds as well as the time for which the formed cloud is expected to exist. Kwan and Valdes note that the time needed for a cloud to grow from $10^3 M_\odot$ to $10^5 M_\odot$ is $\approx 6 \times 10^7$yrs. If the GMCs are produced primarily in the spiral potential minima then the time for which they would be expected to exist can be estimated from the fraction of the ISM in molecular form. However, it has been seen that this fraction varies dramatically depending on the assumed value of C and probably also depends on Galactic radius.

Lo *et al.* (1987) interpret their CO observations of M51 to suggest that GMCs are mainly confined to the spiral arms with the inter-arm regions populated by a distribution of smaller molecular clouds. They conclude that GMCs form from the coalescence of smaller clouds in the presence of the Galactic spiral shock (in agreement with Kwan and Valdes 1983) and are then re-dispersed upon leaving the spiral arm. If such a re-dispersal does take place, then the maximum lifetime of a GMC will be the spiral arm transit time which is $\approx 5 \times 10^7$yrs, although it is dependent upon the spiral pattern speed and galactic radius. This value under estimates that suggested by Kwan and Valdes (1983). However, if the clouds have already reached a massive stage before they enter the spiral region, then their lifetime may be increased to $\approx 10^8$yrs. The most probable method of dispersal is the disruptive effect of massive O SF. Disruption in the form of a single catastrophic event (*e.g.* a supernova explosion) is unlikely in view of the enormous gravitational binding energies of GMCs. It is more likely that a GMC would disperse whilst undergoing a sequence of massive O SF over a period of $\sim 10^7$yrs or so (Blitz and Shu 1980).

1.2.2.2 Formation in Parker Instabilities

Blitz and Shu (1980) argue against the formation of GMCs by coagulation, mainly on the basis that it takes too long. On the timescales necessary for the accumulation of masses in excess of $10^5 M_\odot$ ($\approx 6 \times 10^7 \text{yrs}$) the cloud may have been seriously disrupted by massive SF. The coagulation theory does not prevent the formation of GMCs in the inter-arm regions and, since little high mass SF is observed outside the spiral arms, would allow GMC lifetimes in excess of 10^8yrs in the absence of dissociative forces. It is difficult to see how a cloud of mass $> 10^5 M_\odot$ could be supported against gravitational contraction over a period of $> 10^8 \text{yrs}$.

Instead, Blitz and Shu (1980) argue in favour of the formation of GMCs from atomic material behind the Galactic spiral shock. They propose that the development of Parker instabilities (magnetic Rayleigh-Taylor instabilities) in the Galactic magnetic field in these shock regions will lead to the formation of GMCs. This mechanism for cloud formation is described by Mouschovias *et al.* (1974). However, the Parker instability mechanism suffers from two main objections. Firstly, it is expected that at the high temperatures (10^6K) and low densities (1cm^{-3}) of the uncondensed ISM, the hydromagnetic waves associated with the Parker instability will be incapable of effecting significant density changes (Shu 1978). Secondly, the restriction of GMC lifespan ($\approx 5 \times 10^7 \text{yrs}$) implies that the maximum proportion of the ISM in molecular form is 30 per cent. Although this fraction is subject to great uncertainty, a value of 30 per cent would seem to be an underestimate for the inner Galaxy ($R < 10 \text{kpc}$) at least (Table 1.2).

1.2.3 Summary of Arguments

The arguments presented above in §1.2.2.1 and §1.2.2.2, despite innate differences, allow the imposition of constraints on cloud formation and destruction and speculation on a common scenario for these processes. It would appear that (at least) the largest molecular clouds are more or less confined to the spiral arms as defined by massive SF. In the spiral arm regions these large clouds form either by orbit crowding-aided coagulation or by Parker instability-aided contraction. They may only last for the period of the arm crossing time ($\approx 5 \times 10^7 \text{yrs}$) after which they may then be dispersed—possibly due to the disruptive effects of high mass SF. Any

resultant disrupted fragments or smaller molecular clouds could then exist in the inter-arm regions for $> 10^8$yrs until they again pass into a spiral arm and the process is repeated. However, the theory of formation in Parker instabilities (and other theories requiring GMCs to be formed in and confined to the spiral arms) could run into difficulty if it is found that large GMCs— as defined by the cloud size distribution—do exist in the inter-arm regions. Coagulation theory (as presented, for example, by Kwan and Valdes 1983) on the other hand does not suffer from this difficulty since it in no way precludes the existence of large GMCs between the spiral arms. It merely stipulates that the probability of observing such an object in a given volume of space is greater for a volume within a spiral arm than for one without. It seems more likely, though, that the inter-arm cloud population consists mainly of smaller objects less prone to the ravages of high mass SF. These clouds would presumably undergo low mass SF and evolve relatively quiescently.

The observed SF rate requires that most observed molecular clouds must be supported against gravitational collapse for a large proportion of their lifetime. If this support is facilitated with the aid of the cloud's embedded magnetic field, then it would be easier to envisage such support in the case of small clouds rather than large. Upon entering the spiral arms, the clouds may coalesce and initiate high mass SF.

The details of the internal structure of large clouds are not clear although it is certain that they will not consist of single condensations with simple radial density distributions. It has been suggested that large molecular complexes are hierarchically structured and consist of several scales of size and density, each exhibiting a high density contrast and low volume filling factor to the preceeding scale. Falgarone and Puget (1986) consider such a molecular complex and discuss the energy transfer between different structural levels in the complex concluding that the transfer of cloud orbital energy to internal random cloud kinetic energy *via* interlinking cloud magnetic field lines may be important in supporting the cloud.

1.3 Star Formation in Molecular Clouds

The discussion of the previous section suggests a differentiation in the way large and small molecular clouds are formed. Such a 'bimodal' approach to the distribution of star forming material would perhaps be expected to manifest itself in the process of SF itself. Optical observations of clouds in the solar neighbourhood indicate that plenty of 'low mass' SF is occurring but comparatively little evidence of high mass SF is seen. Also, since there are up to 6000 GMCs in the Galaxy but only about 100 known HII regions, high mass SF appears to be a very selective process.

This work is concerned with the PMS activities of low and intermediate mass stars (*e.g.* T Tauri stars at a few solar masses). These objects may form more or less 'spontaneously' as all or part of a molecular cloud becomes gravitationally unstable as a natural consequence of its isolated (on a Galactic scale) evolution. If this is the case, then these stars should form anywhere where there is a sufficient abundance of H_2.

The treatment of cloud collapse has been attempted using models of varying sophistication, the simplest case being that of a non-rotating cloud containing no magnetic flux. The inclusion of a cloud magnetic field necessarily complicates the calculation and also dictates that the cloud collapse be non-isotropic. If the magnetic cloud is allowed to rotate about some axis then the analytical solution becomes intractable except for the most simple and symmetric geometries. However, it is only at this level of complexity that the cloud model becomes realistic and can be expected to yield information on the fundamental nature of SF.

These factors and the effect they have on the evolution of a molecular cloud will now be discussed independently.

1.3.1 Isotropic Cloud Collapse

Consider an isolated spherical non-rotating and non-magnetic molecular cloud under a constant external pressure P_0. The cloud has access to stable equilibrium states for all values of P_0 less than some critical value P_c. When $P_0 > P_c$ the cloud collapses, that is, it contracts beyond the last available equilibrium state.

For such a system, the virial theorem equation is (Spitzer 1978)

$$4\pi R^3 P_0 = \frac{3MkT}{\mu} - \frac{3GM^2}{5R} \tag{1.2}$$

with R, M, and T the radius, mass and temperature of the cloud. An increase in the external pressure, P_0, causes the cloud to contract *i.e.* R decreases. Since the cloud is assumed to be isothermal the internal pressure term is constant and for small enough R (high enough P_0) the gravitational term dominates. When this happens, no further equilibrium states are available and so the cloud must collapse. This condition occurs for a critical external pressure P_c where

$$P_c = \frac{1.4(kT/\mu)^4}{G^3 M^2} \tag{1.3}$$

(Spitzer 1968). It is also easy to show from Equation 1.2 that the collapse condition corresponds to a critical mass M_c. If T is constant, then $(kT/\mu)^4 = C^8$ where C is the isothermal sound speed and

$$M_c = 1.2C^4(G^3 P_0)^{1/2} \tag{1.4}$$

Mouschovias (1980) shows that for $T = 40K$, $M_c \approx 1.5 \times 10^2 M_\odot$ and concludes, therefore, that all observed molecular clouds ($\mu = 2.33$) should be collapsing.

In §1.2.3 it was suggested that a large proportion of molecular clouds may exist for $> 10^8$yrs without collapsing and undergoing SF. Clearly, for this to be the case, some additional force contributing to the support of the clouds against gravitational collapse must be operative.

1.3.2 The Importance of the Magnetic Field

The importance of the interstellar magnetic field in determining the behaviour of gaseous material in the Galaxy depends on the answers to the following questions

1. Is the magnetic field comparable with the other major forces in the Galaxy?

2. Does the field decay on timescales comparable with those of the system it is affecting?

3. Is the field sufficiently coupled to the majority of the matter to affect it?

By approximating the scalar energy densities of the magnetic, gravitational and radiative fields it can be shown that the three are, in fact, comparable. The interstellar magnetic field is therefore a significant reservoir of energy in the Galaxy

For a magnetic field of flux density **B** in a medium of finite conductivity σ and velocity field **v** we have

$$\partial \mathbf{B}/\partial t = \nabla \wedge (\mathbf{v} \wedge \mathbf{B}) + (\sigma \mu)^{-1} \nabla^2 \mathbf{B} \qquad (1.5)$$

When **v** = 0 this reduces to

$$\partial \mathbf{B}/\partial t = (\sigma \mu)^{-1} \nabla^2 \mathbf{B} \qquad (1.6)$$

This is a diffusion equation which indicates that the field leaks from point to point. Oppositely oriented field lines initially in different places leak together and neutralise one another causing the field to decay. This decay occurs on a timescale $t \approx L^2 \sigma \mu$ where L is a length scale. For astrophysical values of the conductivity, σ (∞) and length scale L, t is greater than the age of the universe and so field decay is unimportant.

For a medium with $\mathbf{v} \neq 0$ and $\sigma = \infty$ we have

$$\partial \mathbf{B}/\partial t = \nabla \wedge (\mathbf{v} \wedge \mathbf{B}) \qquad (1.7)$$

This equation specifies that the induction through a circuit, each element of which is moving at velocity **v**, is constant and thus represents the condition for 'flux-freezing', that is, there is no motion of the medium relative to the field lines. This condition occurs when the fractional ionisation is sufficiently high and requires that either the medium is stationary (magnetically dominated) or that the field is carried along with the motion (inertially dominated).

1.3.3   Cloud Collapse with a Magnetic Field

Consider again the isothermal cloud discussed in §1.3.1. It is now proposed that this cloud is threaded uniformly by a 'frozen-in' magnetic field. The flux cutting the cloud is $\phi = \pi R^2 B$ and is constant as long as the flux

freezing assumption holds. The virial theorem equation for cloud collapse now becomes (Spitzer 1978)

$$4\pi R^3 P_0 = 3MkT/\mu - R^{-1}[3GM^2/5 - R^4B^2/3] \qquad (1.8)$$

For the gravitational term to dominate at small R, as in the non-magnetic case, we require the expression in brackets to be positive. This occurs under the condition that $R^4B^2/3 < 3GM^2/5$ which holds when $M > M_c$ where M_c is a critical mass given by $M_c^2 = 5R^4B^2/9G$. Since $\phi = \pi R^2 B$ this becomes

$$M_c = (5/9)^{1/2}\phi G^{-1/2}\pi^{-1} \qquad (1.9)$$

For $M < M_c$, where M_c is seen to be proportional to $\phi/\sqrt{G}$, the cloud is gravitationally stable and cannot collapse. For such an above described isotropic collapse with flux freezing, the magnetic and gravitational forces increase proportionately. Thus, if the frozen-in magnetic flux is sufficient to support the cloud against collapse initially ($M < M_c$), no amount of subsequent contraction will cause the cloud to collapse. The isotropic collapse considered neglects the anisotropic cloud flattening effect of the magnetic field. Also, the virial theorem, being an integral relationship, does not take account of or give any information on the structure that may exist in the system.

Mouschovias (1976a and 1976b) obtains the time-dependent equilibrium states for a contracting isothermal cloud and then uses the virial theorem as an interpolation formula with the constants in the virial expression fixed by the equilibrium state solutions. He finds that $M_c = 0.126\phi/\sqrt{G}$—about $\frac{1}{2}$ of the critical mass predicted by Equation 1.9. Also, for $M < M_c$, he finds that the external pressure required for collapse is less than that predicted for a pure virial theorem analysis. It is thought that these discrepancies arise from the development of central density enhancements (*i.e.* condensations) in the clouds. This phenomenon is, of course, to be expected since we ultimately envisage SF occurring by the accretion of surrounding material onto such a protostellar object. Central density enhancements show up in time dependent analyses of even the simple collapse situation described in §1.3.1.

1.3.4   Collapse of a Rotating Cloud

The inclusion of molecular clouds in the general rotation of the Galaxy requires that they possess an intrinsic angular momentum. Estimates suggest that, in the diffuse pre-collapse stages, the cloud angular momentum will typically exceed expected stellar angular momenta by a factor of $\sim 10^6$ (Mouschovias 1980). In the case of binary systems, this factor is less and occupies a range of values depending on the 'width' (and hence angular momentum) of the binary system formed. The rotation of the cloud about some internal axis can, therefore, be expected to exert an important if not dominant influence on the dynamics of cloud collapse.

As mentioned in §1.3.3, for a sufficiently massive cloud, the presence of a magnetic field does not prevent cloud collapse since (in the isotropic case at least) the magnetic supporting force increases only in proportion with the gravitational force. Consider, however, a spherical cloud rotating about some internal axis. At the cloud's equator, the centrifugal force opposing gravity, F_c, is $\Omega^2 R$, where R is the cloud radius and Ω the angular velocity. If no external torques operate on the cloud then the cloud angular momentum, $M\Omega R^2$, is constant implying that Ω is proportional to R^{-2}. Hence, F_c is proportional to R^{-3} and, since the attractive gravitational force, F_G, varies only as R^{-2}, there will be an R at which F_c and F_G are in equilibrium and no further contraction can occur without the removal of angular momentum.

If the rotating cloud were to fragment into two cloudlets orbiting about a common centre of gravity, then each cloudlet would continue to contract until they again acquired a prohibitive angular momentum. In other words, the cloud angular momentum is transferred to the orbital angular momentum of the cloudlets. This process, however, would be expected to generate flattened distributions of stars which is contrary to observation.

A more promising mechanism for the removal of cloud angular momentum is magnetic braking—a process by which rotational energy is transferred from the cloud to its low density surroundings by the propagation of magnetic disturbances.

1.3.5 Magnetic Braking

A simple picture of magnetic braking is obtained by considering a rigidly rotating cloud with a frozen-in magnetic field. Unless the cloud mass is substantially greater than the critical mass, M_c, contraction will have proceeded preferentially parallel to the magnetic field lines leading to an oblate spheroidal geometry or, in the more extreme case, a relatively flat disc. Since the magnetic field in the cloud is expected to connect across the cloud boundary with the field in the surrounding uncondensed medium, rotation of the cloud will generate disturbances in the energy and stress of this field. These disturbances propagate outwards along the field lines into the surrounding low density material in the form of torsional Alfvèn waves which exert a mechanical effect. Due to the torsional nature of the propagated disturbance, the exerted mechanical effect takes the form of an enforced rotation facilitating the transfer of angular momentum from the cloud to the surrounding material. The torsional Alfvèn waves could, therefore, be viewed as outwardly propagating angular momentum waves, decreasing the rotational energy of the cloud. The cloud rotation is magnetically braked.

The efficacy of the magnetic braking depends upon the relative orientation of the axis of rotation and the cloud magnetic field. A simple estimate of the cloud braking time, t_b, may be obtained by calculating the time it would take for a wavefront propagating at the Alfvèn velocity to sweep out a volume such that the imparted rotation yields a moment of inertia for the volume equivalent to that possessed by the cloud itself. It has been shown that such simple treatments do give favourable results when compared with much more sophisticated models (Mestel and Paris 1984). These treatments predict that braking will be more efficient when the field is aligned perpendicular to the axis of rotation since, in this case, the Alfvèn waves propagate radially outward in the plane of the flattened cloud and encounter material with progressively greater moment of inertia. A simple geometry inferred for a rotating disc (highly flattened cloud) with the field aligned parallel to the axis of rotation is shown in Figure 1.2. The shaded surfaces represent the outwardly propagating wavefronts.
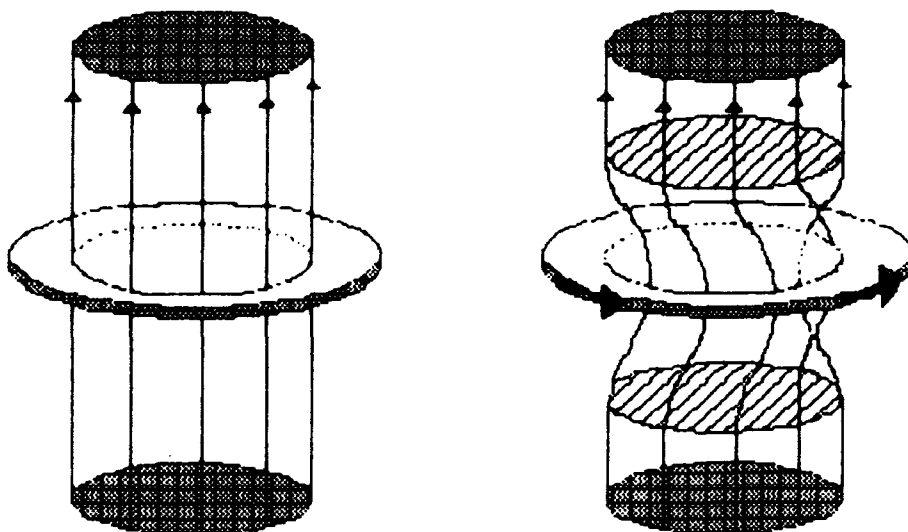
Figure 1.2: A magnetic braking geometry (adapted from Mouschovias 1980)

1.3.6 Flux Loss and Ambipolar Diffusion

In the above described models it has been assumed that the magnetic flux threading a cloud is constant during the cloud's contraction and that this flux is always capable of exerting a significant effect on the (neutral) mass. The effect is exerted by ion-neutral collisions—the ions being tied to the magnetic field. A spherical isotropic collapse requires that B vary as $n^{2/3}$ where n is the cloud density. Assuming the accepted values for n_0 and B_0 (the initial uncondensed values) and no loss of flux, collapse down to stellar densities (n_*) leads to values of $B_* \geq 10^8$G. However, Mouschovias (1976a and 1976b) has shown that for a more realistic anisotropic collapse with cloud flattening parallel to the field lines, B is proportional to n^k where $\frac{1}{3} \leq k \leq \frac{1}{2}$ which leads to a more moderate range of values for B_*. Nevertheless, there are two processes by which the effect of the magnetic field on the cloud dynamics may be diminished. These are the loss of magnetic flux from the cloud and the process of ambipolar diffusion by which neutral material can slip through the field. Both processes will affect the cloud critical mass (M_c) and the efficiency of magnetic braking, thus

having an important effect on the collapse of the cloud in general.

Flux loss can occur by self-negation of magnetic field lines. Two oppositely oriented magnetic field lines can be pushed together (by hydrostatic pressure, for example) and cancel out or a null point can develop where two field lines cross leading to field reconnection. The process of ambipolar diffusion or ion-slip can allow the ions to be driven through the neutral matter (which constitutes the majority of the mass in molecular clouds) by the magnetic pressure. Conversely, the neutrals could be driven through the ions by gravitational force. This process will lead to a gradual separation of the ions and neutrals and, since the field is locked to the ions, a separation of the neutrals from the magnetic field. It should be noted, however, that this process does not necessarily entail a loss of magnetic flux from the cloud.

Spitzer (1978) calculates an approximate steady state diffusion time, t_d, for the ions relative to the neutrals in an infinite cylinder of (mostly neutral) gas supported against self-gravitation by the magnetic pressure experienced by the ions. This gives $t_d = 5 \times 10^{13} n_i / n_H$ yrs, where n_i is the number density of ions. Therefore, for ambipolar diffusion to be important on the timescale of cloud collapse, $n_i / n_H \approx 10^{-7}$ which is possible in the interiors of molecular clouds.

1.3.7 Simple Scenarios

Simple virial theorem arguments show that there exists a critical mass M_c dependent on the magnetic flux ϕ and the geometry (usually defined by a 'shape' parameter) such that for $M > M_c$ gravitational collapse perpendicular to the field lines is possible and for $M < M_c$ such collapse is prevented by ϕ. Contraction parallel to the field lines is halted only by the establishment of hydrostatic equilibrium in this direction.

Although flux freezing cannot prevent the collapse of a sufficiently massive cloud, angular momentum can. It was seen in §1.3.4 that the ratio of centrifugal to gravitational forces varies as R^{-1}. Therefore at some stage during the contraction there will be a balance between these forces in two dimensions. Further contraction is contingent upon the effects of magnetic braking.

When $M < M_c$ any degree of braking will eventually slow down the cloud until it is rotating in approximate synchrony with its environment.

The cloud will thus flatten into a disc oriented perpendicular to the magnetic field lines. The disc is supported vertically by the hydrostatic gas pressure and radially by the magnetic field. Further evolution of the system depends on either the accretion of more mass (usually this involves a prohibitively large volume of space since accretion cannot be expected to take place perpendicular to the field) or the loss of magnetic flux. Both of these processes could eventually render the cloud mass super-citical enabling it to contract perpendicular to the field. If they occur on timescales longer than the braking timescale then approximate corotation (with the environment) will be maintained.

When $M \gg M_c$ the cloud will collapse almost isotropically. For more modest (supercritical) values of M some contraction perpendicular to the field will occur. If Ω is initially small the cloud may collapse down to quite a high density before Ω again becomes significant. This is especially true if the degree of magnetic braking is high, in which case the cloud will collapse in approximately magnetically diluted free fall. These scenarios may lead to large values for Ω and B at high densities, depending on if and at what stage ambipolar diffusion sets in.

For more moderate amounts of magnetic braking the cloud will approach approximate CGM (centrifugal, gravitational and magnetic) equilibrium, that is, the cloud will be more or less corotating with its environment and further contraction will proceed through a series of equilibrium states.

These scenarios may lead to the formation of a central protostellar object but their simplicity is restrictive and they cannot be expected to describe anything other than the idealised evolution of a single isolated condensation. A complete theory of SF must be able to explain the formation of binary and multiple star systems and, ultimately, planets. For more than one star to form in close association, the cloud must, at some stage in its evolution, undergo a process of fragmentation. At the densities associated with the initial collapse stages, the Jeans mass may typically be $\sim 10^2 M_\odot$. Thus, in order to produce stars of similar mass to the sun, solar mass fragments must occur and be sufficiently long lived to undergo individual collapse to protostellar densities. The existence of fragmentation is also evidenced by the observed clumpy nature of molecular clouds.

1.3.8 Fragmentation and Numerical Simulation

When a molecular cloud contracts isothermally, the Jeans mass, M_j, decreases with increasing density, n. This allows the formation of fragments which, assuming that they are gravitationally unstable, will contract separately. As the densities of these fragments rise they too may undergo fragmentation. This is the hierarchical fragmentation process suggested by Hoyle (1953). Eventually, the densities will be so high that further contraction must occur adiabatically. The onset of this opaque phase depends on the efficiency of various cooling processes such as molecular line transitions and (at higher densities) grain IR emission. Once the gas becomes adiabatic, M_j increases with density and fragmentation is suppressed (this is called opacity limited fragmentation). It may be argued, however, that by the time the temperature has risen sufficiently to render the fragment opaque, then it is dense enough to be considered a protostar.

The above argument neglects to include the important effects of the magnetic field, rotation and anisotropic contraction and cannot, therefore, be expected to adequately describe the contraction and fragmentation processes occurring in realistic molecular clouds. The inclusion of these factors complicates matters to such an extent that fundamental questions such as 'does fragmentation occur at all?' are difficult to address.

Numerical simulations can go some way in predicting what happens during cloud collapse but they too have their attendant difficulties and limitations. Numerical simulation of cloud collapse is usually achieved either by the solution of the hydrodynamic equations at various points in the cloud or by following the motions of fluid particles in N-body analyses. The results of simulations are affected by the assumed initial parameters, the degree of idealisation and to a large extent the model, depending for example on the way in which internal angular momentum transport is treated.

Highly idealised simulations by Larson (1978) suggest that the degree and manner of the fragmentation depends upon the ratio of the total cloud mass to the Jeans mass. When $M \approx M_j$ a single condensation forms with the remnant material gradually accreting onto the central object; when $M \approx 2M_j$ two condensations may form, usually one primary object and a smaller 'satellite' object; when $M \gg M_j$ several condensations may form.

Bodenheimer (1981) suggests that clouds are unstable to fragmentation over a wide range of initial conditions. In simulations of anisotropic cloud

collapse he finds that

1. Fragmentation does not occur as efficiently as might be expected from the hierarchical model of Hoyle (1953). There are various mechanisms by which density perturbations may be damped (*e.g.* pressure damping) before fragmentation can occur.

2. Fragmentation can proceed through the development of an intermediate ring stage. In this case the centre of the cloud represents a density minimum.

3. In the majority of cases two fragments form (binary fragmentation). This could account for the observed predominance of binary systems in the stellar population.

In simulations of rotating magnetic clouds, Dorfi (1982) illustrates the importance of the magnetic field in cloud collapse and fragmentation. Interaction of the gas with the frozen-in field can lead to the development of asymmetric density distributions which tend to be more prone to fragmentation than symmetric distributions. The relative orientation of the magnetic field and the axis of rotation is found to affect the efficiency of magnetic braking with the perpendicular case braking ten times more efficiently than the parallel case.

Chapter 2

Evidence for Energetic Outflow

It is now recognised that many, if not all pre-mainsequence (PMS) stars are, at some point in their evolution, involved in a phase of energetic interaction with the local parental cloud material. It seems that this energetic phase may occur in association with PMS stars of widely differing mass suggesting that it is a common factor in all SF processes.

Early indications that young stars may be involved in mass outflow were provided by spectral observations of the (almost certainly PMS) T Tauri and Herbig Ae/Be stars. The discovery of P Cygni line profiles in their spectra suggested the presence of strong outflowing stellar winds. Mass loss rates were estimated to be between 10^{-7} and $10^{-9} M_\odot \mathrm{yr}^{-1}$ in the case of the T Tauri stars and between 10^{-6} and $10^{-8} M_\odot \mathrm{yr}^{-1}$ for Herbig Ae/Be stars with wind velocities of $150 \rightarrow 450 \mathrm{km\ s}^{-1}$ (§2.1).

The luminous outburst of FU Orionis in 1936 has been identified with a more violent form of T Tauri phenomenon. Since that date, several more enigmatic FU Ori type stars have been observed (§2.2).

A most dramatic example of mass outflow, by virtue of sheer size and energy, is provided by the large scale 'high velocity' molecular outflows. Observations of the ^{12}CO and ^{13}CO rotational line transitions have helped to establish a range of important kinematical parameters for these objects. Empirical models and theoretical explanations for the outflows and their driving mechanisms have been advanced but general agreement is still sought. Observations of other molecular species such as CS, NH_3, H_2, HCN

etc. may help to clarify the situation. Molecular outflow will be discussed
at length in §2.3.

Bipolar and cometary optical nebulae have been observed in conjunction
with identified bipolar molecular outflows towards several PMS objects (*e.g.*
R Mon, PV Cephei and R CrA). In general, the optical and molecular
features are closely associated and show an approximate alignment of major
axes. The optical structures are usually more highly collimated than the
molecular flows although this is dependent to some extent on the resolution
of the CO observations.

Herbig-Haro (HH) objects have been associated with molecular outflows
and optical nebulosity in many objects (*e.g.* HH7-11, HH24, HH26, HH28).
This is particularly interesting in view of the interpretation of their emission
line spectra in terms of the post-shock recombination expected to occur
after the interaction of a hypersonic outflow or wind with the surrounding
cloud material. The measurement of HH object proper motion vectors
shows that many of them are rapidly receding from identifiable YSOs.
Their observation in conjunction with molecular flows thus strengthens the
interpretation of these regions as outflow (rather than gravitationally bound
motion). HH objects are discussed in §2.4.

Closely allied to the HH object observations is the detection of maser
emission from molecules such as H_2O and OH. These masing regions *also*
exhibit large recessional velocities (relative to their associated PMS object)
and provide an opportunity for the high resolution probing of regions very
close to the central star or protostar.

Perhaps the most exciting recent development is the discovery of colli-
mated high velocity emission line jets apparently emanating from several
YSOs. About 20 such jets are known to date and their close association
with HH objects is becoming increasingly apparent. Stellar jets have been
the subject of several very recent reviews (see, for example, Mundt *et al.*
1987, Mundt 1987) and so will not be dealt with in this chapter.

The postulation of disc structures around YSOs, perhaps responsible for
the collimation (and in some cases generation) of the above mentioned phe-
nomena, is a common theme in all current theoretical and empirical models
of SF. The detection of these structures is, therefore, of vital importance
and §2.5 reviews the evidence for circumstellar and interstellar discs.

2.1   T Tauri Stars

T Tauri stars are thought to be PMS objects of low mass (usually less than $3M_\odot$) and irregular variability. In the optical region, their spectra exhibit strong emission lines such as $H\alpha$, FeI, FeII, CaII, TiII, [SII], [OI], [NII] (Herbig 1985) which are often strong enough to mask the underlying stellar continuum and absorption spectrum. Variability of the emission line profiles of T Tauri stars is discussed by Mundt and Giampapa (1982) who suggest flare activity or variable accretion as an explanation. Non-thermal broadening of the emission and absorption lines is often seen suggesting stellar wind activity. Classical P Cygni profiles, indicative of mass outflow, are seen in about 5 per cent of the T Tauri population with a further 5 per cent exhibiting 'inverse' P Cygni profiles suggesting mass inflow (Kuhi 1978). Stars in the latter category are often termed YY Orionis stars (a list of them is given by Bertout and Yorke 1978).

It is difficult to estimate mass loss rates from line profile studies alone, since the distance from the star at which the emission is produced is not known. However, radio observations suggest that mass loss rates from these stars may be $\sim 10^{-7} M_\odot yr^{-1}$ (Lada 1985).

T Tauri stars are located above and to the right of the ZAMS on the HR diagram (Cohen and Kuhi 1976) which is the main reason for classifying them as PMS. Although their exact evolutionary status is unknown, it is thought that they may have passed through the main accretion and planetary formation phase and that they are now surrounded by remnant discs and dust shells—as evidenced by their excess IR emission. They are thus *bona-fide* stars in the process of contracting down onto the main sequence. Further evidence for their PMS evolutionary nature comes from their observed association with dark molecular clouds (star forming regions) and early type O or B stars (in NGC2264 for example) implying ages $\sim 10^6$yrs or so. The general properties of T Tauri stars are reviewed in detail by Strom *et al.* (1975) and, more recently, by Herbig (1985).

Higher mass stars ($M > 10M_\odot$) fall into the category of Herbig Ae and Be stars. These objects form a group of irregularly variable emission line stars spectrally very similar to T Tauri stars, showing P Cygni and 'inverse' P Cygni profiles.

2.2 FU Orionis Stars

The star FU Orionis was observed to increase in brightness by 6 magnitudes in 6 months during 1936/7 (Herbig 1977) and represents the prototype for this group of flare stars. The phenomenon appears to be long-lived (FU Ori still remains in its brightened state after 50yrs) and its rarity is testified to by the sparse population of the group. As well as the prototype, V1515 Cyg, V1057 Cyg, HH57 IRS and Elias 1-12 have been identified as FU Ori stars. Bastian and Mundt (1985) recorded line profiles for FU Ori, V1057 Cyg, V1515 Cyg and Elias 1-12 and concluded that all four show P Cygni type profiles indicative of strong stellar winds. These authors suggest that the winds are accelerated to high velocities ($\sim 200k$ ms^{-1}) very close to the stellar surface and note the spectral similarity between FU Ori and T Tauri objects, implying that the former may be a more pronounced version of the latter. The cause of the FU Ori outbursts is unknown but possibilities include an increase in the accretion rate onto the star, the removal of an obscuring dust screen or internal structural changes in the star itself.

Graham and Frogel (1985) discuss the recent brightening of HH57 IRS into a visible star and suggest that this object may have ejected a shell of gas and dust. The close association of this star with an HH object makes it even more interesting.

2.3 Molecular Outflow

Early observations of CO molecular line emission towards regions of suspected SF (Zuckerman *et al.* 1976, Kwan *et al.* 1976) identified the presence of high velocity molecular gas and revealed an unexpected facet of PMS stellar evolution. Surveys of these regions in the ^{12}CO and ^{13}CO rotational line transitions (see, for example, Cantó and Rodriguez 1982, Bally and Lada 1983, Edwards and Snell 1984) have provided a valuable picture of the large scale structure and morphology of these gas flow regions as well as an estimation of important physical parameters for the high velocity gas.

A high velocity flow may be distinguished from the bulk motion of the ambient cloud material by the width of the line profile. Molecular cloud line widths are typically only a few km s^{-1} wide whereas molecular flows exhibit red and blue shifted line wings extending for tens of km s^{-1}. Usually,

when the full width of the line is greater than 10km s^{-1} for an antenna temperature of 10^{-1}K a high velocity flow is deemed to exist. An extreme example is the Orion molecular flow with a line width of $\approx$ 180km s^{-1}. Bally and Lada (1983) found 37 sources satisfying the high velocity flow criterion, nineteen of which showed line widths in excess of 30km s^{-1}.

Spatial mapping of the molecular gas provides information on the morphology and distribution of the emitting regions. A study of the structure of the CO emitting lobes reveals that molecular outflows exhibit varying degrees of collimation. Many sources show a positional offset between the centroids of the red and blue shifted emission regions suggesting that the outflows are angularly anisotropic and in many cases 'bipolar'. This information is contained within the high velocity line wings as illustrated in Figure 2.1. Bipolarity places constraints on the kinematics of the flow but does not allow an unambiguous interpretation since simple processes such as rotation and anisotropic collapse as well as outflow could be responsible. However, as will be shown later, evidence strongly suggests that the observed high velocity motion represents the outflow of cold molecular material from the vicinity of a central PMS or protostellar object.

CO observations also facilitate the estimation of the mass and velocity of the gas and, hence, the linear momenta and kinetic energies of the outflows.

2.3.1 Determination of Outflow Mass

In order to determine the mass of gas in the outflow, the observed (CO) transition should, ideally, be optically thin in order to accurately obtain the column density of CO from its emission intensity. There is now considerable evidence to suggest that the ^{12}CO line is, in fact, optically thick towards most outflow regions and should therefore be supplemented by observations in ^{13}CO. However, it seems to be the case that observations in just ^{12}CO and multi-transition observations in both ^{12}CO and ^{13}CO give comparable results.

The column density of ^{13}CO per unit velocity interval is N_v^{13} and for the J=1 $\rightarrow$ 0 transition this is given by (Margulis and Lada 1985)

$$N_v^{13} = 2.5 \times 10^{14}(T_{ex} + 0.91)[1 - \exp(-h\nu/kT_{ex})]^{-1}t_v \qquad (2.1)$$

in units of cm^{-2}(km s^{-1})$^{-1}$. T_{ex} is the gas excitation temperature and t_v is the optical depth at velocity v. A conversion from CO to H$_2$ column
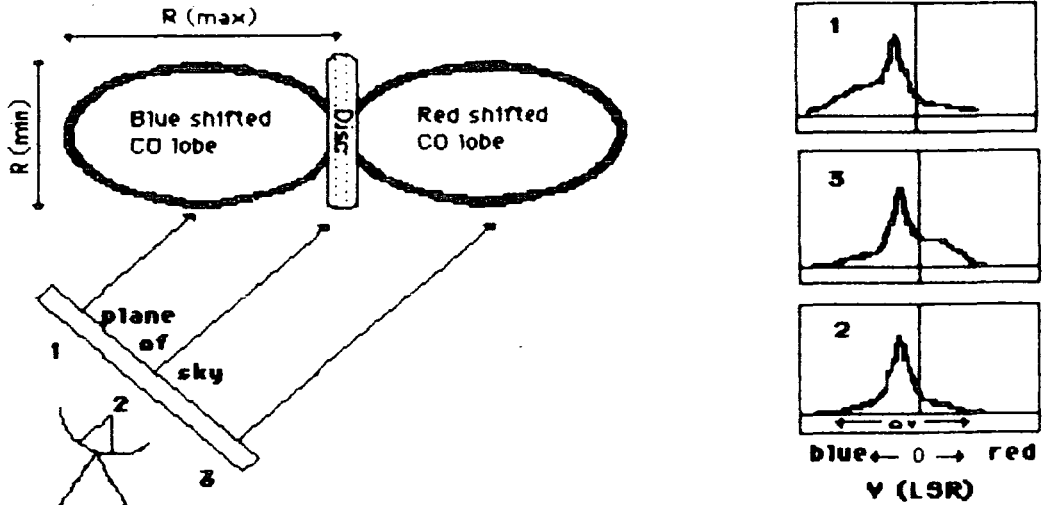
Figure 2.1: A schematic representation of the asymmetric line profiles of a bipolar nebula tilted out of the plane of the sky.

density must be made, the H_2 column density is then integrated over the spatial and velocity extent of the flow to give the mass. The mass of the outflow in $M_\odot$ is then given by (Lada 1985)

$$M = 1.67 \times 10^{-57} \, ^{13}X^{-1} \int \int N_v^{13} dv dA \qquad (2.2)$$

where ^{13}X is the abundance of ^{13}CO relative to H_2 and A is the projected area normal to the line of sight. Thus, in order to calculate the mass (M), T_{ex}, t_v, ^{13}X, A and v must be known. All of these quantities, except ^{13}X (which is usually assumed) can be obtained from CO measurements. For example, t_v can be obtained from observations of the intensities of the same transition in both ^{12}CO and ^{13}CO as long as the isotopic abundance ratio is known (and T_{ex} is assumed to be the same for both ^{12}CO and ^{13}CO) and T_{ex} can be derived from observations of two transitions in the same molecule, for example, the $^{13}CO(J=1 \rightarrow 0)$ and the $^{13}CO(J=2 \rightarrow 1)$ transitions. Usually T_{ex} is interpreted as the gas kinetic temperature. There is evidence to suggest that the outflow temperature may be systematically lower than the ambient cloud temperature indicating that these regions are remote

from the hot H_2 line emitting shock regions.

The variable t_v appears to be velocity dependent, decreasing with increasing velocity suggesting that the bulk of the material moves with low velocities. Indeed, towards the Orion (very high velocity) molecular flow, the $^{12}CO/^{13}CO$ ratio approaches the terrestrial isotopic ratio (Snell 1987).

The main sources of error in this sort of calculation come from:

- The estimation of the area A. Unless the source is mapped comprehensively in ^{12}CO the value of A used will probably be an underestimate.

- The inability to account for mass travelling at low velocities when performing the integration in Equation 2.2 due to the signal blending with the ambient cloud emission at these velocities.

- An underestimation due to the use of ^{13}CO in the mass determination equations. Material not detected in ^{13}CO but emitting in other lines will not be included.

- Also, the telescope beam-filling factor needs to be taken into consideration.

2.3.2 Ouflow Energetics

In order to calculate the kinetic energy and linear momentum of the outflow it is necessary to know the inclination of the major axis of the outflow to the line of sight. An upper estimate can be obtained by assuming v to be a constant and setting it equal to the maximum observed velocity (Bally and Lada 1983). Then the rate of change of kinetic energy $\partial T/\partial t$ (where T is $Mv^2/2$) is given by

$$\partial T/\partial t = Mv^2/2t_d = Mv^3/2R = L_m \qquad (2.3)$$

where t_d is the dynamical timescale and is approximated by R/v and the quantity $\partial T/\partial t$ is often called the mechanical luminosity L_m. L_m is obviously sensitive to the assumptions concerning the velocity, v.

A comparison between the mechanical luminosity of the outflow (L_m) and the bolometric luminosity of the associated PMS object (L_*) has been made in the case of 48 outflows by Snell (1987). This comparison shows

that, on average and notwithstanding the inherent assumptions, $L_m \sim 10^{-1}L_*$. This suggests that, in principle, there is enough energy in the radiation field of the central object to account for the energy present in the molecular outflow assuming a steady energy transfer over its dynamic timescale.

The force required to drive the molecular flow is F_m where

$$F_m = \partial P/\partial t = Mv/t_d = Mv^2/R \qquad (2.4)$$

where P is the linear momentum. The force that can be exerted through photon scattering in the radiation field is L_*/c. However, results for the above-mentioned 48 outflows suggest that $F_m \gg L_*/c$ by a factor of 10^2 or more for all the observed outflows. Therefore, in order to account for the observed momentum flux of the outflows, photons must scatter upwards of 10^2 times. As well as requiring considerable obscuration along the axis of the outflow, such frequent scattering would quickly reduce the photon energies to the IR. These results strongly imply, then, that the driving force responsible for the acceleration of the outflows is non-radiative in origin. However, it is interesting to note that L_m appears to be directly proportional to L_* suggesting that whatever is responsible for the outflows is also responsible for a large part of the bolometric luminosity of the central object. This is a potent argument for disc powered outflows which are expected to drive accretion onto the central protostar. A summary of the properties of molecular outflows is given in Table 2.1.

The enormous energies involved in these gas flows (up to 10^{48} ergs) points convincingly towards an explanation in terms of mass outflow, since gravitationally bound motion would require the common occurrence of very massive central objects. The angular anisotropy and large scale spatial extent of these phenomena also argues in favour of an outflow nature. In principle, low velocity molecular flows could be explained in terms of rotational kinematics, however, the association of HH objects and maser emission regions with measurably high radial velocities (§2.4.2) provides yet another reason for interpretation as outflow.

2.3.3 Angular Structure

The great majority of known molecular outflows exhibit bipolarity, with a red and a blue shifted lobe situated more or less symmetrically about a

Parameter	Typical Values
Size	$10^{-1} \to 4\mathrm{pc}$
Mass (outflow)	$1 \to 10^2 M_\odot$
Density (H_2)	$10^2 \to 10^3 \mathrm{cm}^{-3}$
Velocity	$10 \to 30\mathrm{km\ s}^{-1}$ ($127\mathrm{km\ s}^{-1}$ in Orion A)
t_d	$10^4 \mathrm{yrs}$
Energy	$10^{43} \to 10^{48}$ ergs
L_m	$10^{-5} \to 10^3 L_\odot$
L_*	$10 \to 10^5 L_\odot$
Kinetic Temp	20K

Table 2.1: Typical parameters of molecular outflows

central source. The presence of this angular anisotropy is indicated by the asymmetric (or pedestal) line profiles, as shown in Figure 2.1. In the list of molecular flows given by Lada (1985), 30 outflows are classified as bipolar, 7 monopolar and 4 isotropic. Monopolar outflows are flows in which only one lobe is detected (for example, NGC2264) whereas isotropic outflows are objects in which there is no detected separation between the red and blue shifted emission centroids. Lada (1985) classifies the S140 molecular flow as isotropic, however, Hayashi *et al.* (1987) have mapped this object in CO emission achieving 15 arcsec resolution and find it to be bipolar, emphasising the importance of telescope resolution in measurements of this sort.

Molecular outflows may be more usefully classified according to their degree of collimation, an approximate measure of which is given by the collimation factor R_{col} defined as the ratio of the major and minor axes of the flow (Figure 2.1). Lada (1985) tabulates R_{col} for 26 objects and finds values ranging from 1.0 to 6.2. It should be noted that (as mentioned above) the resolution of the CO observations has a major effect on the observed outflow dimensions. The results of surveys carried out with different instruments are, therefore, not expected to be directly inter-comparable. With this caution in mind, certain general conclusions can now be drawn.

It may be suggested that all molecular outflows are in fact bipolar and intrinsically well collimated. The observed spectrum of values for the parameter R_{col} then results from the geometrical factor due to the random

orientation of the outflow in space relative to the line of sight of the observer. On the basis of this assumption, certain predictions can be made if it is assumed that the bipolar outflow is a simple bicone. The probability of *observing* a value of $R_{col} = 1$ is just the probability of observing the bicone end on. This occurs when the line of sight from the outflow to the observer lies within the solid angle S subtended by the end face of the outflow of area A where $S = A/R_{max}^2$. However, $A = 2\pi(R_{min})^2$ and so $S = 2\pi(R_{min}/R_{max})^2 = 2\pi/(R_{col})^2$. For N outflows, then, the number of outflows, F, *observed* to have $R_{col} = 1$ is:-

$$F = NS/4\pi = N/2(R_{col})^2 \qquad (2.5)$$

Figure 2.2 shows the frequency distribution of the observed values of R_{col} for 26 molecular outflows considered by Lada (1985). The maximum collimation factor is 6.2. Assuming that all outflows are intrinsically well collimated and that $R_{col} < 6$ results from adverse geometry (*i.e.* substituting $R_{col} = 6$ into Equation 2.5), then Equation 2.5 predicts that the number of outflows observed end on should be less than one. Figure 2.2 shows that 10 of the 26 outflows have $R_{col} = 1$. It is probable, therefore, that the degree of intrinsic collimation varies between outflows and that, on the whole, bipolar molecular outflows are poorly collimated.

2.3.4 Spatial Structure

The spatial structure of the CO emitting gas and its various velocity components can provide important information on the structure and kinematics of the molecular outflow. If the outflowing gas is undergoing a steady acceleration, then we would expect to observe the highest velocity gas furthest from the source. Conversely, if the gas is decelerating then the low velocity material should appear more extensive.

In a study of the velocity structure of the CO emitting gas in the NGC2071, GL490, S140 and Orion outflows, Snell *et al.* (1984) suggest that there is a spatial coincidence between the low, intermediate and high velocity gas. Such a velocity structure is compatible with neither acceleration nor deceleration and Snell *et al.* suggest that the bulk of the gas resides in a thin expanding shell surrounding a wind filled cavity. Goldsmith *et al.* (1984) describe CO observations of B335, L1455M, L1455NW
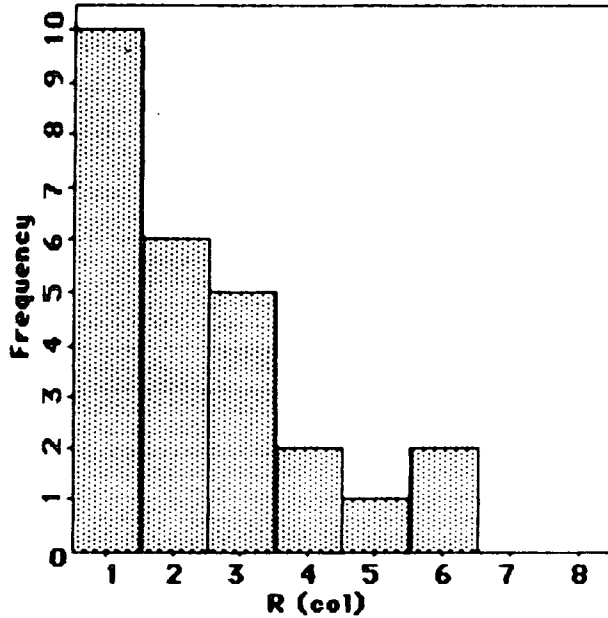
Figure 2.2: The frequency distribution of collimation factors for the 26 molecular outflows considered by Lada (1985).

and L723 and also conclude that the distribution of CO emitting gas is independent of velocity. They too advocate Snell *et al.*'s model of a swept up shell and explain the observed velocity dispersion in terms of a mass spectrum of clumps within the molecular shell. As the molecular clumps plough through the ambient cloud material they grow in size and subsequently decelerate. The great majority of well collimated bipolar molecular outflows are of insufficient spatial extent to obtain the resolution necessary for the unambiguous detection of shell structures. The L1551 outflow, however, is one of the more extended sources and is also well collimated (R_{col} = 5.2 Lada 1985). Recent high spatial resolution molecular line observations of this object have shown that velocity structure does exist in the spatial distribution of molecular gas.

2.3.4.1 Two Empirical Models

Snell and Schloerb (1985) present lunar occultation observations of L1551 and conclude that the low and high velocity CO emission does, in fact,

arise from different parts of the outflow. The high velocity gas is seen predominantly towards the centre of the outflow whereas the low velocity gas is seen towards the edges of the outflow and appears to encircle the high velocity gas. Snell and Schloerbs's results are derived from only one high resolution scan across the blue shifted lobe of L1551 and, hence, their spatial coverage is incomplete. With this limitation in mind they try to explain their observations in terms of the previously proposed expanding shell model. The centrally located high velocity gas corresponds to the front face of the blue shifted lobe/shell which, in addition to its motion away from the central source, is imagined as expanding towards us. The bulk of the emission and, hence, of the gas, resides in the shell-like structure seen at low velocities. This model is illustrated in Figure 2.3 which also shows the clumpy nature of the expanding molecular shell (inset box). The illustration (adapted from Lada 1985) is a simple one and does not show the position of the shock front which is expected to lie some way beyond the molecular shell. However, according to this model, it should be possible to detect the expansion of the far side of the molecular shell away from us in the velocity structure. Such a motion is not suggested by the observations of Snell and Schloerb (1985).

Uchida *et al.* (1987) have mapped the L1551 outflow in ^{12}CO J= 1 → 0 with the Nobeyama telescope, achieving good spatial coverage and angular resolution (15 arcsec). Their observations indicate a paucity of CO emitting material along the axis of the outflow which is again suggestive of a shell structure containing the bulk of the molecular gas. However, Uchida *et al.* suggest that the shell has a paraboloid geometry close to the source and a cylindrical geometry further out, so that when viewed in cross section it resembles a tuning fork. Uchida *et al.* observe a velocity structure similar to that seen by Snell and Schloerb (1985) with the high velocity material concentrated towards the centre of the outflow and the low velocity material distributed around it. They interpret this velocity structure as evidence for acceleration of the outflow material with distance from the central object (contrary to the conclusions of Snell and Schloerb).

In the expanding shell model, the shell is created by the ram pressure of the wind driving a shock front into the cloud and sweeping up the cloud material. In their model, Uchida *et al.* suggest that the molecular material is constrained to flow along a paraboloid/cylindrical surface in the manner predicted by their MHD outflow acceleration model (§2.3.7.1). The shell
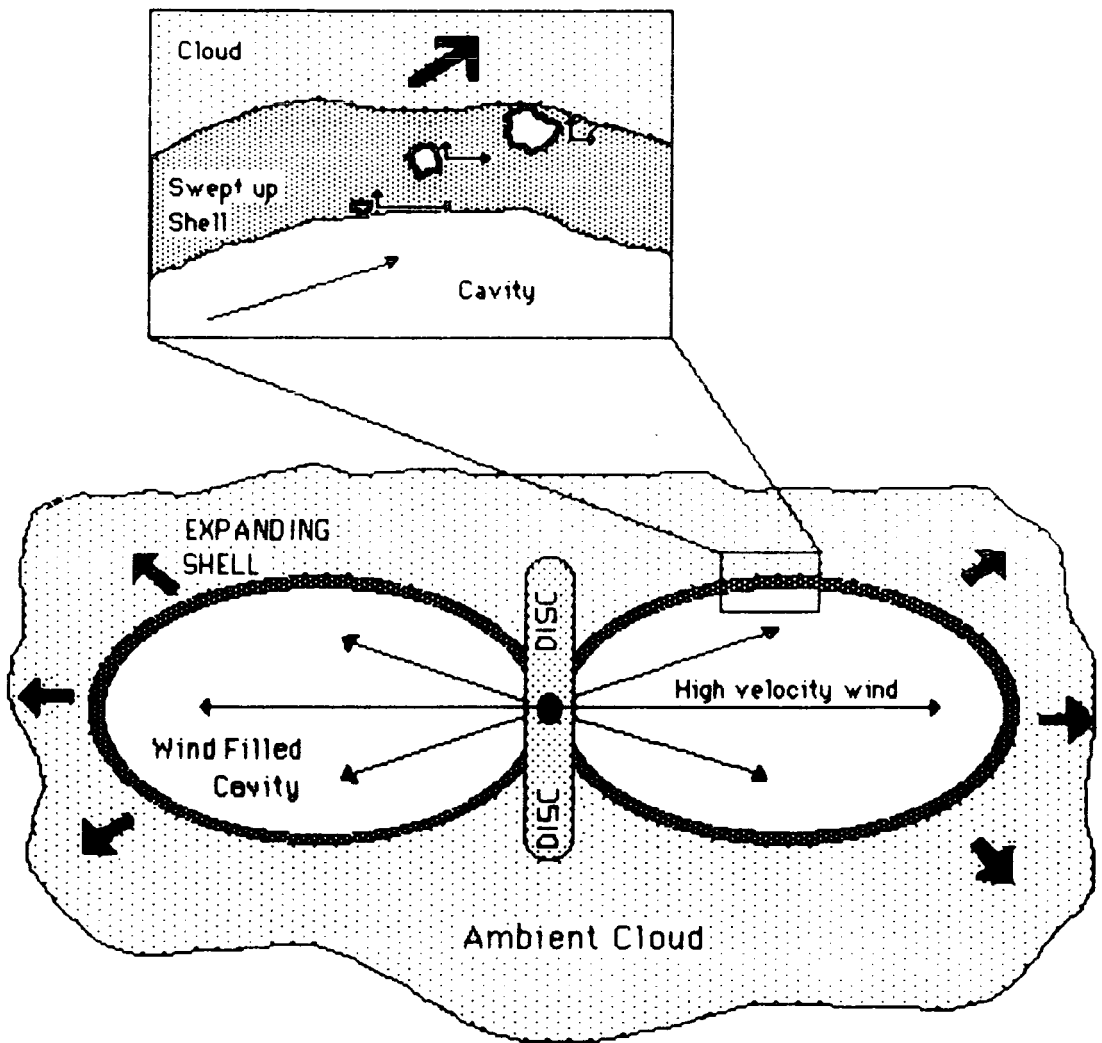
Figure 2.3: The expanding shell model as described in the text, (after Lada 1985).

is therefore composed of material originating in the molecular disc (which enjoys a ubiquitous status in outflow models—§2.5) which is accelerated progressively with distance from the source. An additional velocity feature, not seen in Snell and Schloerb's measurements, is the 'skew' distribution of low velocity material, with red shifted emission extending along the western edge of the blue shifted lobe and blue shifted emission extending along the eastern edge of the red shifted lobe. This skew distribution is interpreted in terms of a rotation of the outflow about its major axis, a phenomenon also predicted by the MHD acceleration models (§2.3.7). It is suggested that this rotation is in the same direction as that of the molecular disc (however, see also the interpretation of Moriarty-Schieven *et al.* 1987).

2.3.5 Frequency of Occurrence

Approximately 70 molecular outflows are known to exist at present and about 60 of these are within 1kpc of the sun. They are associated with PMS objects of low, intermediate and high mass and correspondingly diverse luminosities so how common a phenomenon are they? If it is assumed that the typical dynamic age of a molecular outflow is $\sim 10^4$yrs and that, during its PMS evolution, each star forms only one molecular outflow, then a comparison between the observed frequency of occurrence of molecular outflows and the estimated SF rate can be made. Such a comparison for objects within 1kpc of the sun suggests that all stars of mass $> 1M_\odot$ must go through the outflow phase (Snell 1987, Lada 1985). Since it is almost certain that all of the molecular outflows within 1kpc of the sun have not yet been discovered, 10^4yrs may be an underestimate of their dynamic age.

2.3.6 Other Observations

The H_2 molecule has a vibrationally excited emission line detectable in the IR at 2.12μm. Draine *et al.* (1983) suggest that shock waves propagating in dense molecular clouds are a copious source of H_2 emission. Such shock waves are expected to exist in the vicinity of YSOs and especially molecular outflows. Collisional excitation in the regions behind these shocks could also be a source of H_2 emission. Fischer *et al.* (1985) conduct a search for high velocity CO outflows in regions exhibiting H_2 emission and find a remarkable correlation between the two. They find that in one case (DR21)

the H_2 emission peaks at the periphery of the outflow region (as evidenced by the CO emission) and in several other cases it peaks within the outflow itself. Such a distribution would be expected for a population of randomly orientated outflows. Fischer *et al.* conclude that the ratio of energies in the H_2 and CO emissions is < 1 and that the H_2 emission can, therefore, in principle be driven by the molecular outflow. It is thought that the majority of the 2μm emission from the Orion OMC1 region could be due to H_2.

High velocity OH (hydroxyl) has been detected in absorption towards 9 out of a total of 23 known sources of molecular outflow (Mirabel 1987). The radio frequency OH emission lines arise in the ambient cloud whereas the velocity shifted absorption takes place in the high velocity molecular flow. The OH absorption traces the low density gas and thus provides information on outflow regions remote from the source. Mirabel concludes that, whilst the CO outflow geometry is reflected in the OH observations, the velocity of the OH emission is greater than that of CO in 50 per cent of the outflows. This result lends support to the acceleration with distance hypothesis proposed in connection with the CO observations of L1551 (Uchida *et al.* 1987) and endemic in the tuning fork model.

Far IR emission has been detected towards the L1551 outflow. Edwards *et al.* (1986) examine co-added IRAS data from an approximately 1 deg. square field centred on the L1551 cloud. They find that the 60μm and 100μm emissions are concentrated along the axis defined by the high velocity CO emission and correlate spatially with the region of molecular outflow. This alignment strongly associates the far IR emission with the outflow rather than with the L1551 cloud as a whole. Although the morphological correspondence is good, the 60μm emission appears to be extended beyond the outer CO contour. Edwards *et al.* also suggest that the energy for the far IR emission is derived from the high velocity wind rather than from direct radiative heating from the central source (an r^{-2} dependence is not detected). Clark and Laureijs (1986) report a correlation between the 60μm IRAS sky flux data and the high velocity CO emission in L1551.

Radio continnum measurements are an important method of probing the regions very close to the central star/protostar itself. Beiging *et al.* (1984) surveyed the Taurus-Auriga cloud complex at 6cm with the VLA and discovered compact elongated radio structures coincident with several previously identified YSOs (*e.g.* HH24 IRS, L1551 IRS5, DG Tau and Haro

6-10). Beiging *et al.* conclude that the probability of observing such radio emission is enhanced when an HH object is present and that usually the axis of elongation of the radio structure is colinear with the HH object.

2.3.7 Theoretical Models

The range of current theoretical models of bipolar molecular outflow in regions of SF may be divided into two categories *viz* stellar wind driven outflows and magnetically driven outflows. As seen in §2.3.2, the thrust requred to power the observed molecular flow exceeds that of the stellar radiation field by a factor of 10^2 or more, suggesting that the outflows cannot be radiatively driven. Therefore, in the absence of exotic stellar winds— rotationally driven winds for example—stellar wind theories of molecular outflow may find difficulty in accounting for the observed energetics. The evidence for proportionality between the mechanical luminosity of molecular outflows and the bolometric luminosity of the central source (§2.3.2) suggests that accretion discs may be a common factor in the production of both the outflow and central object luminosities, as predicted by the magnetically driven disc wind theories. These theories also predict a rotation of the outflowing material about the outflow axis (*i.e.* the material moves out from the central regions helically) which has been observed in the L1551 outflow (Uchida *et al.* 1987). It is not possible to account for such a rotation in terms of stellar wind driven molecular outflows.

In the light of the above considerations, stellar wind theories will be neglected here in favour of two promising magnetically driven disc wind theories. Also, anisotropic stellar winds and collimating mechanisms will be discussed in conjunction with HH objects (§2.4.3).

2.3.7.1 Magnetic Twist Acceleration

Uchida and Shibata (1987 and references therein) discuss a mechanism for the acceleration of material from the surface of an accretion disc by the action of a relaxing magnetic twist. In their model it is assumed that the disc is threaded by an, initially, purely polloidal magnetic field and that the disc rotation is keplerian. It is also supposed that this magnetic field is strongly coupled to the neutral material in the disc region (*i.e.* 'frozen

Energetic Outflow

in') and that it therefore rotates with the disc. The disc lies in the $z = 0$ plane of a cylindrical coordinate system and axisymmetry is assumed.

The rotation of the disc and its embedded magnetic field induces a B_ϕ twist component into the initially purely polloidal field configuration, leading to rotational wind-up of the field lines. The magnetic disturbance caused by this toroidal distortion of the field propagates along the polloidal field lines in the $\pm z$ directions as a series of torsional Alfvèn waves (Fig 1.3). These Alfvèn waves transfer rotational energy to the plasma through which they propagate and enforce corotation with the underlying disc out to quite large distances, thus facilitating the extraction of angular momentum from the disc. In such a magnetically braked environment, disc material can move in toward the central object and spin-up (*i.e.* v_ϕ increases as keplerian rotation is maintained) causing the field lines to become more and more twisted. When B_ϕ becomes sufficiently large, material in the surface layers of the disc may be accelerated along the z axis by the unbalanced $\nabla^2 B_\phi / 8\pi$ pressure force as the magnetic twist relaxes. Such an acceleration can result in the formation of a bipolar helical outflow of molecular disc material along the z (disc) axis.

Uchida and Shibata (1985) present axisymmetric numerical simp/ula- tions of molecular outflow based upon their magnetic twist acceleration model. They show that rotational wind-up of the disc field does occur and leads to the formation of a bipolar outflow with a cylindrical or 'tuning fork' structure. The outflowing material is concentrated into a thin shell and collimated along the z axis, the collimation being achieved by the mag- netic field which becomes increasingly polloidal with distance from the disc. A further consequence of this model is that the velocity of the outflow in- creases with distance from the disc until the terminal velocity is reached. It is expected that the terminal velocity will be approximately equal to the Alfvèn velocity and that the thickness of the shell will be dependant upon the range in r over which the disc is sub-keplerian.

The observation of 'tuning fork' type spatial structure and the evidence for acceleration with distance in the velocity structure of molecular line observations of L1551 (Uchida *et al.* 1987) provide support for hydromag- netically driven disc outflows.

2.3.7.2 Centrifugal Acceleration

The efficacy of angular momentum and mass transport by centrifugally driven hydromagnetic winds was first examined by Blandford and Payne (1982) in the context of accretion discs around black holes. These authors found that material may be accelerated from the surface of a Keplerian disc threaded by a frozen-in poloidal magnetic field provided that the field lines make an angle of at least 60 deg. with the plane of the disc. The resultant MHD outflow may achieve super-Alfvènic velocities and will pass through three critical points (points at which the outflow velocity equals the velocity of a backward propagating MHD disturbance) as it accelerates with distance away from the disc. Between the sonic and Alfvènic points, material is forced to corotate with the disc and its embedded field and is accelerated centrifugally along the poloidal field lines by the magnetic slingshot effect. In this region, the toroidal and poloidal velocities increase with radius. The process may be visualised as the acceleration of beads threaded along rotating wires (Königl 1986). Since the outflow takes place along the poloidal field it is intrinsically collimated along the disc axis. At and beyond the Alfvènic surface, a dominant toroidal field component develops due to distortion of the initially poloidal field by the increasing rotational inertia of the outflowing material. In this region, inertial forces dominate magnetic forces and corotation with the underlying disc and, therefore, centrifugal acceleration, is destroyed. However, the outflow may be further accelerated by the hydrostatic pressure of the toroidal field component and is expected to reach terminal velocity at the fast magnetosonic point (Michel 1969). Collimation of the outflow in this region may be effected by the development of hoop stresses in the field (Chan and Henricksen 1980).

In a series of papers, Pudritz and Norman (1983,1986a,b) and Pudritz (1985) further examine the centrifugal acceleration model with the specific aim of an application to bipolar outflows and the development of a 'self consistent' theory of SF. The disc is assumed to be threaded by a poloidal magnetic field which may be a condensed version of the original cloud field (although flux may not have been conserved during cloud collapse). The disc is expected to be in approximate CGM (centrifugal, gravitational and magnetic) equilibrium and the field in the disc is assumed to be radially

pinched as a result of marginal cloud contraction perpendicular to the field lines during the anisotropic collapse phase. This radial pinching provides the angle between the field lines and the plane of the disc necessary for centrifugal acceleration. As in the Uchida and Shibata model, axisymmetry is assumed. The main points of the Pudritz and Norman model are summarised below.

(i) An important constraint on the efficiency of the centrifugal drive in SF regions is the degree to which the magnetic field threading the disc is coupled to the mainly neutral disc material. This coupling efficiency may be expressed as the ratio (β) of the ion-neutral collision timescale and the dynamical timescale of the outflow (the ratio should be much less than 1 for effective coupling). If the field is able to slip through either the disc material or the material at the Alfvènic point, then little or no angular momentum transport can occur. Radiation from a central star would be expected to raise the fractional ionisation, especially in an envelope region near to the surface of the disc, causing this region to be strongly coupled to the field. However, material deeper inside the disc may not be strongly coupled to the field, due to the inability of ionising radiation to penetrate to these regions, so that a substantial portion of the disc angular momentum may not be available to power the centrifugal drive. Also, it may be necessary to explain the occurrence of molecular outflows during the protostellar era.

(ii) The mass flux in the outflow is equal to the mass flux through unit area integrated over the Alfvènic surface.

$$\dot{M}_w = \int \rho_n \mathbf{v_n} \cdot \mathbf{dA} \qquad (2.6)$$

where ρ_n is density, $\mathbf{v_n}$ the polloidal velocity of the neutrals and $d\mathbf{A}$ an elemental area.

(iii) Angular momentum is transported in the wind by the neutrals and by the magnetic field. The total specific angular momentum of the outflow (field and neutrals) is constant and depends only on the conditions at the Alfvènic point. It does not depend on B_ϕ or v_ϕ, since in order for v_ϕ to remain finite at r_a (the cylindrical Alfvèn radius), the field must arrange itself such that $L = \Omega r_a{}^2$ (Weber and Davis 1967). Thus, the specific angular momentum of the outflow is determined by the position of the Alfvènic point and the torque exerted by the outflow on the disc is given by:-

$$\dot{L} = \int L\rho_n \mathbf{v_n} \cdot \mathbf{dA} \approx f_g \dot{M}_w \Omega r_a{}^2 \qquad (2.7)$$

where f_g is a geometric factor depending upon the structure of the polloidal field and Ω is the disc angular velocity. This torque is responsible for driving accretion through the disc onto the central object such that the accretion rate $\dot{M}_a$ is given by:-

$$\dot{M}_a r^2 = f_g \dot{M}_w r_a^2 \qquad (2.8)$$

This relationship illustrates the principle of the lever-arm by which, as well as carrying off its own angular momentum, outflowing material may extract additional angular momentum from the disc by means of a magnetically mediated torque.

(iv) The terminal velocity of the outflow (that is, the velocity at the fast magnetosonic point) is given approximately (assuming rigid body rotation) by

$$v_\infty \approx v_{rot} \frac{r_a}{r_d} \qquad (2.9)$$

(where r_d is the disc radius) again illustrating the lever-arm principle. If the Alfvènic radius is ten times the radius of the disc, then a 50km s^{-1} outflow may be powered by a disc with rotational velocity 5km s^{-1}. As the disc angular velocity decreases, the lever-arm decreases in length and magnetic braking and outflow acceleration becomes less efficient.

(v) Pudritz (1985) describe a 'self consistent' model of SF in which accretion of disc material onto a protostellar core leads to the production of FUV photons. These photons create a disc envelope in which $\beta \ll 1$ holds and which is, therefore, strongly coupled to the field. This envelope material is efficiently accelerated away from the disc in the form of a bipolar outflow, extracting angular momentum from the disc in the process. The subsequent magnetic braking of the disc leads to enhanced accretion onto the core and the cycle is closed.

(vi) Pudritz and Norman (1986a) describe a two regime SMR/FMR (slow magnetic rotator/fast magnetic rotator) disc in which the majority of the rotational energy, mass and magnetic flux are concentrated in the outer (FMR) disc regions, whereas most of the thermal energy is concentrated in the inner SMR region. By means of such a two component disc, these

authors attempt to explain the range of collimation in observed outflows from the poorly collimated large scale ($\sim 10^{18}$cm) molecular outflows to the highly collimated ($\sim 10^{15-16}$cm) optical outflows and stellar jets. It is assumed that the optical outflows and jets are associated with the inner SMR region of the disc and are more or less thermally driven whereas the outer FMR region is responsible for the massive molecular outflows which are centrifugally driven. It is proposed that the inner optical outflows are pressure confined by the surrounding large scale molecular outflow, which is itself magneticallly collimated. Instabilities in the boundary region between the FMR and SMR portions of the disc have been used as an explanation for the FU Orionis phenomenon.

2.4   Herbig-Haro Objects

Although discovered in the early 1950s (Herbig 1951, Haro 1952) Herbig-Haro (HH) objects remained an enigmatic phenomenon up until the late 1970 s. Progress in the understanding of HH objects has been extensively reviewed over recent years (*e.g.* Mundt 1987, Schwartz 1985, Schwartz 1983a, Schwartz 1983b, Cantò 1983) and so only a brief resumè will be given here.

HH objects have been described variously as 'emission nebulae' and 'semi-stellar knots' and are usually identified on the basis of their optical emission line spectra. However, attempts to compress HH objects into one restrictive category will inevitably fail since the population of the group is in many respects diverse. Morphological diversity is evidenced by HH7-11 and HH102 for example, the former being a group of semi-stellar knots, the latter exhibiting an extended nebulous form. A description of HH objects as emission line nebulae can also be misleading since a significant reflective component is quite often seen (*e.g.* HH24, HH102, HH100, HH57).

It was originally thought that HH objects represent the pre-stellar clumps of material from which PMS objects such as T Tauri stars will eventually form. However, faillure to find spatial coincidence between HH objects and T Tauri stars soon cast doubt on this hypothesis. Current thinking requires that HH objects result from the interaction of the energetic outflows from YSOs with the clumpy cloud material in which these YSOs are embedded—a link that was first suggested by Osterbrock (1958).

Schwartz (1975) suggested that the optical emission line component of many HH object spectra is consistent with recombination behind shocks of moderate velocity (50 → 140km s^{-1}) and pre-shock density (50 → 300cm^{-3}). The structure of the shocks is currently a matter for debate and several models have been proposed.

Detection of linear polarisation at optical wavelengths in HH24 (Strom *et al.* 1974) implies a reflective origin for the illumination of this object. However, as mentioned above, the emission lines are characteristic of a low density origin and are expected to be intrinsic to the HH object. The observed linear polarisation most probably arises from the reflection of (mainly) broad band radiation from the associated YSO (SSV63 in the case of HH24) by dust in or surrounding the HH object. The polarisation of light from HH objects is discussed by Scarrott *et al.* 1987a, 1987b and 1987c corresponding respectively, to HH24, HH57 and HH100.

2.4.1 Emission Spectra

The optical emission line spectra of HH objects are characterised by lines such as [SII], [OI] (comparable in strength to Hα), [NI], [FeII] (comparable to Hβ) and weak [NII] and [OII] and possibly [OIII] (Dopita *et al.* 1987). Some HH objects possess a red continuum which may be the result of reflection.

Bohm *et al.* (1981) confirmed the existence of a UV excess in HH1 (previously observed by Ortolani and D'Odorico 1980) and noted that the excess is too large to be explained in terms of the shock used to model the emission in the optical wavelength range 3700 → 11000Å. Bohm *et al.* conclude that in the range 1200 → 3000Å, HH1 has a luminosity $L > 1L_\odot$ and that the emission increases monotonically with decreasing wavelength. Also, the high energy region of the UV spectrum (in HH1) appears to be dominated by high ionisation emission lines such as [CIV], [CIII], [SiIV] and [OIII]. These UV emission lines also appear to be over-luminous compared with the predictions of the shock model used to explain the optical emission (this may partly be due to the use of an inappropriate extinction curve). The UV continuum excess was explained in terms of the H$_2$ two-photon (2p) process by Dopita *et al.* (1982) and Schwartz 1981. Schwartz (1981) attempted to reconcile the UV excess problem by means of a two component shock model in which a low velocity shock gives rise to the optical emission

and a high velocity shock gives rise to the UV emission. It was suggested that such a two component model may occur in the interaction of a stellar wind with a dense clump—a head on shock would result in a high excitation region whereas a more oblique shock would lead to a (more extensive) low excitation region (see §2.4.3.1). However, it has been suggested by Mundt and Witt (1983) that a significant proportion of the UV emission from HH1 and HH2 results from the reflection by dust grains of light originating in the Orion reflection nebula.

In a 2μm survey, Elias (1980) detects H_2 emission towards several HH objects. He concludes that the emission arises in fairly dense gas ($\approx 10^4 cm^{-3}$) excited by low velocity shocks (15km s^{-1}). Such conditions are not concomitant with those invoked to explain the optical emission which tends to reinforce the idea of a clumpy medium with regions of high and low excitation. A list of HH objects detected in H_2 is given by Mundt (1987).

2.4.2 Velocities of HH objects

Many HH objects exhibit considerable proper motions and, hence, tangential (to the line of sight) velocities. The measurement of the proper motions of 66 HH knots has been accomplished by Schwartz *et al.* (1984) and references therein. The maximum observed tangential velocity to date is 350km s^{-1} in the case of HH1. However, proper motion estimates do, of course, depend on the assumed distance to the HH object and often this is under some dispute. Mundt (1987) also suggests that 65 per cent of the tangential velocities estimated to be under 100km s^{-1} may be in error by more than 50 per cent.

The backward projection of the HH object proper motion vector often intersects an identifiable PMS star or previously known IR source, thus providing direct evidence of a physical association between the two. Indeed, such an extrapolation of proper motion vectors has been used as a means of limiting the survey area in the search for embedded IR sources associated with visble HH objects and has met with considerable success (Cohen *et al.* 1985 and references therein). In some cases, two or more HH objects are seen to be receding in different (often diametrically opposite) directions from a common IR source or PMS star providing strong evidence for collimated (bipolar) outflow or ejection from these central objects.

Examples of this phenomenon are HH1 and 2 receeding from the opti-
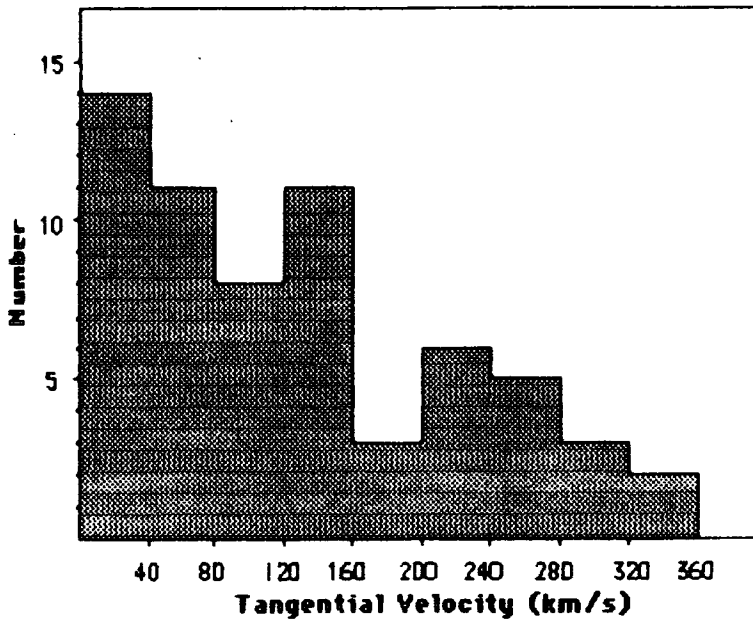
Figure 2.4: The frequency distribution of the observed tangential velocities for 63 HH knots (from Schwartz 1986).

cally obscured VLA source, HH46 and 47 with oppositely directed colinear proper motions in the Gum nebula and HH32 A,B,C and D receeding from AS353A. The frequency distribution of tangential velocities—as derived from the observed proper motions—is shown in Figure 2.4 for 63 HH knots. These knots represent individual condensations and not necessarily independent HH objects. The data is taken from a compilation by Schwartz (1986). Although high tangential velocity HH objects clearly exist, 50 per cent of the population shown in Figure 2.4 have velocities $< 120 \mathrm{km\ s^{-1}}$.

High resolution spectroscopy can provide detailled information on the radial motion of gas associated with the HH object. Emission line widths and velocity extents of up to $420 \mathrm{km\ s^{-1}}$ have been observed in HH32 by Hartigan *et al.* (1984). Such large emission line widths are most easily interpreted in terms of emission line shocks. However, the relationship between the high velocity gas motion and the velocity of propagation of the emitting region (the HH object) through space depends on the geometry adopted for these shocks (*i.e.*the model) and their orientation relative to the line of sight. Figure 2.5 shows the frequency distribution of radial velocities
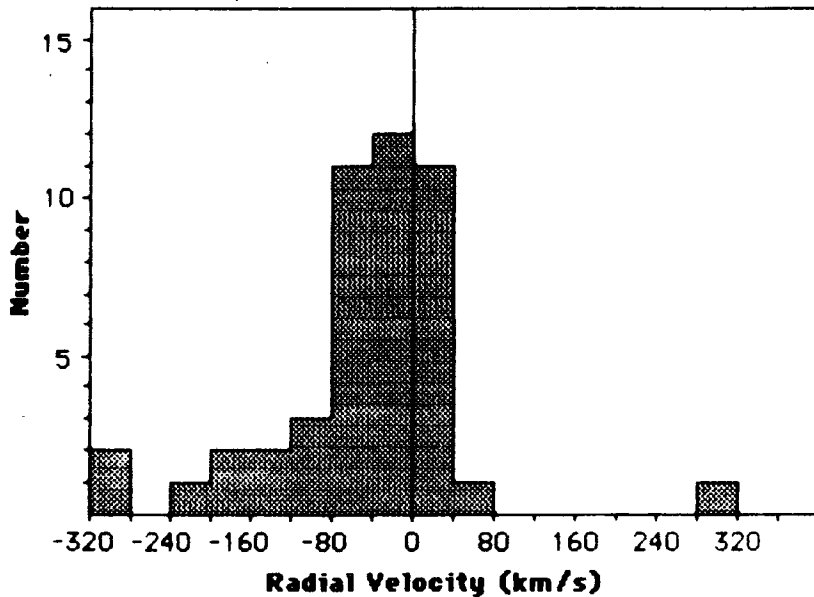
Figure 2.5: The frequency distribution of the observed radial velocities of 46 HH knots from Schwartz (1986) and Cantò (1981).

for 46 HH knots taken from Schwartz (1986) and Cantò (1981).

The sample possesses a very noticable blue shifted asymmetry with more than 70 per cent of HH knots exhibiting a negative radial velocity. This asymmetry is most easily interpreted as an observational selection effect. Since SF regions are preferentially observed towards the extremities of molecular clouds, red shifted HH objects will be systematically more heavily obscured and thus harder to find than blue shifted ones.

The association of some HH objects with bipolar molecular outflows is suggested by their observed spatial coincidence and enforces the opinion that these phenomena are manifestations of a common SF event. In such cases the HH objects are commonly associated with the blue shifted lobes of the outflow as would be expected from the distribution shown in Figure 2.5. They exhibit proper motions typical of participation in a large scale outflow from the central object. HH28 and HH29 in the L1551 bipolar outflow and HH7-11 associated with the bipolar outflow in NGC1333 are examples of such a coexistence and the additional support provided by HH objects for the interpretation of the large scale molecular gas motion as gravitationally

unbound outflow.

2.4.3 Theoretical Models of HH Objects

Any theoretical model of HH objects must be able to satisfactorily explain

1. The charateristic emission line spectrum and its intensity

2. The large proper motions and/or radial velocities shown by many HH objects

3. The spatial alignments and associations between HH objects and nearby YSOs.

Support for the idea that the HH emission spectra are typical of a combination of low and high velocity shocks was presented in §2.4.1 and current theoretical treatments, as well as reflecting observation, illustrate the range of conditions and geometries under which these shocks may arise. Four models for the generation of HH objects will be considered, all have points for and against them. If we consider it unlikely that a single global formation mechanism is active in the Galaxy then the observed population may be satisfactorily explained in terms of these four models.

2.4.3.1 Shocked Cloudlet Models

Schwartz (1975), Schwartz (1978) and Schwartz and Dopita (1980) examine the interaction of a centrally generated isotropic stellar wind with dense clumps or cloudlets in the surrounding cloud medium. The obstruction of a supersonic stellar wind by a dense cloudlet is expected to result in the formation of a luminous bow shock and the acceleration of the cloudlet away from the wind source. Schwartz (1978) presents emission line width and radial velocity data for the complex of knots in HH1 and 2 and proposes an interpretation in terms of such a wind-cloud interaction with the geometry illustrated in Figure 2.6.

In this model the shocked material is the stellar wind. The component of the stellar wind normal to the main shock (2) must move subsonically behind the shock resulting in the formation of a high excitation region (3).
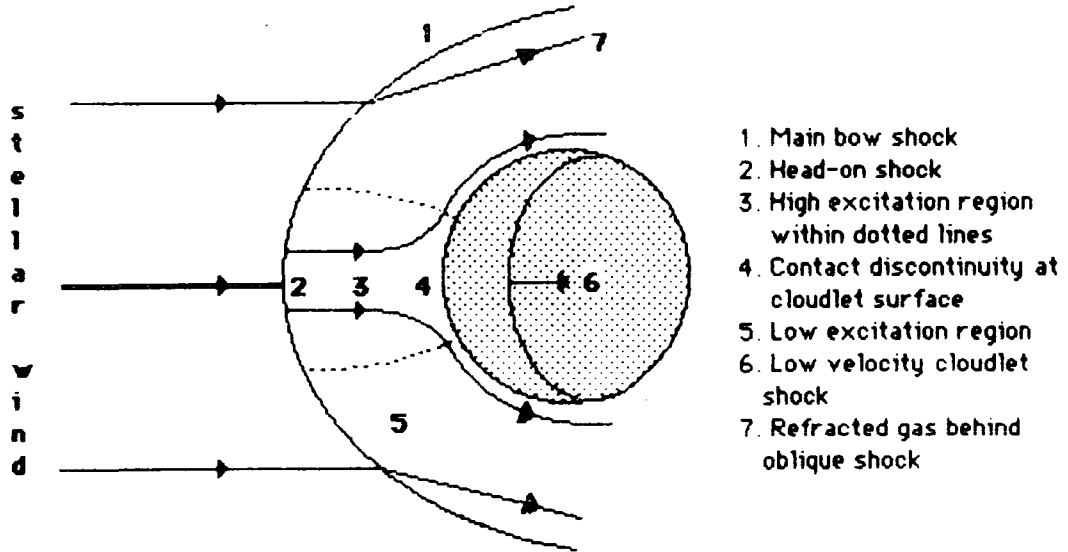
Figure 2.6: The shocked cloudlet model (after Schwartz 1985).

It is this high excitation 'head' region that may be expected to produce the UV emission observed in some HH object spectra, provided that the pre-shock wind velocity is sufficient. The component of the wind impacting obliquely with the main shock (7) will be refracted and will retain a significant proportion of its pre-shock velocity (*i.e.* it will remain supersonic). Oblique shocking and supersonic flow behind the shocks are predicted by the observed emission line widths. These regions in the 'wings' of the bow shock are expected to be responsible for the low excitation optical part of the emission spectrum. Since they are more extended than the high excitation 'head' region, they account for most of the observed luminosity of the HH objects. The dotted lines represent the boundary between the subsonic and supersonic flow regions. The pressure at the front face of the cloudlet may drive a low velocity shock through the cloudlet itself (6). Schwartz (1978) suggests that the IR H_2 emission observed towards many HH objects is characteristic of such a low velocity (15km s^{-1}) shock.

Ròzyczka and Tenorio-Tagle (1985) model the bow shocks around dense clumps in a supersonic wind and find that (i) the shocks can extend over a region covering 15 times the cloudlet diameter and (ii) the shape of the

shock is strongly dependent upon the wind velocity. It seems likely, there-
fore, that for low velocity winds only the gas at the head of the bow shock
is sufficiently excited to radiate (optically) whereas for high velocity stellar
winds optical emission may be seen over an extended region (*i.e.* in the
wings of the bow shock). This suggests that HH objects with optically vis-
ible bow shocks (*e.g.* HH34, HH1 and 2) are associated with high velocity
stellar winds.

2.4.3.2 Interstellar Bullets

The interstellar bullet model was first proposed as a possible explanation
for maser emission and HH emission in regions of SF by Norman and Silk
(1979) and also by Rodriguez *et al.* (1980). In this model masers are
presumed to be the precursors of HH objects.

It is envisaged that an expanding shell of swept up cloud material—
propelled outwards by a centrally generated stellar wind—becomes prone
to the development of Rayleigh-Taylor instabilities. As a result of these
instabilities, dense clumps of material may form which are also swept
up by the ram pressure of the stellar wind. These clumps are typically
denser ($\sim 10^{11} \text{cm}^{-3}$) than those supposed in the shocked cloudlet model of
Schwartz since they are intended to be a source of the observed H_2O maser
emission. As the clumps are accelerated outwards (at $100 \to 200 \text{km s}^{-1}$)
they plough into the cloud material surrounding the region of SF leading to
the development of a preceeding bow shock. The clumps also expand with
distance from the central object so that after 10^3yrs they may be 10^{-1}pc
from the star and of radius 10^3AU with a density of $\sim 10^5 \text{cm}^{-3}$ (Norman
and Silk 1979). At these densities all maser activity will have ceased and
radiation from the preceeding bow shock will have taken over. The physics
of the bow shock is expected to be the same in this model as in the shocked
cloudlet model with the exception that in this case the shocked agent is the
cloud material.

Both the shocked cloudlet and the interstellar bullet models make pre-
dictions about the expected variation of the HH object excitation with its
velocity away from the exciting source. The former model predicts that
high velocity HH objects should be less energetic than low velocity ones
whereas the latter model predicts the reverse. However, discrimination be-

tween the two models on this basis is not simple since there is evidence for both cases. Schwartz (1986) shows that HH object excitation (as measured by the excitation parameter [OII]/[OI]) increases with velocity in the case of the HH1 knots suggesting the interstellar bullet model. However, the same excitation parameter appears to decrease with velocity in HH43 (wherein the highest excitation component also appears closest to the exciting star) suggesting the shocked cloudlet model.

Tenorio-Tagle and Ròzyczka (1984) suggest an alternative origin for the interstellar bullets. They propose that secondary clumps may form in the cooling material swept up by conical shocks which they envisage occurring as the main shock wraps around the primary clump and converges on the far side.

A critique of both the shocked cloudlet model and the interstellar bullet model lies with their difficulty in accounting for the observed luminosities of HH objects since the stellar wind is assumed to be isotropic and the HH objects subtend a very small solid angle at their central star. This problem has lead many authors to consider mechanisms for the focussing and collimation of stellar winds.

2.4.3.3 Focussed Wind Models

Several models of HH objects involving a focussed or collimated stellar wind or outflow as the energising agent have been proposed. Two such models will briefly be considered here.

(1) Cantò's focussed stellar wind model

Following Cantò (1980), Cantò and Rodriguez (1980) envisage a YSO embedded within a cloud possessing a density gradient. The interaction of the stellar wind from a YSO with an isotropic density distribution would normally result in the formation of a spherically expanding shell of swept up cloud material surrounding a spherical stellar wind bubble. However, in the presence of a density gradient in the ambient medium the stellar wind bubble will expand preferentially in the direction of least density resulting
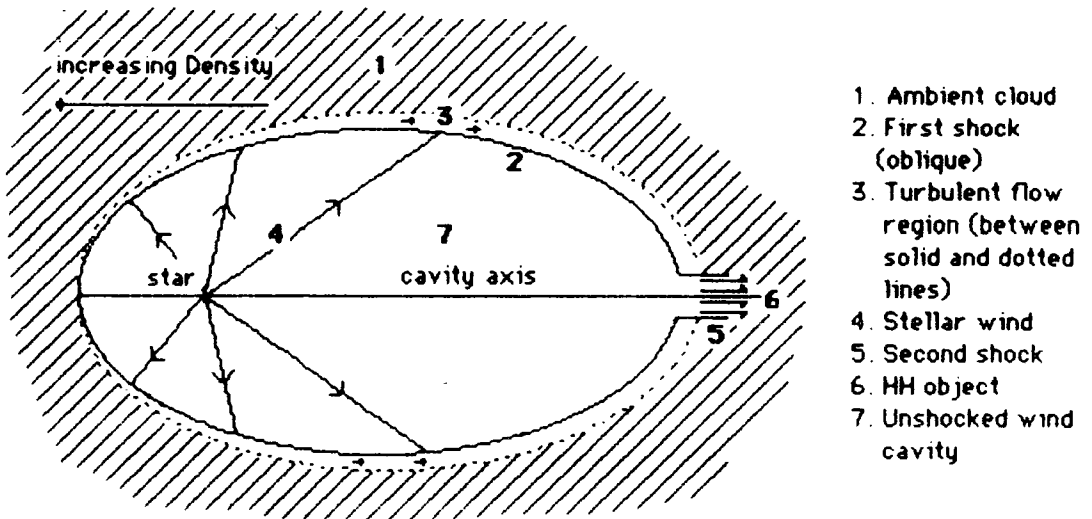
Figure 2.7: Cantò's focussed stellar wind model.

in the formation of an ovoid (rather than spherical) cavity. This geometry is illustrated in Figure 2.7.

At the boundary of the ovoid cavity, rather than being stopped by a head-on shock (as in the case of a spherical cavity), the stellar wind is shocked obliquely and refracted towards the apex of the cavity furthest from the star. In this apical region, the stellar wind converges and shocks again, this time against itself. It is proposed that the HH object is formed from the cooling material behind this second shock. A critique of this model lies in its difficulty in accounting for the observed high velocities of some HH objects (§2.4.2) since the shock cooling region is expected to remain more or less fixed in space.

(2) Königl's focussed stellar wind model

Königl (1982) attempts an interpretation of all bipolar outflow phenomena within the context of a single collimated stellar wind model. The model is

similar to that proposed by Cantò in that it describes the interaction of an initially isotropic stellar wind with the density gradient in the surrounding cloud. Königl shows that as the stellar wind bubble expands then, under certain conditions, it may become unstable to the formation of de Laval nozzles. The outflow is then channelled, through the de Laval nozzles, into two (assuming that the star has formed at the centre of the density distribution) oppositely directed supersonic jets.

The interaction of the supersonic jet flow with the ambient cloud material may result in the acceleration and excitation of clumps, as described in the shocked cloudlet and interstellar bullet models, and the formation of HH objects. Such a synthesis of models is particularly attractive in view of the spectroscopic support for bow shocks in HH objects and in view of the less stringent stellar wind energy requirements afforded by the collimated outflow models.

Sudden changes in the pressure of the medium through which the jet propagates may induce oscillatory behaviour in the jet boundary resulting in internal cross shocks and perhaps Mach discs. Such periodic expansions and rarefactions of the jet material and the attendant oblique shocks may afford an explanation for the recent observation (*e.g.* Mundt 1986) that HH objects sometimes represent the brightest knots in faint (and therefore previously unobserved) optical emission line jets.

A further point in favour of the focussed wind models is the morphological similarity between many optical bipolar and cometary nebulae and the theoretically predicted wind cavity geometries. A natural explanation for bipolar nebulae could be the reflection of light from the central object by the walls of the swept out stellar wind cavity. A particularly striking illustration of this conjecture is the HH57 nebulosity in which HH57 and a recently identified FU Orionis star appear to be connected by two nebulous 'arms' reminiscent of the walls of an ovoid cavity (Scarrott *et al.* 1987b).

2.5 Evidence for Discs around YSOs

As was discussed in §1.6.3, the evolution of a rotating cloud in the presence of a magnetic field leads naturally to anisotropic collapse and the formation of a central disc structure. Such disc structures (of both interstellar and circumstellar proportions) are a ubiquitous factor in all current theoretical

models of bipolar outflow. Also, although planetary formation is poorly understood, it is thought that the solar system must have evolved from some sort of disc structure, perhaps similar to the highly flattened structure found recently around the star β Pictoris (Smith and Terrile 1985). At present, therefore, the existence of discs around YSOs is a theoretical necessity. The observational verification of these structures can be divided into direct and indirect evidence.

2.5.1 Indirect Evidence

Polarisation measurements of both optical and IR sources identified as the central exciting stars in regions of energetic outflow have shown that many such objects exhibit considerable linear polarisation. This polarisation has been interpreted as evidence for the existence of dusty discs surrounding and obscuring the central YSOs.

In the optical regime, linear polarisations of 10 per cent (much greater than typical interstellar polarisations) have been observed towards many suspected YSOs (see for example Scarrott *et al.* 1986 and references therein). This topic will be discussed in detail in Chapter 7.

In the IR (2.3μm), Sato *et al.* (1985) present aperture polarisation measurements for nine sources associated with high velocity molecular outflow and observe levels of polarisation in the range 4 → 20 per cent. These authors note that the PA of polarisation tends to be perpendicular to the bipolar outflow axis. Hodapp (1984) also observes significant polarisation towards nine IR sources associated with collimated mass outflow and concludes, similarly, that the angle of polarisation lies preferentially perpendicular to the outflow axis.

Both Sato *et al.* (1985) and Hodapp (1984) suggest that the scattering of starlight from dust grains in non-spherical circumstellar shells (*i.e.* discs) is responsible for the observed IR polarisations. However, Scarrott *et al.* (1987d), in a study of optical polarisations find compelling evidence for magnetically induced polarisation in a number of objects associated with bipolar outflows. The relative merits of these polarising mechanisms will be discussed in Chapter 7.

The observation of cometary and bipolar nebulae illuminated by sources totally obscured in the visible provides more indirect evidence for the existence of dusty discs around these sources (although bar-like obscuring

geometries would equally suffice in some cases).

2.5.2 Direct Evidence

Molecular line observations have provided a considerable amount of direct evidence for the existence of non-spherical gas condensations in association with YSOs. Although the angular resolution of the mm observations is generally not good, it is often sufficient to determine the shape of the gas condensation and its location relative to nearby YSOs on size scales typically $\sim 10^{-1}$pc (*i.e.* 'interstellar' dimensions). Such condensations have been detected in ^{12}CO, ^{13}CO, NH$_3$ and CS (each molecule emits within a characteristic density range—increasing density in the order given) and many appear to be disc-like.

Cantò *et al.* (1981) observe a disc structure around R Mon in CO emission which they propose is the collimating structure for the bipolar outflow, also observed in CO. The major axis of the CO disc structure is perpendicular to the CO outflow axis, as required by current theories of molecular outflow collimation and ejection.

The Nobeyama 45m dish has been used to observe several disc-outflow systems with the following conclusions (Kaifu 1987):

1. Discs have a double peaked structure expected of a toroid viewed edge on—a toroid being a disc with a central hole.

2. The polar cavities of the molecular toroids appear to 'fit' the apical regions of the molecular outflow, that is, the outflow appears to take place from the surface of the toroid. This conjecture is supported both by the spatial and velocity distributions of the emitting gas.

Kaifu *et al.* (1984) observe such a toroid in the CS J= 1 $\rightarrow$ 0 transition towards the L1551 molecular outflow. The CS toroid appears perfectly positioned between the red and blue shifted CO lobes and lies in a plane perpendicular to the major axis of the CO outflow. The proposed exciting source of the outflow, L1551 IRS5, lies between the two peaks of the CS toroid. Kaifu *et al.* (1984) find evidence for rotation of the CS toroid, although this has not been independently confirmed (Moriarty-Schieven *et al.* (1987) find no evidence for rotation in their CS measurements). The

proposed rotation is in the same sense as that detected by Uchida *et al.* (1987) in the blue shifted CO lobe.

Torrelles *et al.* (1983,1985,1986) present surveys of the inversion transition of NH$_3$, made with a 37m single dish, in regions of high velocity molecular outflow. Torrelles *et al.* (1983) find that 7 out of 10 observed bipolar outflows show NH$_3$ emission. The NH$_3$ distributions suggest elongated condensations of size $\sim 10^{-1}$pc ($\equiv 10^4$AU) surrounding the outflow sources and orientated with their major axes in a plane perpendicular to the outflow axes. They detect NH$_3$ emission associated with the L1551 outflow but find that the distribution appears to be orientated along the axis of the outflow (rather than perpendicular to it) which is not suggestive of a collimating torus. Torrelles *et al.* (1985) present VLA observations of the NH$_3$ transition in L1551 which show an emission region positionally offset from L1551 IRS5. They also note the orthogonality of the structures detected in their 1983 single dish survey and the single dish survey of Kaifu *et al.* (1984). Torrelles *et al.* (1986) observe nine molecular outflow regions and observe NH$_3$ emission towards three of these. However, in this survey, most of the NH$_3$ structures are unresolved within their 1.4 arcmin beam.

The efficacy of molecular line observations in the search for toroids around YSOs is demonstrated by the number of detected candidate structures (Kaifu 1987 lists 11 bipolar outflows in which toroids have been detected in a plane perpendicular to the outflow axis). It is probable that the CS structure observed by Kaifu *et al.* (1984) in L1551 represents the expected molecular toroid around L1551 IRS5 and that the NH$_3$ structures of Torrelles *et al.* (1983) can be interpreted as swept up gas—*i.e.* part of the molecular outflow. Nevertheless, the need for caution is evident and ideally more than one molecular species should be surveyed. Also of relevance are the mm interferometric measurements of Sargent *et al.* (1987).

IR observations have been successful in detecting extended asymmetrical dust distributions around several YSOs.

Cohen *et al.* (1985) present IR photometry of sources associated with HH objects and find evidence for extended emission from several of these sources. For objects in which the emission is resolvable, the axial ratios imply a toroidal dust distribution orientated perpendicular to the associated outflow (*i.e.* the emission is resolvable perpendicular to the outflow but not parallel to it). In the case of SVS 13 (the IR source associated with HH7-11) Cohen *et al.* (1985) estimate a radius of 400AU for the dust

toroid.

The near IR speckle interferometric observations of Beckwith *et al.* (1984) detect the presence of extended emission around HL Tau and R Mon, which they attribute to the scattering of light from dust within halo structures around these stars. The dimensions of these dust distributions are 320×200AU (HL Tau) and 1300×1300AU (R Mon).

Chapter 3

Polarisation and Polarimetry

Many physics textbooks offer a discussion on the nature of polarised light at various levels of sophistication (see, for example, Hecht 1987 for a lucid treatment) and so a description here is not warranted. The mathematical formulation is particularly relevant since the measurement of astronomical polarisation involves the determination of the Stokes parameters of the incident light. Astrophysically important sources of polarisation include the intrinsic polarisation of synchrotron emission, the scattering of light by small particles and the selective extinction of light by regions of aligned anisotropic dust grains. In regions of SF the most common source of polarisation is the scattering of light from dust grains and this mechanism, in combination with polarisation by extinction (aligned grains) can account for all of the optical polarisation measurements to be described shortly. Consequently, other polarising mechanisms will be neglected. The theory of the scattering of light from dust grains is a complicated issue (Greenberg 1978, van de Hulst 1957) and since no attempt has been made to numerically model the data to be presented it is not necessary to go into the quantitative details here. However, looking ahead slightly, one of the main themes to emerge in the qualitative analysis of the polarisation data is the importance of polarisation by extinction in regions of SF where the local magnetic field is capable of aligning dust grains. The polarisations arising from such magnetically aligned grains allow a determination of the magnetic field geometry (projected onto the plane of the sky) the implications of which are discussed in chapter 7 for SF regions in general. The processes by which grains may be magnetically aligned are, therefore, most relevant

60

and are now discussed.

3.1 Polarisation by Extinction

For polarisation by extinction to occur, two requirements are necessary. Firstly, the dust grains must in some way be optically anisotropic, that is, the cross sections for absorption and scattering must differ between orthogonal axes. This is most easily achieved if the dust grains are flattened or, in the more extreme case, needle shaped. Secondly, the grains have to be aligned so that a net effect can be observed.

It is now generally accepted that grain alignment in the ISM is achieved by means of the Galactic magnetic field *via* the mechanism of paramagnetic relaxation suggested by Davis and Greenstein (1951). Over the years, and in parallel with increasingly sophisticated models of interstellar grains, the original Davis-Greenstein (DG) theory has been slightly modified in order to more accurately accommodate aspects of the accumulated polarisation data.

Paramagnetic relaxation occurs when a paramagnetic substance is placed in an alternating magnetic field of high enough frequency or, conversely, if it rotates rapidly in a static field. In either case, if the relaxation time of the magnetic dipoles is long compared with the timescale on which the field changes occur then the magnetisation will lag behind the field (Morrish 1965). The introduction of such a phase lag, ϕ, leads to a complex form for the magnetic susceptibility, $\chi = \chi' + i\chi''$, where $\chi'' = \chi' \tan \phi$. The component of the magnetisation associated with the aligning torque $\mathbf{L}$ is then that component associated with χ''. Since $\mathbf{L} = \mathbf{M} \wedge \mathbf{B}$ it can be shown that $\mathbf{L} = \frac{\chi''}{\omega}(\omega \wedge \mathbf{B}) \wedge \mathbf{B}$, where ω is the angular velocity of the spinning paramagnetic grain (Spitzer 1978, for example). It can be seen that this torque acts perpendicularly to the magnetic field reducing the component of angular momentum in this direction and causing the spin axis of the grain to line up with the magnetic field.

Within the context of the ISM, the alignment of a thermally spinning grain by this mechanism depends primarily upon two quantities, η and δ. η is a ratio of temperatures, T_{gra}/T_{rot} where T_{gra} is the internal temperature of the grain and T_{rot} is the 'rotation temperature' of the grain. T_{rot} depends on the temperature of the gas since it is assumed that the grain

spins up on collision with the gas atoms (this is called thermal spinning alignment—TSA). For paramagnetic relaxation (DG alignment) to occur, the gas temperature must be greater than that of the dust so that the external field variations dominate the thermal fluctuations of the dipoles. When $T_{gra} = T_{rot}$ no alignment is possible and when $T_{gra} > T_{rot}$ 'inverse' DG alignment is predicted where the angular momentum vector precesses in a plane perpendicular to the field direction (Greenberg 1978). δ is a ratio of characteristic times, τ_c/τ_m, where τ_c is a timescale for collision of the grain with gas atoms and τ_m is a timescale for magnetic grain alignment. Although gas-grain collisions are necessary to provide the rotational energy in the TSA model, such collisions also randomise the grain orientation so that, if a net alignment is to be observed, they cannot be too frequent. Therefore, we should have $\tau_c > \tau_m$.

It is thought that both the above conditions ($\eta < 1$, $\delta > 1$) are satisfied in the hot rarefied gas of the ISM so that DG alignment should be at least qualitatively successful in these regions. However, in order to explain polarisation by extinction in dense molecular clouds and, *ipso facto*, SF regions, it may be necessary to modify the basic (TSA) DG mechanism. The temperature constraint, $T_{gra} < T_{rot}$, is particularly inhibitive in cloud regions since it is expected that the dense gas will be efficiently cooled by molecular line radiation (Goldreich and Kwan 1974). In addition, the dust may be thermally heated by young stars so as to prevent TSA occurring at all. In the case of molecular clouds, a more attractive variation of the DG alignment mechanism is available in the form of 'suprathermal spinning' alignment (SSA instead of TSA) or 'pinwheel' alignment (Purcell 1979). When hydrogen atoms collide with a grain, some of them may stick to the grain and diffuse over its surface. If these hydrogen atoms then combine exothermally at specific catalytic sites on the grain surface, then a significant proportion of the binding energy of the H_2 molecule may become available ($0.2 \rightarrow 2\text{eV} \equiv$ ejection velocity of $4 \rightarrow 14\text{kms}^{-1}$—Spitzer 1978). If the recombination sites are unevenly distributed over the grain surface, as seems likely, then the ejection of the H_2 molecules will result in an unbalanced torque causing the grain to spin. Angular velocities $\sim 10^9\text{rad s}^{-1}$ (Purcell 1979)—much greater than those possible assuming thermal rotation— can be achieved by this method. The advantage of SSA in the treatment of SF regions is that the temperature constraint $T_{gra} < T_{rot}$ is circumvented since suprathermal spinning corresponds to thermal spinning at a gas tem-

ning at a gas temperature of $\sim 10^4$K. However, an additional constraint is imposed in its place. When considering SSA, it is important that grain re-surfacing or erosion does not occur on a timescale comparable with or less than τ_m, the timescale for magnetic alignment. When re-surfacing occurs, the active catalytic sites on the grain will move about causing a change in the spin axis. The grain will spin down and the angular velocity may 'cross-over' through zero and reverse sign. It is found that the efficiency of SSA depends on the frequency of these cross-overs. Spitzer and McG-lynn (1979) show that complete disorientation of the grain occurs in two or three cross-overs so that for effective alignment, the suprathermal spin up process must be long lived relative to τ_m. In the ISM this is unlikely to be a problem since denudation by UV radiation should prevent the formation of grain mantles and ensure that grains are stripped to their refractory cores. However, in the UV-shielded interiors of molecular clouds the re-surfacing of grains, especially by the formation of icy mantles (Johnson 1982) may become a problem. In these regions it must also be assumed that there is sufficient hydrogen available in atomic form to drive the SSA process. Further evidence for SSA is provided, for example, by detailed investigation of the interstellar polarisation curves (Aannestad and Greenberg 1983) and the uncomfortably high magnetic field levels predicted by TSA (see Cugnon 1987 for a review).

3.2 Imaging Polarimetry

The Durham Imaging Polarimeter is an instrument designed to map the linear polarisation of extended astronomical objects. Its construction and method of operation and the way in which the polarisation information are extracted from the observations have been described at length elsewhere (Scarrott *et al.* 1983). In 1984, the polarimeter was interfaced with a CCD detector system based on a GEC P8600 'thick' chip (Wright and MacKay 1981) to form the 'CCD Imaging Polarimeter System', which is described by Draper (1987). The chip has a red response up to $\approx 1\mu$m, negligible fringing problems and a low read-out noise (typically 8 electrons pixel^{-1}) and so the CCD-polarimeter combination is an ideal probe of faint, obscured and highly polarised regions of SF.

The 'dual beam' nature of the polarimeter allows the object to be si-

multaneously imaged in orthogonal polarisation states so that variations in the transparency of the night sky can be corrected for. In order to do this, a set of four such double exposures is required so that, in total, at least eight polarisation measurements of the object are made. This process also allows the elimination of possible differences in the sensitivities of the two polarimeter channels. From these eight images, the I, Q and U Stokes parameters, and therefore all the necessary information for the determination of linear polarisation, may be obtained. A natural 'by-product' of this form of integral polarisation measurement (as opposed to aperture polarimetry) is the production of a final total intensity image as well as a polarisation map (hence 'imaging' polarimetry).

When observing, each separate exposure is kept reasonably short (typically 5 minutes) in order to minimise data contamination by sporadic events such as cosmic ray air showers and the effects of cumulative telescope tracking errors. Moving the telescope between sets of four exposures allows all of the object to be covered. The different fields can be aligned using common stars and combined during the data reduction stage. Also, since the number of exposure sets that can be combined is indefinite, the 'depth' of the final image is constrained only by the available telescope time and not by the saturation limit of the CCD.

All of the data to be presented have been reduced using image processing software developed for the Durham polarimeter. A standard reduction technique is employed throughout and any minor deviations from this procedure are indicated as they arise. The philosophy and details of the reduction technique are discussed by Warren-Smith (1979).

For reference in later chapters, the spectral responses of the polarimeter filters are given in Table 3.1.

Filter	Mean λ (nm)	Peak λ (nm)	FWHM (nm)
None	680	720	345
V	556	532	90
R	669	647	172
Re	670	632	111
I	784	745	125
Z	933	928	65

Table 3.1: Spectral responses of various filters when combined with a response typical of the P8600 chip used in the CCD Polarimeter.

Chapter 4

The Haro 6-5 System

The Haro 6-5 system lies in the vicinity of the B216 and B217 condensations within the dark cloud complex in Taurus (Heyer *et al.* 1987a) which is estimated to be at a distance of 140pc (Elias 1978). The Taurus complex extends over approximately 900pc^2 and contains many features typical of a region of prolific low mass SF such as condensed cloud cores, embedded IR sources, T Tauri stars, molecular outflows, HH objects, optical nebulosity and emission line jets. Haro 6-5 (also known as FS Tau) has been classified as a T Tauri star (Haro 1953) and Cohen and Kuhi (1979) estimate a bolometric luminosity of 1.3L$_\odot$ for this star. The coordinates of Haro 6-5 are $\alpha(1950)$=4^h 18^m 57.6^s $\delta(1950)$=26° 50' 32" from Strom *et al.* (1986).

4.1 Previous Observations

Mundt *et al.* (1984) present multi-waveband CCD imaging of the region surrounding Haro 6-5 and report the detection of an emission line jet. They associate this jet with a nearby star-like object located at the apex of a small triangular reflection nebulosity approximately 20 arcsec west of Haro 6-5. They designate this object Haro 6-5B suggesting that it lies at the centre of a bipolar outflow and is probably, therefore, the energy source for the jet. The jet consists of two bright knots (designated A and B by Mundt *et al.* 1987) linked by fainter nebulosity and appears curved in the images of Mundt *et al.* (1984) so that knot B (the closer of the two to Haro 6-5B) is not colinear with knot A and Haro 6-5B.

Observations by Mundt *et al.* 1987 with a spectrograph slit oriented

along the line joining Haro 6-5B and knot A (PA 53 deg.) confirm the emission line nature of the jet and show that knot A possesses a spectrum typical of HH objects. In contrast, the spectrum of knot B appears relatively featureless and is therefore unusual. The line emission from knot A and the fainter regions of the jet to the north-east of Haro 6-5B is blue shifted with heliocentric radial velocities in the range $-30 \rightarrow -70$km s^{-1}. Detection of red shifted emission from the region to the immediate southwest of Haro 6-5B indicates the presence of a counter jet and reinforces the earlier suggestion of bipolarity in the nebulosity associated with Haro 6-5B. These authors also detect strong Hα and FeII line emission from the triangular reflection nebulosity to the north-east of Haro 6-5B suggesting that if this star is the illuminator, then it is probably an emission line T Tauri star. Both Haro 6-5 and Haro 6-5B are VLA 6cm continuum sources (Brown *et al.* 1985)

Vrba *et al.* (1985) present visual and JHKL photometry of Haro 6-5 and Haro 6-5B and note that Haro 6-5 exhibits IR colours typical of T Tauri stars such as DG and HL Tau—both strong candidates for the possession of dusty circumstellar discs (e.g. Beckwith *et al.* 1984). Haro 6-5B shows a relatively flat spectrum between 1 and 3μm and appears less heavily reddened than Haro 6-5. Optical polarimetry of Haro 6-5 by these authors reveals a level of polarisation of 3.3 per cent at PA 93 deg.

Strom *et al.* (1986) identify Haro 6-5 with the IRAS source 04189+2650 and note that, in order to account for all of the observed FIR flux, this star should have a bolometric luminosity of ≈ 3.8L$_\odot$. These authors also present narrow band [SII] CCD images of the Haro 6-5 system which show the blue shifted emission line jet, red shifted counter-jet and velocity discontinuity centred on Haro 6-5B in agreement with Mundt *et al.* (1987)

4.2   New Observations

Polarimetric data on the Haro 6-5 system were obtained using the Durham CCD Imaging Polarimetry System (§3.2) in conjunction with the 1m telescope of the Wise Observatory, Israel and the 2.5m Isaac Newton Telescope (INT) on 1985 Feb 22 and 1987 Jan 2 respectively.

It is probable that the INT data are contaminated at low light levels by the scattering of extraneous (i.e. dome originating) light into the telescope

Observatory	Wise Obs.	INT
Tel. Aperture	1m	2.5m
Focus	f/13.5	f/15
Date	1985 Feb 22	1987 Jan 2
Image Scale ("/pix)	1.202	0.434
Filter	R	R
Exp. time	300s	500s
No. of exp.	12	12

Table 4.1: A summary of the Haro 6-5 polarimetric observations. For filter passbands see Table 3.1. The exposure times are a rough guide only since the depth of the final image depends upon the degree of overlap between the component fields.

beam during observations and this effect has been compensated for by the use of non-linear fits to and subsequent subtraction of the sky background.

The observations are summarised in Table 4.1 and the data were reduced in the manner outlined in §3.2

4.2.1 Wise Observatory Data

Figure 4.1 shows a brightness contour and polarisation map of the Haro 6-5 system in the R waveband derived from the Wise Observatory data. The contours are spaced logarithmically at intervals of 0.35 magnitudes and various features to be discussed below are indicated. Illuminating centres in the system are labelled Haro 6-5A, B and C. Each vector represents an integration over a 3 pixel ($\approx$ 3.6 arcsec) square bin, the inter-bin spacing being 2 pixels ($\approx$ 2.4 arcsec). The vectors are plotted in the conventional manner, parallel to the **E** field.

In Figure 4.1, the star Haro 6-5 appears as the dominant stellar luminosity peak embedded in surrounding nebulosity. Henceforth, this star will be designated 'Haro 6-5A'. Approximately 15 arcsec to the west of Haro 6-5A lies the triangular patch of reflection nebulosity referred to in §4.1, with the unresolved brightness knot Haro 6-5B at its south-western apex. Nebulosity exists further to the south-west of Haro 6-5B and appears as an arcuate structure containing two brighter condensations. This nebulosity is seen

to be somewhat detached from the main body of nebulosity surrounding Haro 6-5A and Haro 6-5B, as evidenced by the 'pinching' of the brightness contours between the two regions.

The emission line jet of Mundt *et al.* (1987) extends to the north and east of Haro 6-5B with the brightness peak in our image at position (-26,20) in an arcsec coordinate system centred on Haro 6-5B. This peak corresponds to knot A of the Mundt *et al.* (1987) jet and it lies at PA $\approx$ 53 deg. with respect to Haro 6-5B. This is the region of the jet most prominent in the contoured image. The elongated structure labelled 'arc 1' is $\approx$ 40 arcsec in length at PA 19 deg. and seems to be a continuation of the north- eastern edge of the triangular nebulosity close to Haro 6-5B. A fainter nebulous arc stretches between the north eastern extremities of the jet and arc 1 structures and appears to bridge the gap between these two regions. There is also evidence in Figure 4.1 for the presence of a further nebulous arc (labelled 'arc 2') extending from the south- eastern edge of the triangular nebula for $\approx$ 40 arcsec at PA 87 deg. However, this feature is rendered less obvious by its line of sight coincidence with nebulosity close to Haro 6-5A.

The broad R band contour map in Figure 4.1 is similar to the narrow R band CCD images of Mundt *et al.* (1984) as would be expected. However, there *are* subtle differences between the two sets of data which, presumably, result from the different pass-bands used as well as the differences in image scale and resolution. The arc and bridge of nebulosity to the north-east of Haro 6-5B are not evident in the images of Mundt *et al.*, whereas we barely detect the fainter and inner knot B regions of the jet. It is possible that the inner jet regions are not distinct in our broad R image due to the superposition of the bright nebulosity associated with Haro 6-5A and B.

The polarisation map shows high levels of linear polarisation throughout the whole of the Haro 6-5 system, a situation that is typical of reflection nebulosity in which polarisation is induced by the scattering of light from dust grains. A polarisation of 20 per cent appears to be representative for the system although this value is substantially reduced in certain localities.

The star Haro 6-5A illuminates the nebulosity to its immediate south, as is indicated by the symmetry of the polarisation pattern in this region. The influence of Haro 6-5A on the remainder of the encompassing nebulosity is, however, much less obvious. The arc 1 and bridge nebulosities to the north and east of Haro 6-5B show a roughly centrosymmetric polarisation pattern
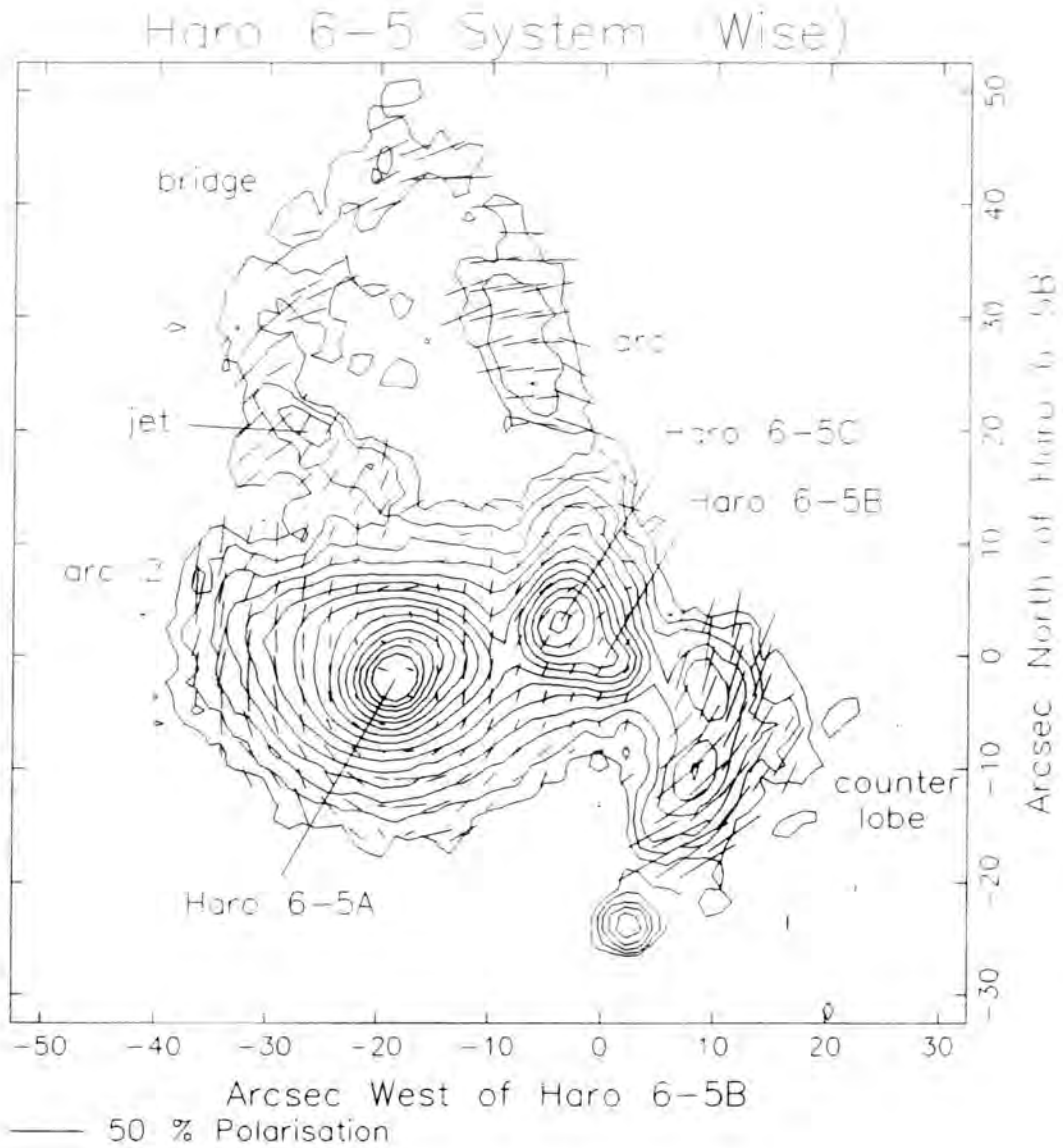
Figure 4.1: A brightness contour and polarisation map of the Haro 6-5 system in the R waveband, derived from Wise Observatory data and described in the text.

centred on the region of the triangular nebula neighbouring Haro 6-5B, suggesting that the dominant illuminating source is located here. A least-squares fit to the polarisation vector orientations in the arc 1 and bridge regions gives an optimum source position for these outlying nebulosities within the bright central region of the triangular nebula. This centre of illumination is designated Haro 6-5C and appears to be a discrete source quite distinct from (and, from our viewpoint, brighter than) Haro 6-5B, which lies ≈6 arcsec to the south-west. On this basis a source at the location of Haro 6-5B seems unlikely as an illuminator of these outlying nebulosities.

The polarisation pattern overlying the triangular nebula housing Haro 6-5C is not completely centrosymmetric and is, therefore, difficult to reconcile with polarisation induced purely by the single scattering of light from a nearby point source. However, the slight curvature evident in this pattern suggests illumination from the direction of Haro 6-5B to the south-west, but the degree of curvature is such that the source position would lie some way beyond the position of Haro 6-5B itself (if polarisation by simple scattering is assumed). The brightness knot at the position of Haro 6-5B (which is assumed to be the unresolved stellar image) is polarised at a level and orientation similar to that of the triangular nebula immediately to the north-east.

4.2.2 INT Data

Figure 4.2 shows brightness contour and polarisation maps of the Haro 6-5 system in the R waveband derived from INT observations. The contours are spaced logarithmically at 0.6 magnitude intervals and the illuminating sources are labelled as in Figure 4.1. The polarisation vectors correspond to integration over 7 pixel (≈ 3 arcsec) square bins with inter-bin spacing of 5 pixel (≈ 2.2 arcsec). A cut in total intensity is imposed below which no vectors are plotted. Figure 4.3 shows an increased spatial resolution polarisation map of the central brighter regions of the Haro 6-5 system. In this map the integration bins are 5 pixels square with an inter-bin spacing of 3 pixels (≈ 1.3 arcsec).

The nebular structure appears much the same as that discussed in the previous section in connection with the Wise Obs. data. The most noticeable differences (arising from changes in the seeing and image scale) are
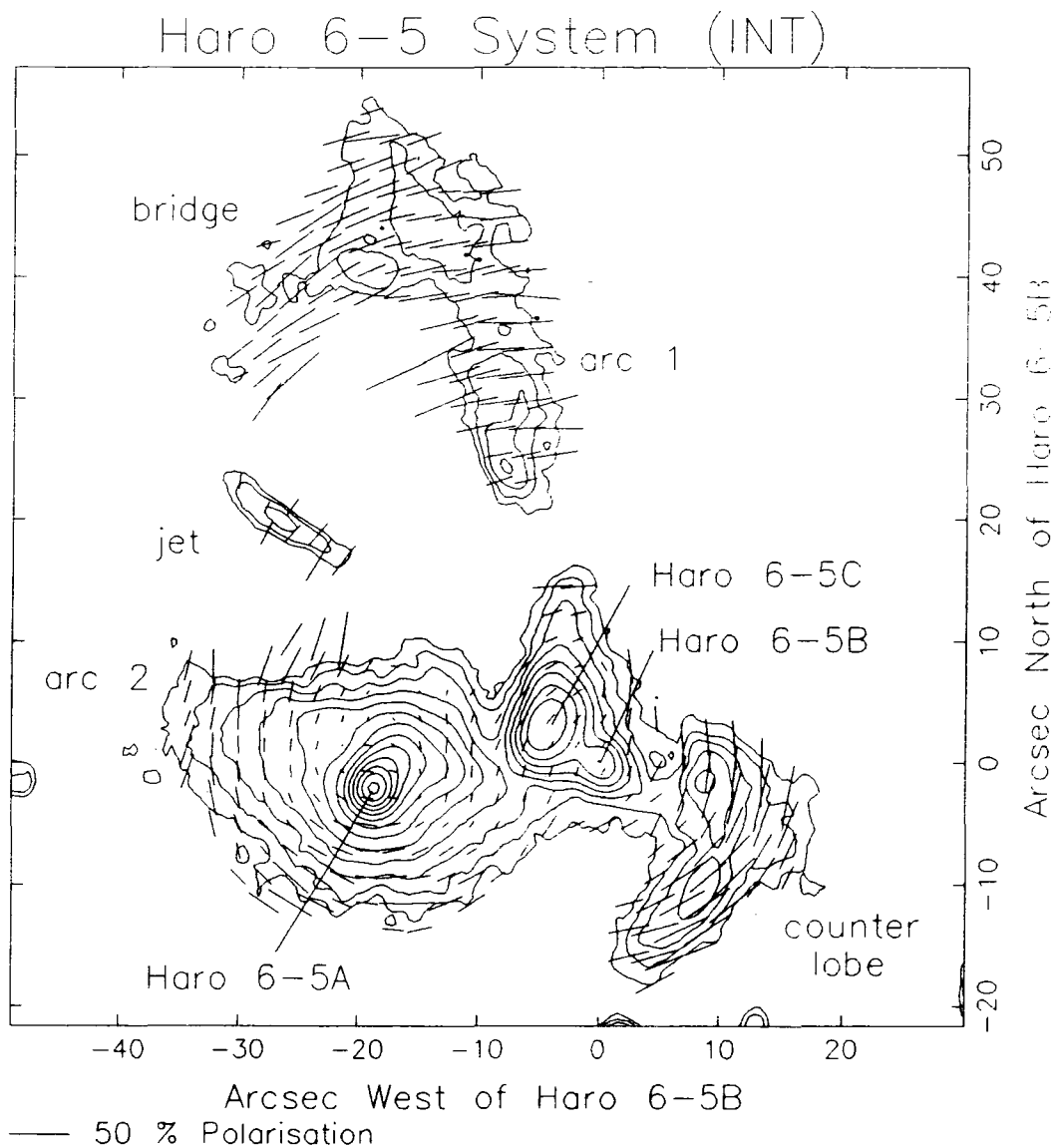
Figure 4.2: Brightness contour and polarisation maps of the Haro 6-5 system in the R waveband derived from INT data.

that the star, Haro 6-5B, now appears to be resolved from the surrounding nebulosity and the edges of the triangular nebula are now quite sharp, whereas they appeared rounded in the lower resolution Wise Obs. data. Also in these data, Haro 6-5B is seen to be embedded *within* the south-western apex of the triangular nebulosity. The two condensations in the counterlobe nebulosity are also now clearly visible.

The east-west elongation of the intensity contours to the north of Haro 6-5A provides evidence for an arc-like extension to the south-eastern edge of the triangular nebula (arc 2 in Figure 4.2). However, on the basis of the intensity data alone, it is very difficult to decide which regions of the nebulosity surrounding Haro 6-5A are associated with this star and which with Haro 6-5B.

The polarisation map of the central regions of the Haro 6-5 system in Figure 4.3 agrees completely with the equivalent field of Figure 4.1, confirming that the two independently obtained data sets are consistent. The polarisations overlying the triangular nebula are again seen to be not totally consistent with polarisation due purely to the scattering of light originating from the position of Haro 6-5B. Instead, the vectors show levels and orientations similar to those overlying Haro 6-5B itself. Now that the image of Haro 6-5B has been resolved, its polarisation may be more confidently measured. The results for Haro 6-5A, B and C are given in Table 4.2 along with the measurement of Vrba *et al.* (1985).

These authors also calculate a mean linear polarisation of 1.8 per cent at PA 23.5 deg. for ten background stars (selected from the catalogue of Moneti *et al.* 1984) located within 1 deg. of the Haro 6-5 system. However, a polarisation of 1.8 per cent is much greater than the expected interstellar polarisation at the distance of the Taurus clouds (about 0.4 per cent assuming a distance of 140pc and 3 per cent per kpc) suggesting that this polarisation is induced mainly by dust associated with the cloud complex itself. This interpretation is supported by the observed orthogonality of the magnetic field orientation and the direction of elongation of many of the cloud condensations within the Taurus association (Moneti *et al.*). The figure of 1.8 per cent then represents the polarisation along a line of sight to the back surface of the Taurus clouds (since the measured field stars are almost certainly background objects) and the polarisation to the front surface of the clouds will be considerably less. Since the location of the Haro 6-5 system relative to the front and back surface of the Taurus clouds
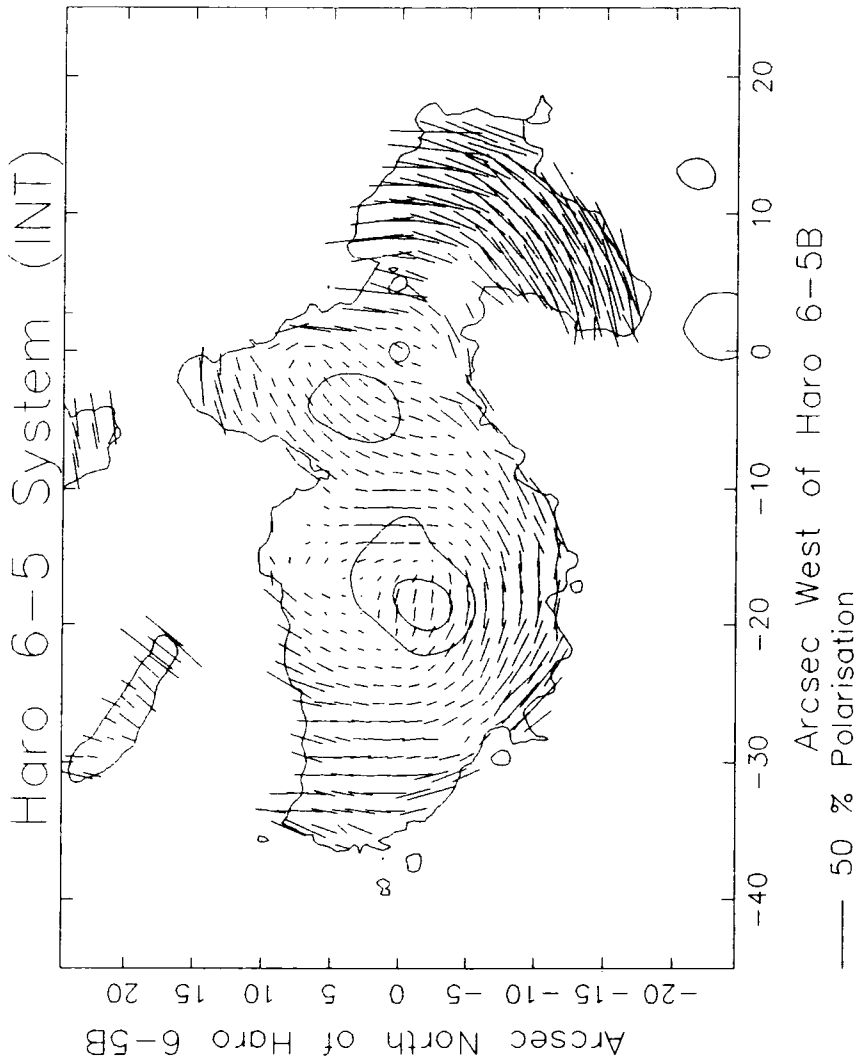
Figure 4.3: A polarisation map of the central regions of the Haro 6-5 system, as discussed in the text.

Data	Haro 6-5 Source	Date	Aperture (arcsec)	P (%)	PA (deg.)
Wise	A	22/2/85	5	8.4 ± 0.4	75 ± 2
Wise	B	"	"	7.7 ± 1.6	149 ± 6
Wise	C	"	"	10.3 ± 0.7	144 ± 2
INT	A	2/1/87	5	10.1 ± 0.5	82 ± 1
INT	B	"	"	7.2 ± 1.5	150 ± 6
INT	C	"	"	10.9 ± 0.6	142 ± 2
Vrba	A	14/3/85	?	3.3	93

Table 4.2: Polarisation measurements of the Haro 6-5 sources using a circular aperture of diameter 5 arcsec. The Wise and INT data are taken through R band filters (Table 3.1). The data of Vrba *et al.* 1985 is unfiltered.

is unknown, no correction for 'interstellar' polarisation has been made.

The counterlobe nebulosity to the south-west of Haro 6-5B shows very high levels of polarisation (typically 30 → 40 per cent and up to 50 per cent in places) and a centrosymmetric vector pattern consistent with illumination by Haro 6-5B. This observation diminishes the likelihood of a centre of illumination to the south-west of Haro 6-5B for the triangular nebulosity, since such an illuminator would be expected to influence the polarisation pattern of the counterlobe region—an effect not observed.

A most noticeable feature in the polarisation map of Figure 4.3 is the band of parallel polarisation vectors overlying Haro 6-5A itself. To the immediate west of this parallel band there is evidence for a null point in the polarisation pattern. There is no obvious corresponding null point to the east of Haro 6-5A.

As noted previously, the region of nebulosity to the south (and east) of Haro 6-5A appears to be directly illuminated by this star. The region to the south-west of Haro 6-5A, although in general showing lower levels of polarisation than in the south and south-east, may also be interpreted as reflection nebulosity associated with Haro 6-5A. The region to the north of Haro 6-5A shows lower levels of polarisation and evidence for another null point and is clearly complex in that the polarisation pattern cannot be attributed to the scattering of light from any one of the hitherto known sources in the field (*i.e.* Haro 6-5A, B or C). The region to the north-east

of Haro 6-5A appears to be illuminated from the direction of Haro 6-5B or C.

4.3 Interpretation

Before proceeding to an interpretation of the data, the main features noted so far will be summarised

1. The polarisation patterns in the vicinity of the stars Haro 6-5A and Haro 6-5B are inconsistent with centrosymmetric scattering patterns. A band of parallel polarisation overlies Haro 6-5A. Both stars are significantly polarised, the polarisation angle of Haro 6-5B being perpendicular to the jet axis.

2. There is evidence for at least *three* sources of illumination within the Haro 6-5 system: The star Haro 6-5A illuminates nearby nebulosity to the south and possibly also to the north. The star Haro 6-5B illuminates the counterlobe nebulosity to its south-west and probably the triangular region of nebulosity to its north-east. The brightness peak Haro 6-5C at the centre of the triangular nebula illuminates the outlying arc 1 and 'bridge' nebulosities.

3. The polarisation of the triangular region of nebulosity cannot be explained in terms of simple scattering of light originating from any of the three known sources of illumination in the system.

4. The nebulosity to the north of Haro 6-5A is polarised in a complex manner indicating that scattered light from more than one illuminator contributes to this region or that more than one polarising mechanism is operative (or both).

4.3.1 Evidence for Circumstellar Discs

A significant polarisation has been measured for the star Haro 6-5B (Table 4.2) which is similar in degree and orientation to that overlying the triangular nebula to its north-east. Since it has been shown that the triangular nebula houses Haro 6-5C, the illuminator of the outlying nebulosity in the system, this suggests that Haro 6-5B is intimately associated with

and an integral part of the Haro 6-5 system as a whole, and not just a foreground or background object.

4.3.1.1 The Polarisation Map

In view of the polarisation of Haro 6-5B, the quasi-centrosymmetric nature of the vector pattern overlying the neighbouring triangular nebula may now be seen as evidence for the presence of two competing polarising mechanisms in this region. This phenomenon has been found to occur frequently in the polarisation patterns close to the illuminating sources of cometary and bipolar nebulae and has previously been interpreted as evidence for circumstellar discs containing grain-aligning magnetic fields (for example. Scarrott *et al.* 1987d).

In such situations it is proposed that a circumstellar disc (in this case a disc around the star Haro 6-5B) is threaded by a predominantly toroidal magnetic field (*i.e.* a field component in the plane of the disc). Alignment of the dust grains within the disc by this magnetic field (*via* the DG mechanism, discussed in §3.1) ensures that light from regions viewed through the disc carries a component of polarisation by extinction parallel to the plane of the disc, superimposed on any existing polarisation. When the disc overlies reflection nebulosity illuminated by a central source (for example, Haro 6-5B) then a centrosymmetric vector pattern, typical of scattering from such a source, is seen in conjunction with polarisation induced by the extinction of light within the disc. The result is a pattern characterised by a band of parallel vectors overlying the illuminating source that becomes more and more centrosymmetric with distance from this source, as the influence of the disc (and its extinction) diminishes. A further consequence of this polarisation model is the generation of two null points in the vector pattern in the equatorial plane of the disc. These points define the positions at which, relative to the line of sight to the observer, the two polarising mechanisms act in antagonistic fashion and to equivalent extent such that the resultant polarisation is exactly zero.

Alternatively, the quasi-centrosymmetric or 'elliptical' nature of the vector pattern may be produced if the triangular nebulosity is illuminated by an intrinsically polarised source (Notni 1985). The 'intrinsic' polarisation is produced by anisotropic light scattering close to Haro 6-5B—the anisotropy

being created by a circumstellar disc. Null points in polarisation can be generated in the equatorial plane of the central disc, as with the aligned grain model and an appropriate geometry is discussed in chapter 7.

However, both mechanisms require the presence of a circumstellar disc oriented with equatorial plane parallel to the stellar polarisation. The polarisation map of Figure 4.3 therefore suggests that Haro 6-5B is surrounded and partially obscured by a circumstellar disc inclined with equatorial plane at PA $\approx$ 150 deg.

One possible way of distinguishing between the two polarising mechanisms is to subtract off the polarisation of the star from the map and to note the effect of this upon the vector pattern in the nebulosity close to the star. If the distortion of the scattering pattern is due to the polarising effects of a uniform distribution of overlying aligned grains, then a constant PA polarisation (the polarisation of the star) will have been 'added' to the polarisation due to scattering at each point in the nebula. The subtraction of this constant polarisation should therefore result in the restoration of a centrosymmetric scattering pattern. In the case of an intrinsically polarised source, the distorting effect is dependent upon the scattering geometry and will vary throughout the nebula with angular offset from the disc polar axis and the subtraction of a constant polarisation should not produce a centrosymmetric pattern. If a non-centrosymmetric pattern does result after the subtraction of the stellar polarisation it is still difficult to eliminate the effects of aligned grains since the precise extent of the disc and its influence on the polarisation pattern is not known (that is, the overlying dust will not be distributed uniformly). However, if a centrosymmetric pattern does result then this suggests that the distortion of the source region polarisation pattern is due to the effects of aligned grains.

On this basis, the polarisation of Haro 6-5B has been subtracted from the map of Figure 4.3 and the result is shown in Figure 4.4. The exercise appears partially successful in that the vector pattern overlying the triangular nebulosity now shows more evidence for a centre of symmetry coincident with Haro 6-5B than previously (a similar procedure applied to Haro 6-5C does not have the same effect). The resultant pattern is not strongly centrosymmetric, however, which suggests that either the effects of extinction toward the triangular nebula have been over-compensated for or that the light from Haro 6-5B is to some extent 'intrinsically' polarised. The counterlobe nebulosity, on the other hand, appears little changed and shows a

strongly centrosymmetric polarisation pattern centred on Haro 6-5B. This may simply be due to the large levels of polarisation associated with this nebulosity rendering the region insensitive to the polarisation subtraction.

The distortion of the polarisation pattern in the Haro 6-5A region, taking the form of a band of parallel vectors, has already been noted and, in the light of the preceeding discussion, may be taken as polarimetric evidence for the presence of a disc around this star. Further evidence for such a disc is provided by the existence of a null point in the polarisation pattern to the immediate west of the band of parallel vectors (at approximately (-17,-1) in the coordinate system of Figure 4.3). A corresponding equatorial null point to the east of Haro 6-5A is not seen, but this is probably due to the influence in this region of scattered light originating from Haro 6-5C (or B). The orientation of the vector band overlying Haro 6-5A in the INT data (and, indeed, the PA of the polarisation of the star itself) suggests that the equatorial plane of the disc lies at PA 82 deg. The effect of subtracting the polarisation of Haro 6-5A from the INT map is shown in Figure 4.5. The scattering pattern in the nebulosity to the south of Haro 6-5A is strengthened confirming this star as the illuminator and the null point previously seen to the west of Haro 6-5A disappears. This suggests that a component of the polarisation of Haro 6-5A does overlie and has been successfully removed from the nebulosity to the south of the star and that the distortion of the pattern in this region is due to the effects of overlying aligned grains.

4.3.1.2 Total Intensity Image

Further evidence for the existence of an obscuring disc around Haro 6-5B and an indication of its extent on the plane of the sky is afforded by the structure in the brightness contour map of Figure 4.2. The axis of the triangular nebulosity, as defined by the line joining the brightness peak Haro 6-5C to Haro 6-5B, is approximately perpendicular to the plane of the hypothesised disc as would be expected if this nebulosity is illuminated by Haro 6-5B through the polar regions of the disc. The detached nature of the counterlobe nebulosity is most easily explained if a disc associated with Haro 6-5B is inclined relative to the line of sight so that it overlies and obscures the region between this structure and Haro 6-5B. If the counterlobe and triangular nebulosities *do* define the cones of illumination imposed on

Figure 4.4: A polarisation map of the Haro 6-5B region derived from INT data and superimposed on selected brightness contours. The polarisation of the star has been subtracted from the map.
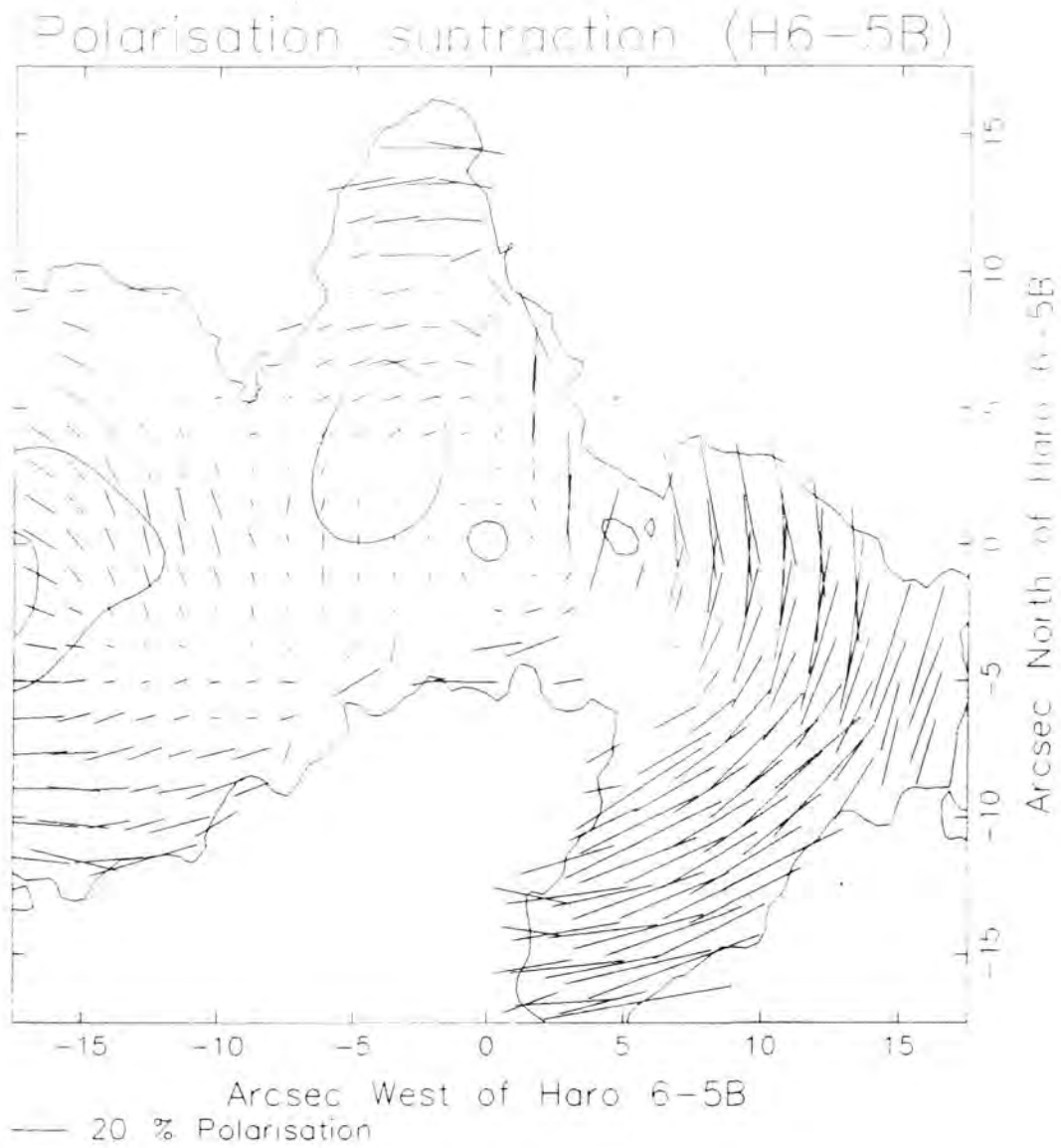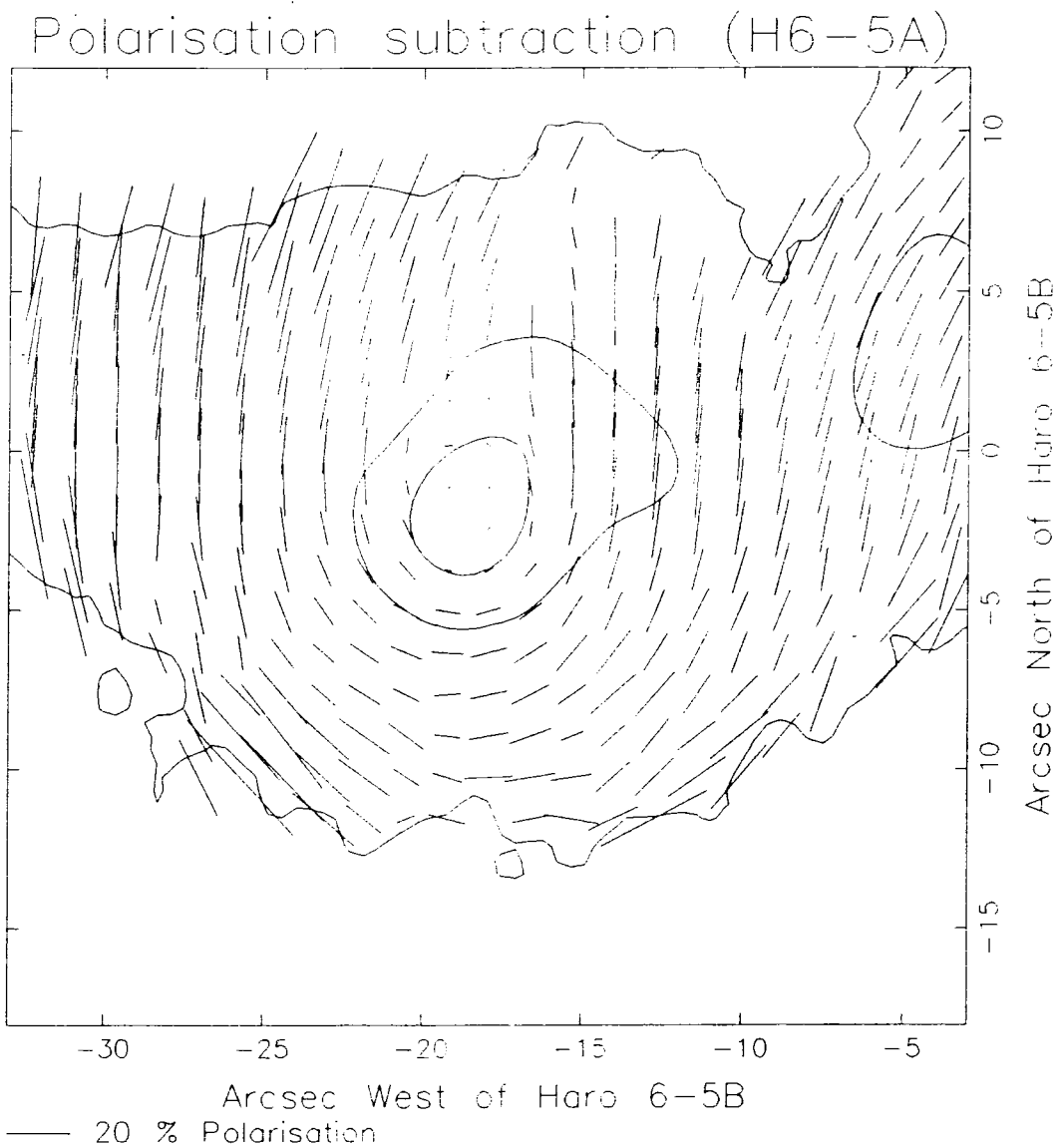
Figure 4.5: A polarisation map of the Haro 6-5A region derived from INT data and superimposed on selected brightness contours. The polarisation of the star has been subtracted from the map.

Haro 6-5B by the surrounding disc, then this inclination of the disc suggests that the counterlobe nebulosity is oriented into the plane of the sky whereas the triangular nebulosity projects out of the plane of the sky. Such a nebular tilt is endorsed by the velocity measurements of emission lines to the north-east and south-west of Haro 6-5B by Mundt *et al.* (1987).

The brightness contours shown in Figure 4.2 do not give a clear indication of a disc at the position of Haro 6-5A but instead show a general elongation of isophotes to the north-west of Haro 6-5A. These contours, however, give little indication of the relative importance of the known illuminating centres in this region and are not. therefore, a reliable basis on which to interpret polarisation attributable solely to Haro 6-5A. An analysis of the nebular structure associated with Haro 6-5A can be accomplished more easily by examination of the polarised intensity and colour data. It will now be shown that these data strongly support the postulation of a disc of obscuration around Haro 6-5A oriented with equatorial plane at PA 82 deg.

4.3.1.3 Polarised Intensity Image

Figure 4.6 shows contours of polarised intensity in the R waveband and the corresponding polarisation map of the brighter nebular regions (*i.e.* not including the outlying nebulosities) of the Haro 6-5 system, derived from INT data. The contours are spaced logarithmically at intervals of 0.5 mag.

The three illuminating sources and much of the nebular structure seen in total intensity can readily be identified in Figure 4.6. However, in the vicinity of Haro 6-5A several interesting features are evident. Firstly, the null point to the west of Haro 6-5A is clearly visible as a pronounced pinch in the polarised intensity contours immediately surrounding this star. Secondly, these contours are elongated in an approximately north-south direction. This elongation is consistent with (and, indeed, can be explained by) the postulation of a disc of obscuring material at PA 82 deg. Such a disc will constrain the illumination of the surrounding nebulosity by Haro 6-5A so that more light escapes in a north-south direction (through the polar regions of the disc) than in an east-west direction (through the equatorial regions).

The fan-shaped extension to the polarised intensity contours to the

south of Haro 6-5A is reminiscent of a cone of illumination of the nebulosity in this region by Haro 6-5A and supports the contended disc geometry.

4.3.1.4 R-I Colour Image

Figure 4.7 shows the R band INT polarisation map superimposed on contours of R-I colour index derived from the Wise Obs. data. The zero point of the contoured image is arbitrary and regions which are relatively redder or bluer than the zero point are labelled 'R' and 'B' respectively. The contours are spaced linearly at 0.05 magnitude intervals.

The three illuminators in the Haro 6-5 system are again quite clearly visible. Haro 6-5B appears slightly redder than its surroundings whereas Haro 6-5C is one of the bluest regions (as would be expected for the brightest part of a reflection nebulosity). Haro 6-5A is noticeable as the reddest object in the system and is surrounded by red contours elongated in approximately the same direction as the band of parallel vectors overlying the star. This elongated structure is most easily interpreted in terms of a layer of obscuration overlying and reddening Haro 6-5A. This provides direct evidence for the existence of a dusty circumstellar disc around Haro 6-5A oriented with equatorial plane at PA 82 deg. and is consistent with the indirect evidence provided by the total intensity and polarisation data.

The fan-shaped extension of the red contours to the south of Haro 6-5A is similar to the structure seen in polarised intensity in Figure 4.6. Two explanations for this structure are:

1. The disc around Haro 6-5A is inclined relative to the line of sight so that it overlies and reddens the region to the south of the star. If this is the case, then it may be expected that the polarisation pattern in the reddened region will contain a component of polarisation due to extinction and will not, therefore, appear as a perfect centrosymmetric scattering pattern. Instead, the pattern should appear flattened in the east-west direction—the direction of the proposed toroidal magnetic field in the disc— to an extent dependent upon the degree of extinction. Evidence for such an effect is seen in Figure 4.5 which shows the result of subtracting the polarisation of Haro 6-5A from the remainder of the map. The vector pattern is more like a
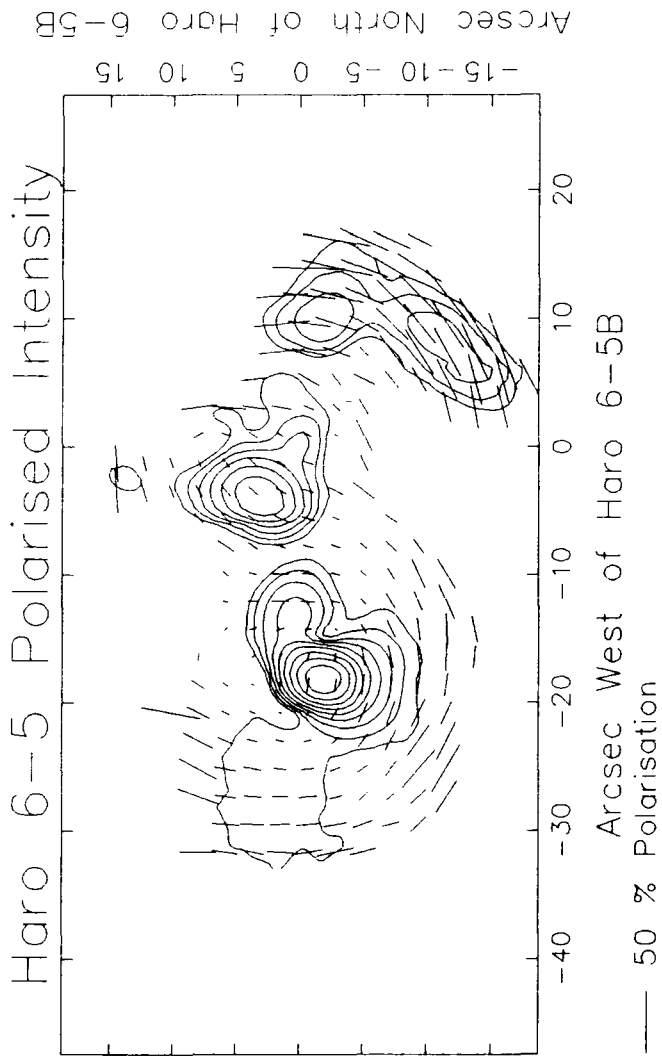
Figure 4.6: Contoured polarised intensity image and polarisation map of the central regions of the Haro 6-5 system in the R waveband, derived from INT data.

centrosymmetric pattern indicative of single scattering after the polarisation subtraction.

2. The star Haro 6-5A has an intrinsically red continuum spectrum and so the red contours simply delineate the regions of nebulosity illuminated by this star. The similarity between this fan-shaped region of contours and that seen in the polarised intensity image is now to be expected since both result from the scattering of light from Haro 6-5A.

It is possible that both effects are in operation. The nebular regions illuminated by Haro 6-5A may be relatively red and the region to the south of Haro 6-5A may be influenced by a component of the magnetic field thought to be associated with the disc around this star (although this does not necessarily entail a tilt of the disc relative to the line of sight). It has been noted in the case of other PMS systems (*e.g.* R Mon—Warren-Smith *et al.* 1987a) that the regions above and below circumstellar discs may be threaded by a magnetic field which links the disc field with the uniform large-scale cloud field.

The colour image provides little convincing evidence for the existence of an obscuring disc around Haro 6-5B. However, the effects of the obscuration around Haro 6-5B appear to be more pronounced than in the case of Haro 6-5A, as evidenced by the distinct paucity of light between the counterlobe nebulosity and the nebulosity surrounding Haro 6-5B. Since there is little information available in this region there can, therefore, be little evidence for (or against) the existence of a disc around Haro 6-B.

Two further noteworthy features are evident in Figure 4.7. The inner red contours associated with Haro 6-5A curve away from this star to the south-west in an arcuate fashion to form a 'spur' traceable for nearly 10 arcsec. A similar structure can be seen to the north-west of Haro 6-5A although in this case the contours can not be traced back to the star and, consequently, the structure appears somewhat detached.

4.3.2 The Illuminating Sources

It has been suggested that the arc 1 and bridge nebulosities of Figure 4.2 are illuminated by the optically bright source Haro 6-5C located at the centre of the triangular reflection nebula. However, since the triangular nebula appears to be illuminated by Haro 6-5B, some 6 arcsec to the south-west of Haro 6-5C, the relationship between the two sources and the nature of the latter source is not immediately clear. Both Haro 6-5B and Haro 6-5C are colinear with the elongated knot A of the emission line jet and form an axis at PA 53 deg. approximately perpendicular to the equatorial plane of the proposed obscuring disc.

Is Haro 6-5C a consequence of the illuminating/exciting effects of Haro 6-5B or is the situation reversed?

A plausible explanation is that the nebulosity in the Haro 6-5 system (excluding the Haro 6-5A region which will be discussed shortly) is illuminated by both Haro 6-5B and Haro 6-5C to differing extents. If Haro 6-5B is deeply embedded within a circumstellar disc, then the disc may control the illumination of the surrounding nebulosity by this star to such a degree that only regions lying very close to the polar axis of the disc receive significant light directly from Haro 6-5B. Hence, the extinction to Haro 6-5B increases rapidly with angular offset from the polar axis so that regions such as arcs 1 and 2 are illuminated primarily by Haro 6-5C. The bridge region appears more or less on the polar axis and so it is not possible to tell which is the dominant illuminator of this nebulosity.

In this scheme, Haro 6-5C would represent a region of intense scattering of the light originating from Haro 6-5B rather than (for example) an embedded star[1].

The counterlobe nebulosity appears to be illuminated solely by Haro 6-5B with no evidence for illumination by Haro 6-5C. This is consistent with the postulation of a dense circumstellar disc around Haro 6-5B which would be expected to block out the light from Haro 6-5C and prevent it from reaching the counterlobe region.

The polarisation pattern to the north of the star Haro 6-5A may be

---

[1]Vrba, Rydgren and Zak (1985) detect a peak in JHKL emission in the region and locate it 6 arcsec to the north-east of Haro 6-5B. However, there appears to be some confusion over the coordinates of this emission peak, which the above authors attribute to the star Haro 6-5B. In fact, an offset of 6 arcsec to the north-east of Haro 6-5B locates the IR peak at the position of the source Haro 6-5C
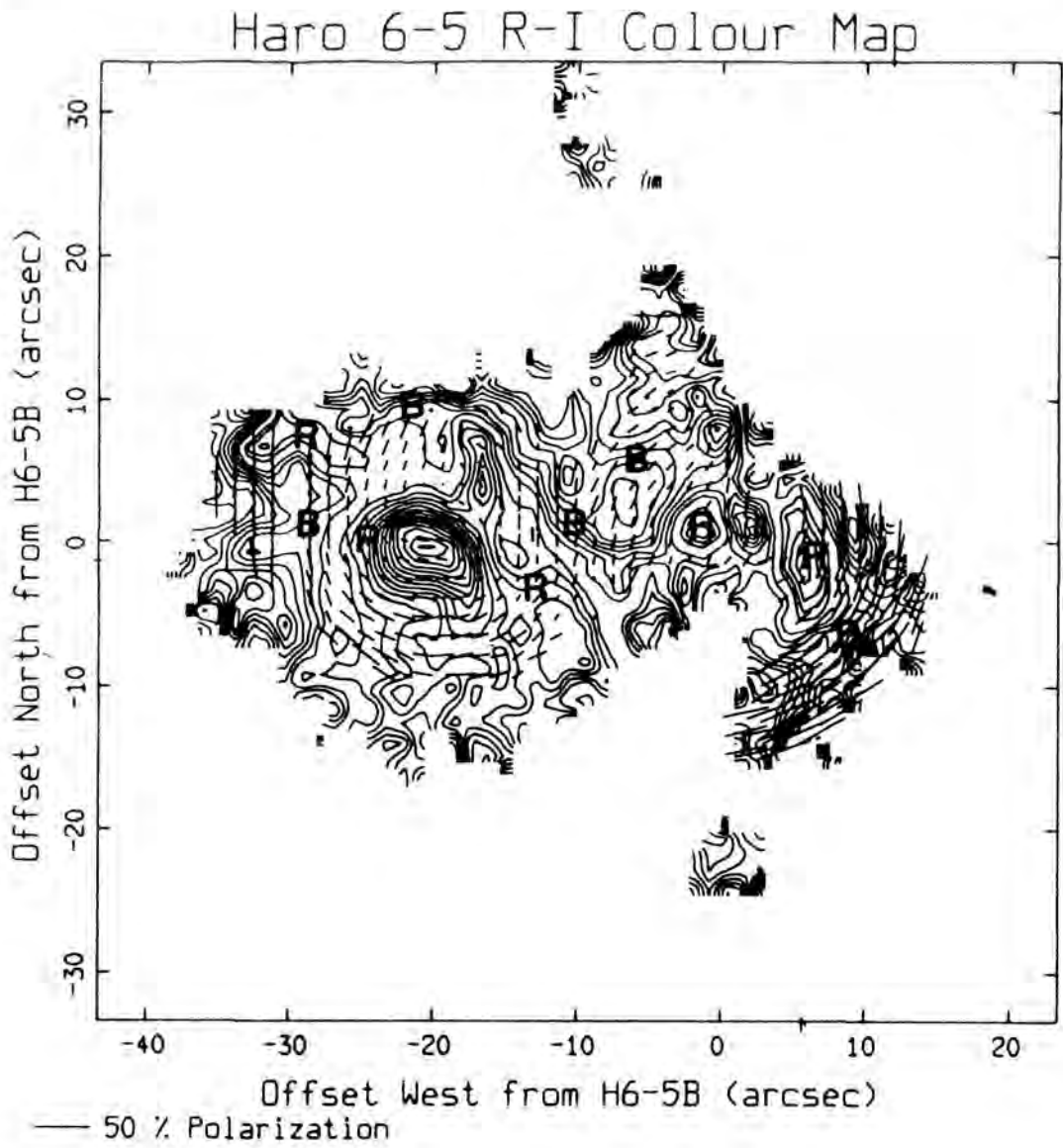
Figure 4.7: R band INT polarisation map and contoured R-I colour index from Wise Observatory data.

explained in terms of the superposition of two scattering patterns. One pattern is centrosymmetric about Haro 6-5C or B, the other about Haro 6-5A. A nebular geometry which could give rise to such a superposition will now be discussed.

4.3.3 The Proposed Geometry

It is proposed that the Haro 6-5 system has a geometry consisting of two nebulous bicones[2], one centred on Haro 6-5A and the other on Haro 6-5B, tilted relative to one another such that, on the plane of the sky, they appear to intersect to the north of Haro 6-5A. This geometry is illustrated schematically in Figure 4.8 and Figure 4.9 which also indicates the polarising influences held to be operative in each region. The two bicones and their equatorial discs are shown superimposed on the nebular outline. In this model it is supposed that a toroidal magnetic field exists within the discs and is responsible for the anomalous source region polarisation patterns discussed earlier. The orientation of the local cloud field is shown and important PAs are indicated. In the interest of clarity, only the Haro 6-5B bicone is outlined in Figure 4.9. The positions of the three illuminating sources are shown. The possible roles of the local magnetic field in the Haro 6-5 system will be discussed in §4.5.

4.3.3.1 The Haro 6-5B Bicone

The more easily distinguished bicone is the one centred about Haro 6-5B which also appears to be the larger of the two (whether this difference in size is real or an effect of projection or perspective is not yet clear).

The north-eastern cone is delineated by the edges of the central triangular nebula and by the nebulous arcs 1 and 2, the latter extending across the face of the nebulosity associated with Haro 6-5A. Evidence of the path traced by arc 2 (and, therefore, the edge of the north-eastern cone) can be seen in the total intensity image of Figure 4.2 as an east-west elongation of the brightness contours to the north of Haro 6-5A. In addition, the two apparently separate groups of contours in the polarised intensity image of

---

[2]The two solids are not *strictly* bicones since they possess finite diameter waists

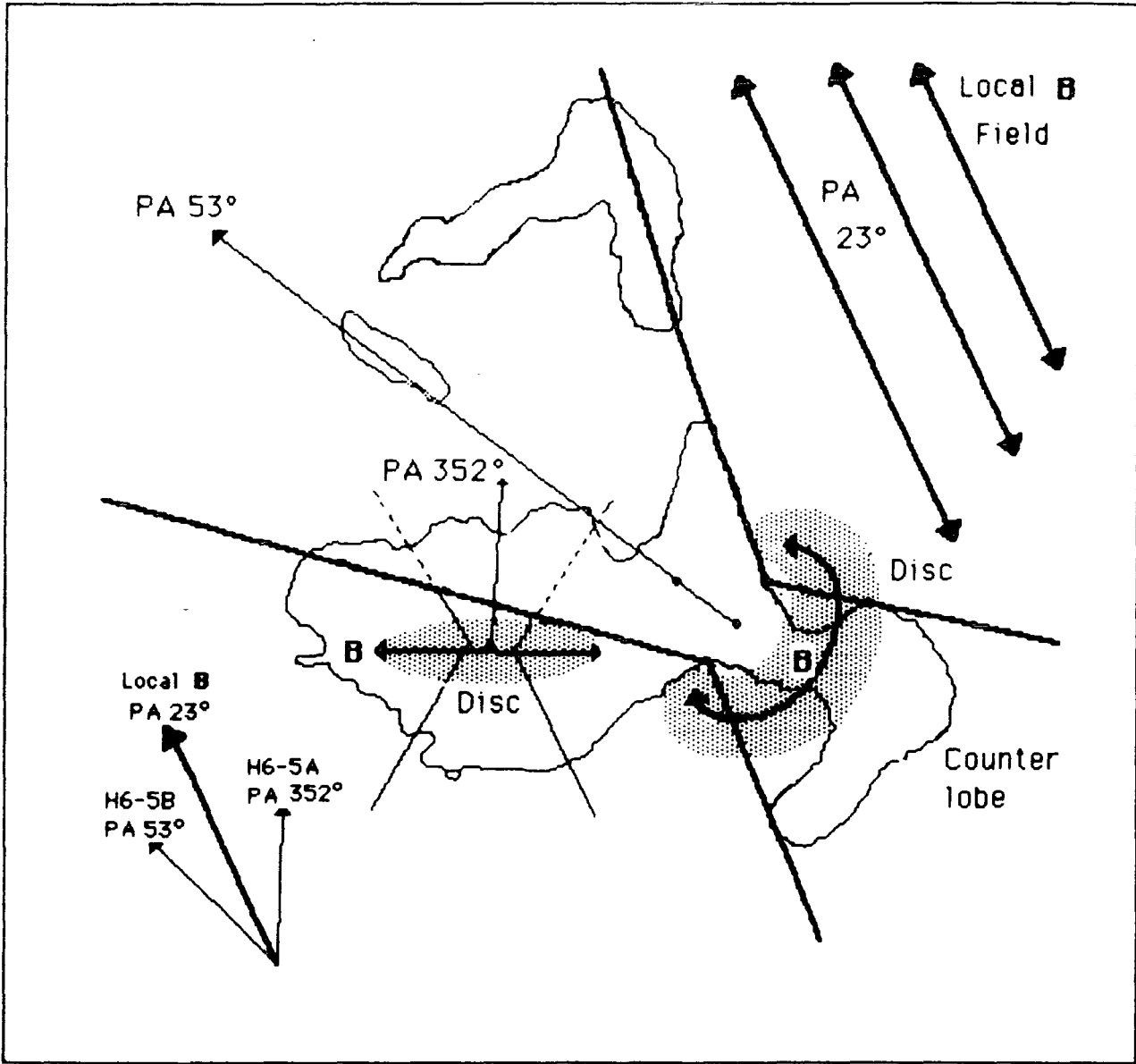Figure 4.8: The proposed geometry for the Haro 6-5 system.
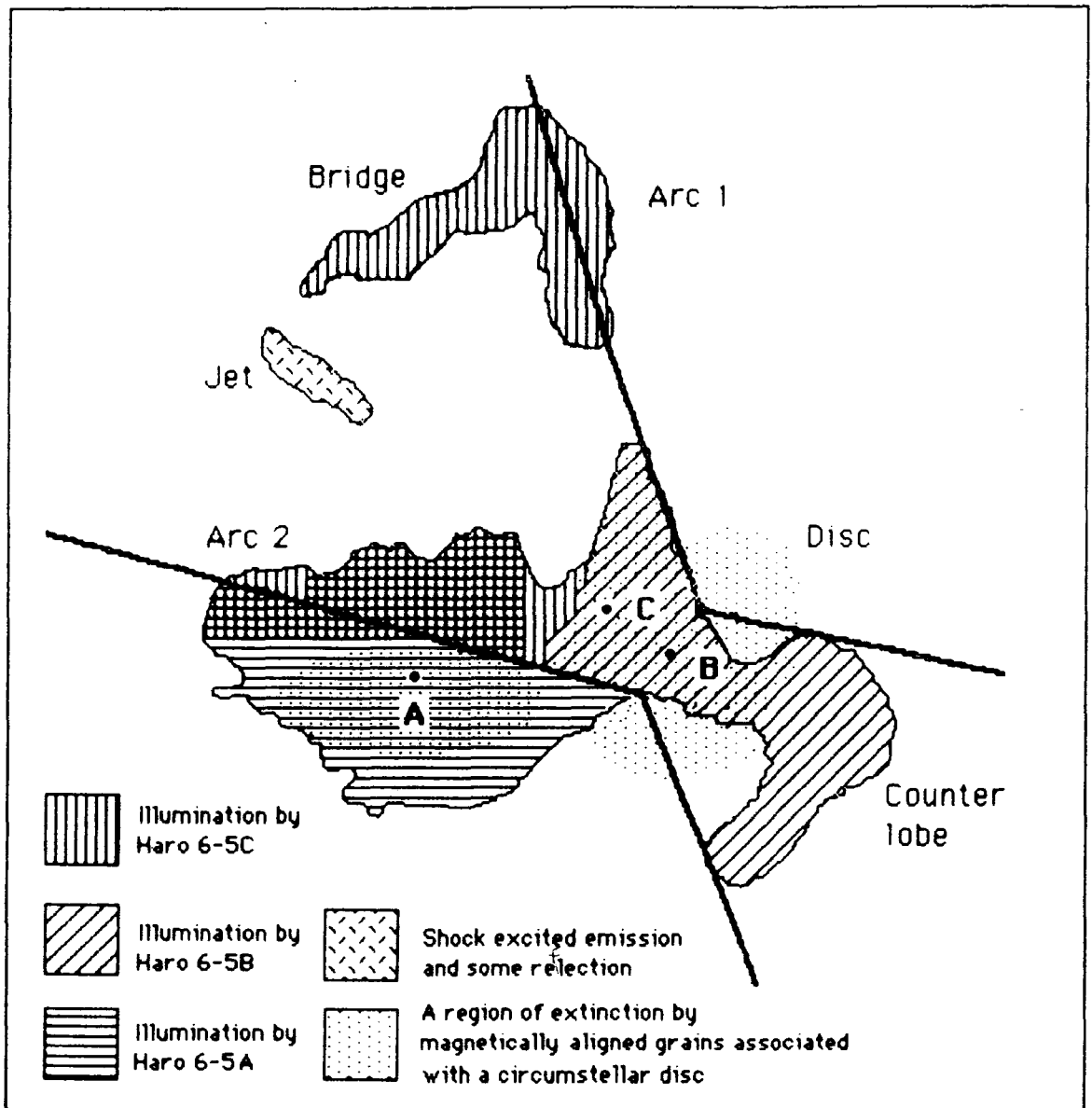
Figure 4.9: The polarising influences in each region of the Haro 6-5 system. The jet region will be discussed shortly in §4.4.

Figure 4.6 (coordinates (-20,-2) and (-16,2) respectively) are also indica-
tive of discrete superimposed nebulosities. Assuming these boundaries, the
opening angle of the Haro 6-5B bicone is approximately 58 deg.

The brightness peak of knot A of the emission line jet lies on the axis of
the Haro 6-5B bicone at PA 53 deg. which is approximately orthogonal to
the equatorial plane of the disc around Haro 6-5B (150 deg—Figure 4.9).
The bicone is inclined to the plane of the sky such that the north-eastern
cone is tilted towards us and the equatorial disc partially overlies and ob-
scures the counterlobe region to the south-west.

In this geometry, Haro 6-5C may be interpreted as a region of intense
scattering from the surface of the bicone or from the surface of the disc
(viewed through the bicone). The 'waist' of the bicone is $\approx$ 8 arcsec in
diameter which, at a distance of 140pc is equivalent to $\sim 10^3$AU. In the
present geometry this dimension is equated with the inner diameter of the
circumstellar disc around Haro 6-5B.

It is tempting to identify the bridge of nebulosity as the outer boundary
of the north-eastern cone. However, the R band image of Mundt *et al.*
(1984) clearly shows that the faint portions of the jet extend well beyond
this point casting doubt on such an interpretation.

4.3.3.2 The Haro 6-5A Bicone

This structure is much less clearly defined than the Haro 6-5B bicone and
the geometry shown in Figure 4.8 is inferred indirectly from the polarisation
data. Both Figure 4.6 and Figure 4.7 show evidence for a conical extension
of contours to the south of Haro 6-5A, but do not show a corresponding
structure to the north. However, it is known that Haro 6-5A contributes to
the illumination of the region to the north from the interpretation of the
polarisation map (§4.3.2). Hence, it is *assumed* that a cone of nebulosity,
similar to the one to the south, extends to the north of Haro 6-5A to form
a bicone centred on this star. The axis of this bicone is at PA 352 deg.,
again approximately orthogonal to the equatorial plane of the obscuring
disc around Haro 6-5A—for which there *is* strong evidence.

It is not clear to what extent, if any, the Haro 6-5A bicone is inclined
to the plane of the sky. It has been shown that there is a component of
extinction to the south of the star indicative of an intrusion of the disc

magnetic field into this region. This suggests that the disc *may* overlie the region to the south of the star to some extent, although in the absence of corresponding information to the north of the star (due to the complex polarisation in this region) this is difficult to corroborate. However, such a nebular tilt would ensure that the northern cone projects out of the plane of the sky and the southern cone into it—an orientation compatible with that of the Haro 6-5B bicone.

4.4   Polarimetry of the Jet Region

In order to assess the degree of coincidence of the total and polarised intensity structures in the jet region more easily, Figure 4.10 shows total and polarised intensity images contoured so that they appear in the same coordinate system (arcsec offset from Haro 6-5B). The data are derived from the R band INT observations and a linear background subtraction has been applied in an attempt to remove the reflection nebulosity in which the jet is embedded. This was done by fitting a planar surface to regions on either side of the jet and extrapolating the surface underneath the jet.

The region of the jet seen in the total intensity image corresponds to the elongated knot A region. As discussed in §4.2.1, the inner knot B region and the fainter extended portions of the jet are not immediately evident in these broad R band observations.

In the total and polarised intensity images of Figure 4.10 the main peak in polarised intensity is located at (-27.5,20) and the peak in total intensity at (-26.5,20.5) in the coordinate system of Figure 4.10. The separation between the two peaks is ≈ 1 arcsec and appears to be real rather than due to any misalignment of the images. Similarly, none of the other polarised intensity knots are coaxial with the jet (as defined by the total intensity image), but appear slightly displaced to one side or the other.

Figure 4.11 shows a montage of polarisation maps superimposed on contoured total and polarised intensity images (the polarisation vectors are derived from the same background-subtracted data as the images in Figure 4.10 and should, therefore, only represent properties intrinsic to the jet).

Part (a) of Figure 4.11 shows polarisation vectors obtained by sampling over 5 pixel (≈ 2.2 arcsec) diameter circular bins spaced at regular intervals
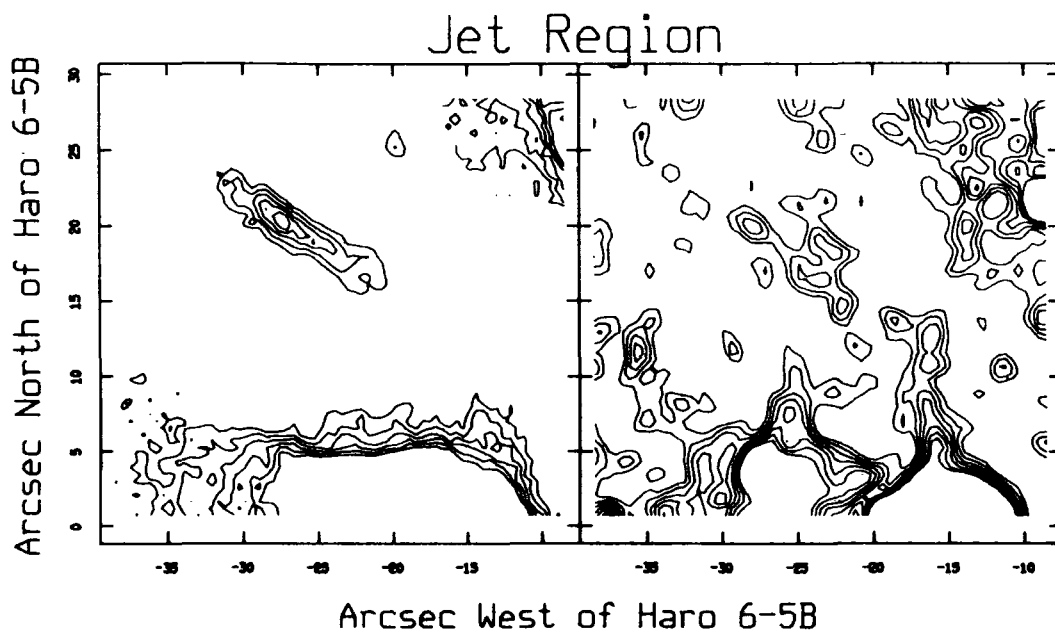
Figure 4.10: Contoured total (left) and polarised (right) intensity images of the knot A region of the jet derived from the INT data and in a coordinate system centred on Haro 6-5B. The contours are linearly spaced.

along the axis of·the jet (PA 53 deg.). The contour spacing is linear. The vectors in the northern portion of the jet appear chaotic due to the lack of polarised intensity in this region. In the central and southern regions, the polarisation levels range from less than 10 to about 20 per cent and PAs lie in the range 136 $\rightarrow$ 161 deg. with a mean value of $\approx$ 148 deg. —approximately perpendicular to the jet axis. Although, individually, the measurements are characterised by large errors, the collective trend in orientations is suggestive of the scattering of light originating from a source of illumination located somewhere along the axis of the jet.

Part (b) of Figure 4.11 shows the polarisation map of (a) superimposed on contours of polarised intensity (spaced as in Figure 4.10). The vectors that deviate markedly from perpendicularity with the jet axis correspond to areas of low polarised intensity.

The polarisation vectors corresponding to the polarised intensity peaks are shown in part (c). The polarised intensity peak closest to the brightness peak of knot A is polarised at 14 ± 8 per cent with PA 150 ± 15 deg. (within a circular aperture of diameter $\approx$ 2.2 arcsec). The individual measurements in this map are characterised by large errors (typically 50 per cent) but the coherence of the vectors suggests that the polarised intensity peaks are not corrupted by cosmic rays or aberrant pixel values.

Part (d) shows polarisation values obtained by integrating over 3 pixel ($\approx$ 1.3 arcsec) diameter circular apertures spaced at regular intervals along the axis of the jet and along two parallel axes running down the edges of the jet. The random nature of the polarisations down the sides of the jet suggests that the background subtraction has been successful and that the vectors on the jet axis *do* represent polarisation intrinsic to the jet.

Since the polarised intensity structure revealed by the INT observations is close to the error levels, some possible sources of error will be considered.

1. The polarised intensity knots in the INT data are due to sporadic events such as the incidence of cosmic rays in the detector. If this is the case, then it is difficult to explain the consistent polarisation angles at the position of these peaks which suggest that the jet does contain a component of scattered light.

2. The polarised intensity structures somehow result from the way in which the background nebulosity has been subtracted. The polarisa-
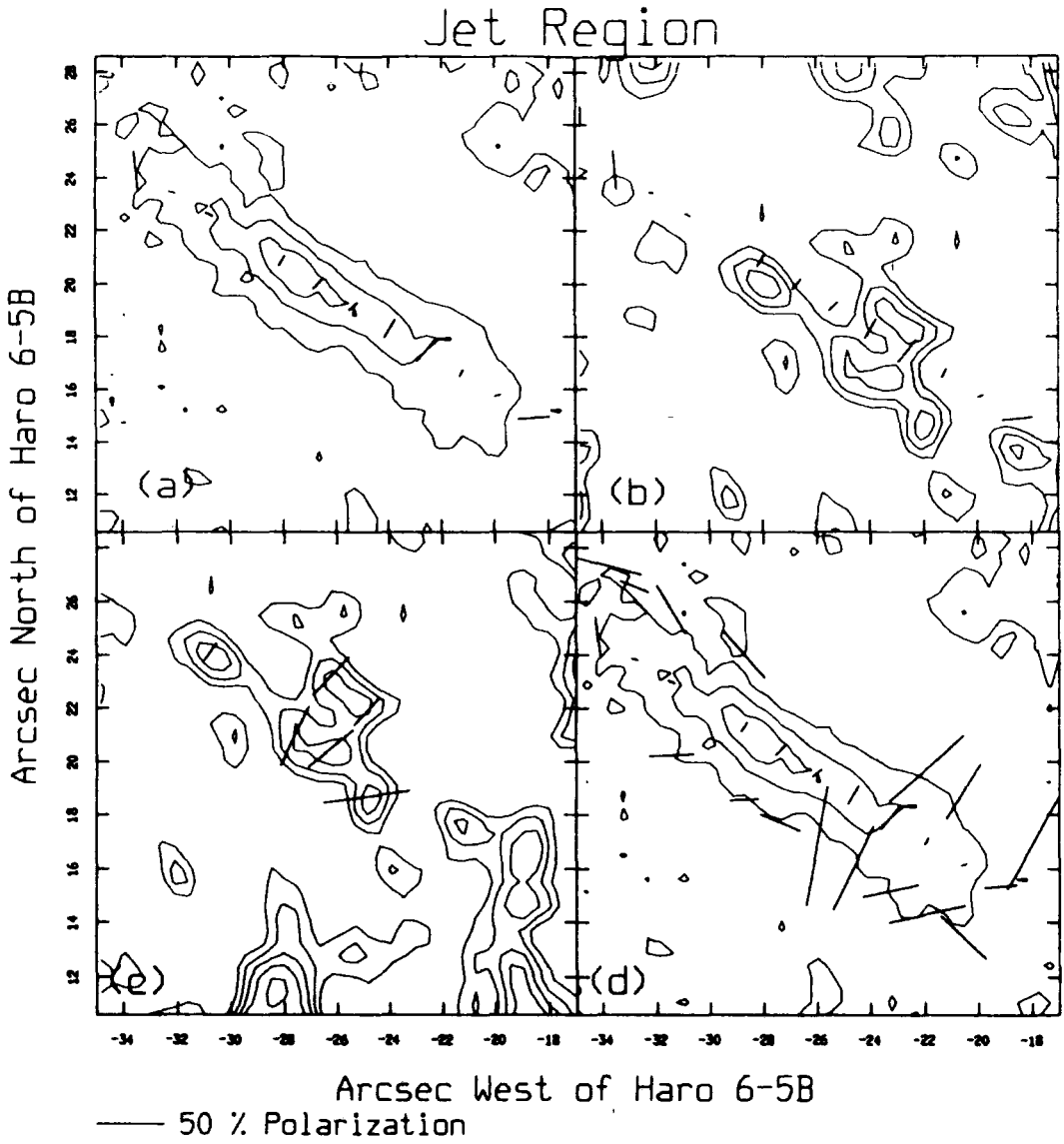
Figure 4.11: A montage of polarisation maps superimposed on contoured total and polarised intensity images as discussed in the text.

tions and position angles at these points might then arise from con-
tamination of the knot A data by remaining background reflection
nebulosity which would naturally form part of the general centrosym-
metric pattern seen elsewhere in the system. However, although this
remains a possibility the polarisation measurements of Figure 4.11
part (d) suggest that any background reflective component has been
removed from around the jet.

3. It does not seem possible to reject any of the data on the grounds of
   spatial coincidence with polarimeter grid edges or chip defects since
   the locations of such potential sources of error are known quite accu-
   rately.

In a previous analysis of the Wise Observatory data, Gledhill *et al.*
(1986) quoted a level of polarisation of 18 ± 2 per cent for knot A on the
basis of transverse profiles through the jet in total and polarised intensity.
In order to verify this measurement an attempt was made to subtract off the
nebulosity in which the jet is embedded. However, due to the small image
scale characterising the Wise Obs. data, it was not possible to uniquely fit
the data in the jet region with a planar surface. Instead, the polarisation
in the knot A region of the jet has been measured by integrating within
an aperture centred on the jet and by then moving this aperture (by ±8
arcsec in a direction perpendicular to the jet axis) so as to sample the
nebular polarisation on either side of the jet. By subtracting the average
normalised Stokes parameters in these two 'sky' regions from those in the
jet region, an estimate of the polarisation intrinsic to the knot A region of
the jet can be obtained. In order to get the best possible signal to noise
ratio, a rectangular aperture (12 by 3.6 arcesec) encompassing the whole
of the knot A region of the jet was used. This proceedure results in a
polarisation level of 20 ± 2 per cent at PA 142 ± 2 degrees intrinsic to the
jet. So as to eliminate the effects of possible cosmic ray events within the
aperture, the data were checked for consistency by using both halves of the
data set separately to obtain independent (apart from flat-fielding errors)
estimates of Q and U.

Applying this process to the INT jet, using apetures of the same physical
size and location, gives a polarisation of 7±3 per cent at PA 150±11 degrees.
Clearly, in order to reconcile this measurement with the Wise Obs. data
it is necessary to assume that the polarisation of the jet is variable. Such

a variability could be produced by changes in emission line strengths or by fluctuations in the brightness of an illuminating source. Gledhill *et al.* (1986) pursued the possibilities of a jet seen by scattered emission light (originating from a source located somewhere along its axis) and found it extremely difficult, in the case of Haro 6-5B, to reconcile such a model with the existing observations.

If the knots in Figure 4.10 do represent the localisation of polarised intensity then this suggests a restricted occurrence of scattering within the jet at the time of the observations. Such a situation may arise if the scattering centres exist in small 'pockets'.

4.5 Discussion

It is interesting to contrast the straight-edged morphology of the Haro 6-5B bicone with that of other optically bipolar systems in which less symmetric geometries are often seen. Many bipolar nebulae exhibit paraboloid geometries which are sometimes regular (*e.g.* LkHα208) or, as is more often the case, distorted to varying degrees (*e.g.* PV Cephei and R Mon). The distorted systems may be characterised by more than one axis of symmetry and in some cases, the symmetry axis appears to rotate in PA with offset from the illuminating source (*e.g.* R Mon: Warren-Smith *et al.* 1987a). However, the Haro 6-5B bicone possesses a single symmetry axis oriented at PA $\approx$ 53 deg. along and about which the nebular features are distributed.

The Haro 6-5B system possesses the main attributes of other regions exhibiting molecular outflow (an extensive disc, evidence for an associated magnetic field and a bipolar nebular geometry) and is inclined at a favourable angle to the plane of the sky for the detection of such an outflow, if present. Molecular outflow is occurring in other regions of the Taurus cloud complex (most notably in the L1551 cloud) which, because of its proximity to Earth, affords an ideal opportunity for the study of this phenomenon. Haro 6-5A must also be viewed as a potential candidate for a molecular outflow since, although the nebular geometry is much less well defined than in the case of Haro 6-5B, there is strong evidence for the association of an obscuring disc and threading magnetic field with this star. However, Heyer *et al.* (1987b) present a molecular line survey of IRAS sources in the Taurus clouds but do not note any peculiar line wing

emission in the vicinity of Haro 6-5.

The Haro 6-5B and Haro 6-5A bicones have been presented as separate nebular complexes, as is indicated by all the available data. The relationship between the two systems is more difficult to ascertain. Two possibilities are:

1. The Haro 6-5A bicone is a background system lying partially behind the foreground nebulosity of the Haro 6-5B bicone.

2. The two systems are at approximately the same distance in which case the dust to the north of Haro 6-5A may be illuminated by both this star and by Haro 6-5C or B.

On intuitive grounds, it does not seem likely that the Haro 6-5A system is the closer of the two since the nebular structure associated with this star is much less well defined and (apparently) smaller in angular extent than that associated with Haro 6-5B. However, it is quite possible that the two systems are at totally different stages of PMS evolution, in which case it would be premature to judge the issue on geometrical grounds alone.

The magnetic field structure in the Taurus complex has been mapped over a large area by Moneti *et al.* (1984) by the measurement of the optical and IR polarisations of background stars and the assumption of DG grain alignment. The resultant polarisation map (figure 1 in their paper) shows a uniform magnetic field oriented approximately perpendicular (on the plane of the sky) to the Galactic plane and the elongated cloud condensations and possessing a smooth variation in PA over a large area. Vrba *et al.* (1985) select 10 stars within 1 deg. of Haro 6-5(A) from the observations of Moneti *et al.* and obtain a mean PA of 23.5±4.1 deg. Assuming DG alignment, this is the mean PA of the large-scale magnetic field in the Haro 6-5 region. The Haro 6-5 system appears to be located within the outline of an elongated cloud (DL-1 oriented with long axis at PA ≈ 140 deg. in figure 1 of Moneti *et al.* 1984). If the Haro 6-5B system *has* formed within this elongated cloud, then it has formed in such a way that the PA of the equatorial plane of the circumstellar disc about Haro 6-5B is now approximately parallel to the PA of the long axis of the cloud.

Mechanisms of cloud collapse were reviewed in §1.3 where it was seen that a cloud threaded by a magnetic field is likely to collapse anisotropically

along the magnetic field lines leading to a highly flattened sheet-like structure. The degree of contraction perpendicular to the field lines depends upon the level of competition between inertial and magnetic forces and on the occurrence of any flux leakage or slippage.

Heyer *et al.* (1987a) present wide-angle CO intensity maps of the B216-B217 region (in which the Haro 6-5 system is assumed to lie) which clearly show a cloud structure elongated with PA $\approx$ 125 deg. Velocity measurements indicate that the cloud is rotating and therefore may be sheet-like, suggesting that the threading magnetic field has had a dominant and controlling influence on the collapse of this structure. This interpretation is strengthened by polarimetric observations of background stars in the B216-B217 region by the same authors. An average polarisation of 28 ± 7 degs. is deduced which, on the assumption of DG alignment, suggests a magnetic field orientation approximately perpendicular to the axis of elongation of the B216 and B217 clouds. In such a situation it is to be expected that further collapse into sub-condensations and, ultimately, circumstellar discs will be controlled by the same magnetic field, leading to the formation of discs lying almost exactly within the plane of the parent cloud-sheet, as seems to have occurred in the Haro 6-5B system.

The location of Haro 6-5A within the Taurus complex and within the above described scheme is not so easy. The PA of the proposed disc about this star (82 deg.) is not parallel to that of the Haro 6-5B disc nor to to the B216-B217 cloud orientation. However, an interesting relationship between the various symmetry axes in the Haro 6-5 system is illustrated in Figure 4.8. It appears that the Haro 6-5A disc and the Haro 6-5B disc are inclined at similar angles to the cloud magnetic field orientation on the plane of the sky as determined by Vrba *et al.* (1985).

Examination of the R waveband CCD images of Mundt *et al.* (1984) clearly shows the emission line jet to be curved. Although the elongated knot A region lies on the Haro 6-5B bicone axis, the inner portions of the jet appear to deviate away so that knot B lies off the axis. A simple backward projection would suggest that the jet originates between Haro 6-5A and Haro 6-5B where no source is presently known. Is it possible that the curved jet results from the superposition of two separate and inclined linear jets? Such a superposition would appear excessively fortuitous and therefore unlikely, also, the smooth curvature of the jet evident from the CCD frames is strongly suggestive of a single coherent structure. In addi-

tion, similar curved jet features, apparently displaced from their proposed sources, are seen elsewhere. The jet in the HL Tau system (to be discussed shortly) is an example.

Magnetic fields and accretion discs are, as in the case of other outflow manifestations, playing an increasing role in the formulation of theoretical models of emission line jets. The observed configurations of emission line jets should not, therefore, be viewed in isolation but within the framework of an integrated outflow generation mechanism. Evidence has been presented in the preceeding sections for the existence in the Haro 6-5 system of a magnetic field configuration concomitant with the model assumptions of Uchida and Shibata. It is expected that, in the regions above and below a circumstellar disc, the topology of the local magnetic field will undergo a transition such that a predominantly polloidal field exists outside the disc and a predominantly toroidal field exists inside it. If the jet is intimately associated with the magnetic field topology then such a transition may be expected to reproduce itself in the observed jet configuration. In other words if the jet is formed by, for example, a column of material being 'squeezed out' from the inner disc regions and constrained to move along the magnetic field lines, then the jet will provide a map of the magnetic field and will consequently appear curved.

Finally, the polarisation level of Haro 6-5A is much greater than that measured by Vrba *et al.* 1985 (3.3 per cent), although the measurements are not directly comparable due to the differences in effective passbands and apertures used. Cohen and Kuhi (1979) quote a visual extinction of two magnitudes to Haro 6-5A, however, the photometry of Vrba *et al.* (1985) yields a value of 5.4 magnitudes on the assumption of an intrinsic V-K colour of 3 magnitudes and normal interstellar reddening. The latter value is more in line with our R band polarisation measurements.

Chapter 5

The HL/XZ Tau System

HL and XZ Tau are a pair of T Tauri stars located in the northern region of the L1551 cloud which itself lies towards the south of the Taurus dark cloud complex. The L1551 cloud is well known for the molecular outflow, optical nebulosity, HH objects and emission line jet associated with the IR source L1551-IRS5. To the north-east of L1551-IRS5 another IR source, L1551 NE, illuminates optical nebulosity (Draper *et al.* 1985b). The HL/XZ Tau system possesses its own emission line jet and shows some evidence for associated high velocity molecular gas. In addition, the two stars appear to be surrounded by morphologically complex optical nebulosity. There is strong evidence, therefore, for (at least) three SF regions in the L1551 cloud suggesting that the phenomenon is relatively common in this area.

5.1   Previous Observations

Mundt and Fried (1983) present CCD imaging of the HL and XZ Tau region through their R band and Hα filters, and report the detection of a jet to the north-east of HL Tau at PA 36 ± 3 deg. They note that, whilst the jet appears to be colinear with fainter and more extensive nebulosity, its axis does not in fact connect with HL Tau but passes $\approx 5 \rightarrow 7$ arcsec to the south-east of this star.

Strom *et al.* (1986) present a velocity survey of the region based on CCD imaging of the [SII] line in which the jet to the north-east of HL Tau appears blue shifted. A corresponding red shifted structure to the south-east of this star is also seen, but is less obviously jet-like.

The long slit·spectroscopic observations of Mundt *et al.* (1987) indicate that the blue shifted heliocentric velocities in both [SII] and Hα emission from the north-eastern jet increase from ≈ $-140 \rightarrow -180$km s^{-1} with distance from HL Tau. The existence of a small patch of red shifted ($+63$km s^{-1}) Hα emission to the south-east of HL Tau (also seen in [SII]) is noted, although, in view of the complexity of the nebulosity surrounding HL and XZ Tau, the relationship, if any, between this patch of emission and the red shifted structure detected by Strom *et al.* (1986) is not clear. A 6cm VLA continuum survey by Brown *et al.* (1985) detects both HL and XZ Tau as well as a third optically invisible source. Mundt *et al.* (1987) suggest that this latter source (designated VLA1-HL Tau at position $\alpha(1950)= 4^h28^m45.2^s$, $\delta(1950)= 18°7'42''$) may be responsible for the emission line jet to the north-west of HL Tau. The existence of this VLA source, however, has not yet been corroborated (Cohen and Jones 1987). On the basis of their velocity measurements, Mundt *et al.* (1987) declare the existence of a bipolar flow in the region, probably centred on the VLA source VLA1-HL Tau.

Calvet *et al.* (1983) detect broadened CO line profiles in the region and deduce the presence of high velocity molecular gas. Both red and blue shifted gas is detected, although the red shifted component may be contaminated in part by the extensive molecular outflow associated with L1551-IRS5 further to the south. Higher resolution (30 arcsec) CO mapping by Torrelles *et al.* (1987) also reveals the presence of both red and blue shifted gas in the vicinity of HL and XZ Tau. On a geometrical basis these authors find it unlikely that HL Tau is responsible for the high velocity gas since both red and blue shifted components lie closer to XZ Tau on the plane of the sky.

The spectral energy distribution of HL Tau, extended into the far-IR by the observations of Cohen (1983), suggests that the radiation from this star is dominated by long wavelength (up to 100μm) emission. The unusually large ratio of IR to optical luminosity (630) leads Cohen to suggest that HL Tau is seen through an edge-on circumstellar disc. A bolometric luminosity of 7.2L$_\odot$ and visual extinction of 7 magnitudes are derived for HL Tau. It is suggested that the HL Tau system may be at a very early stage of PMS evolution, possibly as young as 10^5 years, in which case the star may be surrounded by a loosely bound assembly of warm IR-emitting material rather than a compact disc.

A circumstellar disc is also indicated by the near-IR speckle interfero-
metric observations of Beckwith *et al.* (1984) which reveal a region of ex-
tended scattered light around HL Tau of dimensions 320 by 200 AU (roughly
consistent with the estimates of Cohen 1983). These authors interpret the
light as reflection from a 'fat' circumstellar disc, probably inclined to the
plane of the sky.

Beckwith and Sargent (1987) present interferometric ^{13}CO observations
of HL Tau and conclude that the star is surrounded by an elongated con-
densation of gas which they identify with a disc oriented with equatorial
plane at PA 147 deg.

5.2 New Observations

Polarimetric data on the HL and XZ Tau region were obtained at the 2.5m
Isaac Newton telescope (INT) of the La Palma Observatory on 1987 Jan
4th. The Durham CCD imaging polarimeter system (described in §3.2) was
used at the f/15 Cassegrain focus and a total of 20 unfiltered exposures were
made. In each of these exposures the object was imaged simultaneously
in orthogonal polarisation states.The length of exposure varies between
CCD frames so that, upon subsequent recombination and normalisation,
information is available in both the faint nebular and bright stellar regions.
The data is unfiltered giving a broad bandpass of about 450nm to 1000nm
with peak response around 720nm (Table 3.1).

The image scale is ≈ 0.43 arcsec pixel^{-1}. A linear rather than constant
sky subtraction is used in order to guard against possible contamination
of the exposures by dome-originating scattered light, otherwise the data
reduction is as outlined in §3.2.

5.2.1 Imaging

Figure 5.1 shows a contoured total intensity image of the HL and XZ Tau
region obtained from a combination of 16 of the 20 unfiltered CCD frames.
The image has been smoothed by the application of a 3 pixel^2 filter. The
centroids of the three stars HL Tau, XZ Tau and LkHα358 are indicated
by '+' and are labelled. HL Tau lies at the centre of the coordinate sys-
tem. The approximate location of the VLA1-HL Tau source, obtained by

offsetting its coordinates (taken from Mundt *et al.* 1987) from those of XZ and HL Tau (from Strom *et al.* 1986) is shown by '*' (at (-9,7) in the arcsec coordinate system centred on HL Tau). The image of XZ Tau is badly charge smeared in these exposures and so the affected pixels have been removed to leave the blank region in the centre and to the south of XZ Tau. The XZ Tau centroid shown has been obtained from a separate series of short exposure (50 sec. each) CCD frames. These frames will also enable measurement of the polarisation of XZ Tau, however, they have been excluded from the composite image shown contoured in Figure 5.1 since they contribute only noise to the majority of the nebulosity. The 'spurs' to the immediate east and west of XZ Tau result from diffraction of the stellar image.

The dominant luminosity peaks, corresponding to the stars HL and XZ Tau, are separated by ≈ 24 arcsec on the plane of the sky. The image of XZ Tau, although surrounded by faint nebulosity, is stellar in appearance (ignoring the diffraction and charge smearing effects) whereas that of HL Tau is clearly not. The latter star is surrounded by contours which are extended and irregular suggesting that HL Tau is embedded within optically bright nebulosity. The PA of elongation of the contours surrounding HL Tau is roughly 145 deg. LkHα358 also has the appearance of a nebulous star, in this case the nebulosity is elongated in an east-west direction.

To the north-east of HL Tau lies the blue shifted emission line jet first reported by Mundt and Fried (1983). In the present unfiltered data the jet consists of three knots, labelled A, B and C, which together form a structure ≈ 18 arcsec in length. It is not possible to draw a straight line through all three of the knots shown in Figure 5.1, suggesting the existence of an element of curvature in this structure. An axis at PA 40 deg. passes through knots A and B whereas the outer knot C appears displaced slightly to the north of this line. The effect, however, is rather subtle, and the deviation from linearity over the length of the detected jet is small. In any case it is not possible to cause an axis through any two of the knots to intersect with HL Tau or any other optically visible source. A simple backward projection of the jet passes about 5 arcsec to the south-east of HL Tau. The VLA source, suggested by Mundt *et al.* (1987) as an exciting source for the jet, is located at the south-western tip of the jet (as indicated by the '*' in Figure 5.1) and lies close to the axis at PA 40 deg.

The bright features of Figure 5.1 appear to be superimposed upon a

background of extensive and, in places, highly structured nebulosity. The fainter nebulosity appears quite amorphous and seems to be distributed fairly evenly about HL Tau in a broad swathe running from the tip of the jet in the north-east to LkHα358 in the south-west. The brighter nebulosity is more organised and structures can be discerned extending from spurs on the inner contours surrounding HL Tau to form a system of multi-directional arcs. Several possible arcs are indicated by curves in Figure 5.1. The regions between the arcs are occupied by fainter, connective nebulosity. To the north-east of XZ Tau a linear structure measuring $\approx$ 11 arcsec in length is visible. Faint nebulosity extends to the east of XZ Tau in an arm-like extension terminating in a brighter globule. Two outlying patches of nebulosity can be seen to the north-east and to the north of XZ Tau. One of these patches appears globular, the other irregular, both seem to be detached from the main body of nebulosity and the irregular patch is approximately colinear with the jet.

The luminous structure in the HL/XZ Tau region is clearly complex and, on the basis of morphology alone, it is difficult to decide what roles, if any, each of the hitherto detected sources play in the generation and maintenance of the observed nebulosity.

5.2.2 Polarisation Mapping

Figure 5.2 shows a linear polarisation map of the HL/XZ Tau region derived from the unfiltered INT observations. Each vector represents an integration over a 7 pixel ($\approx$ 3 arcsec) square bin, the inter-bin spacing being 5 pixels ($\approx$ 2.2 arcsec). Selected brightness contours are plotted to indicate the extent of the faint nebulosity and the relative locations of the optically bright sources are shown by '+' (as in Figure 5.1). Also, a total intensity cut is imposed on the map so that no vectors are plotted outside the lowest brightness contour.

Large levels of polarisation are evident throughout the great majority of the HL/XZ Tau system suggesting that the nebulosity is seen primarily by reflection. In the regions to the north-east of HL Tau, polarisations reach 50 per cent in places with 30 $\rightarrow$ 40 per cent being typical whereas lower values of 20 per cent are representative in the regions to the south and south-west of the star. To the south-east and north-west of HL Tau polarisation levels are lower still, generally 10 $\rightarrow$ 20 per cent. In addition
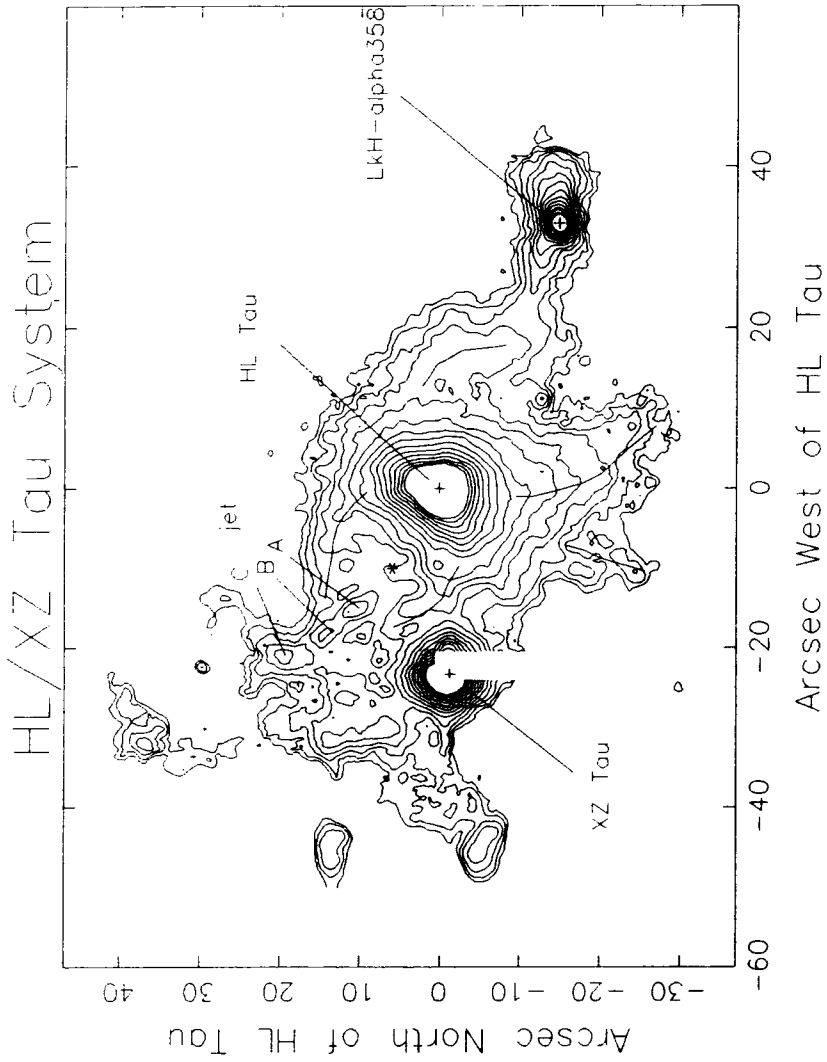
Figure 5.1: A contoured brightness map of the HL/XZ Tau system, as discussed in the text.

there are regions within the lowest brightness contour where the polarisation becomes extremely low or disappears entirely. In agreement with previous observations, HL Tau itself appears considerably polarised. The central regions of XZ Tau have been removed due to the effects of charge smearing and so the polarisation of this star will be obtained from the four short exposures not used in Figure 5.1.

Although the levels of polarisation vary considerably throughout the nebular complex, the pattern formed by the vectors is more coherent. Ignoring, for the moment, the nebulosity in the region of XZ Tau and LkHα358, the majority of the polarisation map displays vector orientations symptomatic of illumination from the vicinity of HL Tau. However, instead of the circular arrangement of vectors seen in the case of isotropic illumination by a single unpolarised central point source, local perturbations in vector orientation appear to be superimposed on a general elliptical pattern centred on HL Tau. The major axis of the ellipse appears to be inclined at approximately the same position angle as the axis of elongation of the contours immediately surrounding HL Tau, which in turn is parallel to the angle of polarisation of the star itself. Returning now to the outlying nebulosities, a transition region is evident in the polarisation pattern to the south-west of HL Tau. Beyond this region, to the west, the prevailing source of illumination is LkHα358 as evidenced by the symmetric distribution of vector orientations to the east and west of this star. Again, a precise circular vector arrangement is not seen although in this case the residual curvature in the pattern is sufficient to identify LkHα358 as the dominant influence. A casual inspection of the polarisation data suggests, therefore, that there may be two separate reflection nebulae in this area—one associated with HL Tau and one with LkHα358.

The polarisations of the three stars HL Tau, XZ Tau and LkHα358 have been measured using a circular aperture centred on each star. The results of this simulated aperture polarimetry are given in Table 5.1. The measurements of Vrba *et al.* (1976) and Bastien (1982) are shown in Table 5.2. When making comparisons between these tables it is relevant to note that the results of aperture polarimetry are dependent upon the size of the aperture used, especially when the object is embedded within strongly polarised reflection nebulosity—as in the case of HL Tau. Under these circumstances it is advantageous to be able to fit the aperture to the stellar image after the observations (when the average seeing conditions are known) such that
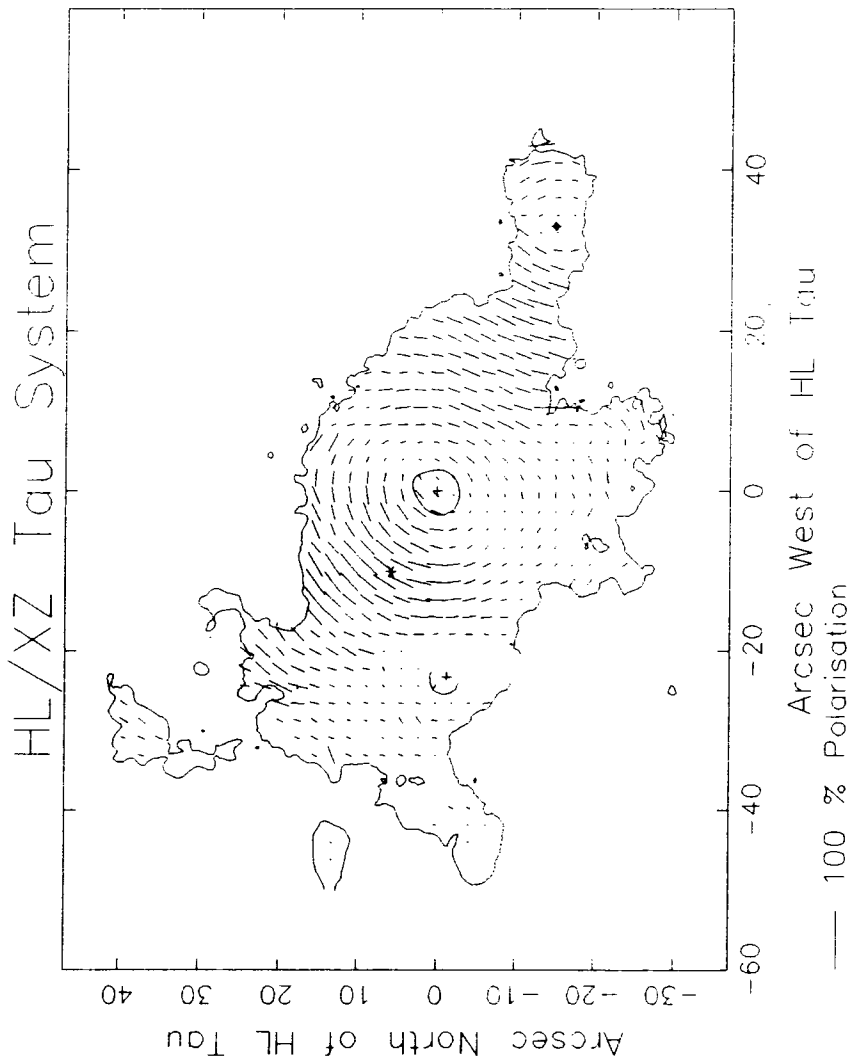
Figure 5.2: Polarisation map of the HL/XZ Tau region derived from the unfiltered INT data and discussed in the text.

Source	INT data	
	P (%)	PA (deg.)
XZ Tau	1.7 ± 0.3	87 ± 5
HL Tau	15.2 ± 0.3	143 ± 0.5
LkHα358	4.1 ± 0.3	4.2 ± 2

Table 5.1: Polarisation measurements for the three stars, derived from the unfiltered (peak response 720nm) INT data. In each case, a circular aperture of diameter 5 pixels ($\approx$ 2.2 arcsec) was used.

Source	Vrba		Bastien	
	P (%)	PA (deg.)	P (%)	PA (deg.)
XZ Tau	1.4 ± 0.3	93 ± 5	0.9 ± 0.2"	100 ± 5
HL Tau	12.3 ± 0.6	144 ± 1	11.2 ± 0.2	147 ± 1

Table 5.2: Polarisation measurements for the three stars taken from Vrba *et al.* 1976 and Bastien 1982. The measurements from Bastien 1982 are for an aperture size of 14 arcsec and correspond to a peak wavelength of 754nm.

it contains as much of the direct starlight as possible (a significant proportion of the polarisation may reside in the wings of the stellar profile) but is not contaminated by the surrounding nebulosity. In this case, a 5 pixel ($\approx$ 2.2 arcsec) diameter aperture is used. The difference in wavebands used will also affect the comparison of results.

Vrba *et al.* (1976) list the polarisations of 23 stars lying toward the L1551 cloud. An estimate of the orientation of the magnetic field threading this cloud can be obtained by averaging the results of Vrba *et al.* for stars which are clearly peripheral to the cloud (and therefore more likely to be field stars) and have polarisations greater than or equal to that expected for a star at the distance of the Taurus clouds and by assuming that nearly all of the polarisation takes place within the clouds. A PA of 75 deg. is obtained for the field along with a polarisation of 1.8 per cent which is assumed to be intrinsic to the Taurus cloud material in the L1551 direction. The location of HL Tau, XZ Tau and LkHα358 relative to the near and

far sides of L1551 (and, indeed, relative to one another) remains unknown
and so it would be inappropriate to 'correct' the figures of Table 5.1 for the
polarising effects of the L1551 cloud. However, it is worth noting that if 1.8
per cent at PA 75 deg. is subtracted from the polarisation of HL Tau shown
in Table 5.1 than a figure of 16.6 ± 0.4 per cent at PA 146 ± 3 results. The
polarisation angle of HL Tau in the IR is also 146 deg. (Hodapp 1984) in
excellent agreement with the PA of the molecular disc (147 deg.) reported
by Beckwith and Sargent (1987).

5.2.2.1 The HL Tau Region

A higher spatial resolution polarisation map of the region surrounding HL
Tau is shown in Figure 5.3. The position of the VLA source is marked. The
integration bin size for the polarisation measurements is 5 pixels ($\approx$ 2.2
arcsec) square with an inter-bin spacing of 3 pixels ($\approx$ 1.3 arcsec).

The finer detail afforded by the closer bin spacing in this map empha-
sises the deviations from circular centrosymmetry previously inferred from
the inspection of Figure 5.2. Most conspicuous is the polarisation of HL
Tau itself which, apart from being unusually large (Table 5.1), lies within
an elliptical arrangement of vectors running across the star with major axis
in a north-west south-east direction. The polarisation levels decrease with
distance from the star along this direction with evidence for null points in
the polarisation pattern at about 5 arcsec on either side of the HL Tau
centroid. Analogous polarisation structures have been found in connec-
tion with the stars Haro 6-5A and Haro 6-5B, also in the Taurus complex,
and a model involving magnetised discs of obscuration around these stars
(chapters four and seven) has been suggested.

Taking a broader view, the regions most consistent with a circular cen-
trosymmetric vector pattern centred on HL Tau are contained within the
north-eastern quadrant of the polarisation map. This quadrant also con-
tains the highest levels of polarisation as well as the jet and VLA source
(Mundt *et al.* 1987). Even so, local perturbations in vector orientation
are still quite evident in this north-eastern quadrant of the map. A closer
examination of the vector pattern surrounding this star will be given in
§5.3.

Centrosymmetry is less obvious in the regions to the west and south-

west of HL Tau and in many cases the vectors have orientations similar to those overlying HL Tau—although the residual curvature indicative of a scattering pattern associated with this star is still evident. The polarisation levels here are also slightly lower than those to the north-east of HL Tau. Again, an analogous effect is observed in the Haro 6-5 system in the triangular nebulosity to the north-east of Haro 6-5B and, to a lesser extent, in the nebulosity to the south of Haro 6-5A.

The north-west south-east line running through HL Tau (and defined by the polarisation angle of the star) appears to divide the map into two manifestly different parts. To the south and west of this line the vector orientations are approximately elliptical suggesting a source of illumination to the north-east of HL Tau (assuming simple scattering) whereas to the north-east circularity is more evident in the vector pattern. In addition, the polarisation levels along this supposed dividing line are markedly lower than those typical elsewhere in the map. In the south-western extremity of Figure 5.3 the effects of illumination from LkHα358 begin to become apparent.

5.2.2.2 The LkHα358 Region

A polarisation map centred on LkHα358 is shown in Figure 5.4 and has the same integration bin size and spacing as that of Figure 5.3—in fact, the two fields overlap slightly. In this overlap region the effects of illumination from both sources (HL Tau and LkHα358) can be seen, resulting in an 'S' shaped vector pattern. To the north the scattering of light from HL Tau seems to dominate whereas to the south, the influence of LkHα358 is more apparent. However, it is difficult to determine the exact extent of the influence of these two sources in this region. As mentioned previously, the curvature evident in the vector pattern surrounding LkHα358 identifies this star as the predominant illuminator of the arm-like extension of nebulosity in which it resides. The curvature does not extend to circularity though, and the pattern appears to be 'flattened' along a north-south line. This is interesting in view of the angle of polarisation measured for the star which is also approximately north-south. If a component of the polarisation overlying LkHα358 also affects the reflected light from the surrounding nebulosity then the modified scattering pattern may be expected to resem-
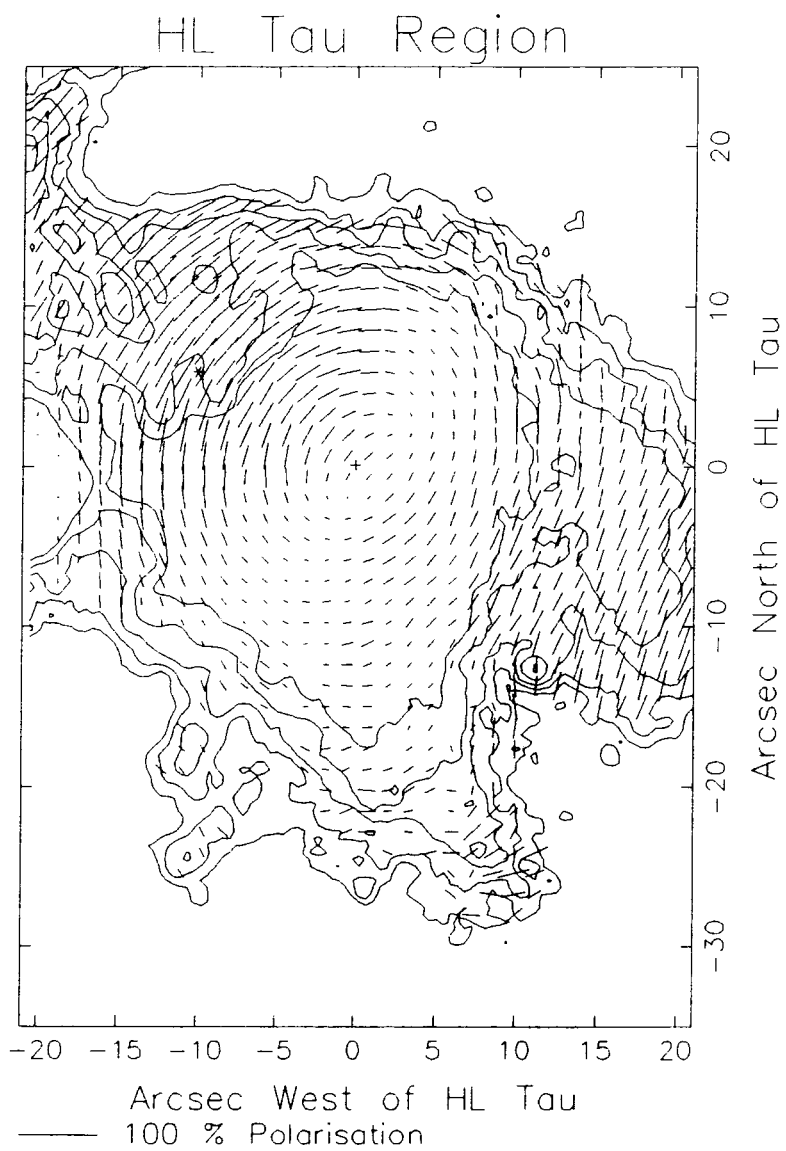
Figure 5.3: A higher spatial resolution polarisation map of the region surrounding the star HL Tau.

ble the flattened vector orientations actually observed. The polarisation pattern in the vicinity of HL Tau shows a similar flattening of the vector orientations along a line parallel to the polarisation of this star.

5.2.2.3 The XZ Tau Region

A polarisation map of the XZ Tau region is shown in Figure 5.5 with integration bin size and spacing identical to that of Figures 5.3 and 5.4. A polarised intensity cut has been imposed on this map so that vectors corresponding to nebulosity thought to be too faint for a reliable determination of the polarised quantities are not plotted. Also, a cut in total intensity ensures that no vectors are plotted outside the lowest brightness contour. The position of XZ Tau is marked (at (-24,-1.5) in the arcsec coordinate system centred on HL Tau) and the VLA source is also shown to the north-west of this star.

The strong scattering pattern in the western and northern part of the map is that associated with HL Tau. The influence of the HL Tau scattering pattern is identifiably bounded but without any evidence of the continuity in polarisation level and angle seen in the transition between scattering patterns in the LkHα358 region. Instead, the polarisation levels and angles seen in the central and western regions of Figure 5.5 appear comparatively disorganised and, in many places, non-existent suggesting that no additional source of illumination is present here. However, to the north and east of XZ Tau, it is still possible to identify groups of vectors whose orientations are consistent with illumination from the direction of HL Tau indicating that light from this star does get through in places to create the effect of 'islands' of reflection nebulosity. These 'islands' are separated by regions devoid of vectors where no polarisation above the intensity cuts is detected. However, the nebulosity surrounding XZ Tau is faint (a comparison of the map with the composite image of Figure 5.1 may be helpful although it is relevant to note that the 3 separate fields have been normalised to one another) and in addition, the region was mapped using shorter exposure times so that the results presented here do not preclude the future establishment of polarisation by a deeper imaging survey.

With this reservation in mind, there is no evidence in Figure 5.5 to suggest that XZ Tau illuminates any of the surrounding nebulosity. The possi-
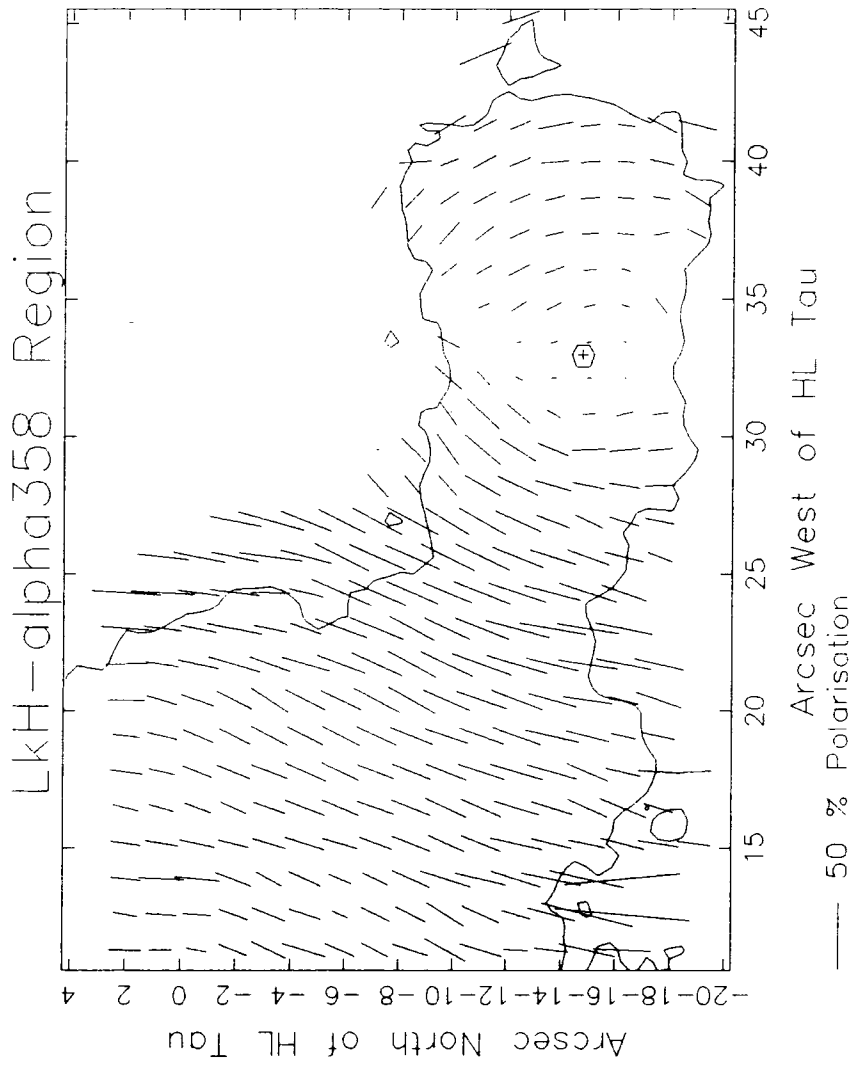
Figure 5.4: A higher spatial resolution polarisation map of the region surrounding the star LkHα358.

bility of a physical association between XZ Tau and some of the surrounding nebulosity still exists, however, since the polarisation data in themselves are not instructive in the interpretation of features that are intrinsically unpolarised. For example, the linear feature (at PA≈ 10 deg.) to the north-east of XZ Tau does not register in the polarisation pattern suggesting that it is seen by emitted rather than reflected light. However, the exposure level is such that a polarisation of less than 5 per cent in this region would be undetected. The PA of the linear feature and its proximity to XZ Tau would favour this star as the progenitor and such a conclusion cannot be excluded on the basis of the polarisation data (although it may be argued that the virtually global influence of HL Tau indicated by the polarisation pattern elsewhere is a reason for the association of all nebular features, polarised or not, with HL Tau). In addition, no polarisation is measured for the globular nebulosities at the eastern edge of the field (as shown in Figure 5.1) although, again, a polarisation level of less than $5 \rightarrow 10$ per cent would not be detected in these observations. However, in view of their compact semi-stellar appearance, these nebulosities may be good candidates for HH objects.

5.3 Interpretation and Discussion

Before proceeding to an interpretation of the data, the salient points presented so far are briefly summarised.

- HL Tau is the most important illuminator in the HL/XZ Tau system and is responsible for the majority of the observed reflection nebulosity. The star LkHα358 also supports reflection nebulosity, although the scattering of light from this star appears to be a locally restricted phenomenon. There is no evidence to suggest that XZ Tau is responsible for the illumination of any of the nebulosity in the HL/XZ Tau region. The role of the VLA source is not clear. Although it is located close to the axis of the emission line jet of Mundt and Fried (1983) and has been suggested as the exciting source of this structure, its position in relation to the remainder of the nebulosity appears arbitrary.

- All three stars are polarised beyond the levels expected for normal interstellar extinction at the distance of the Taurus cloud complex.
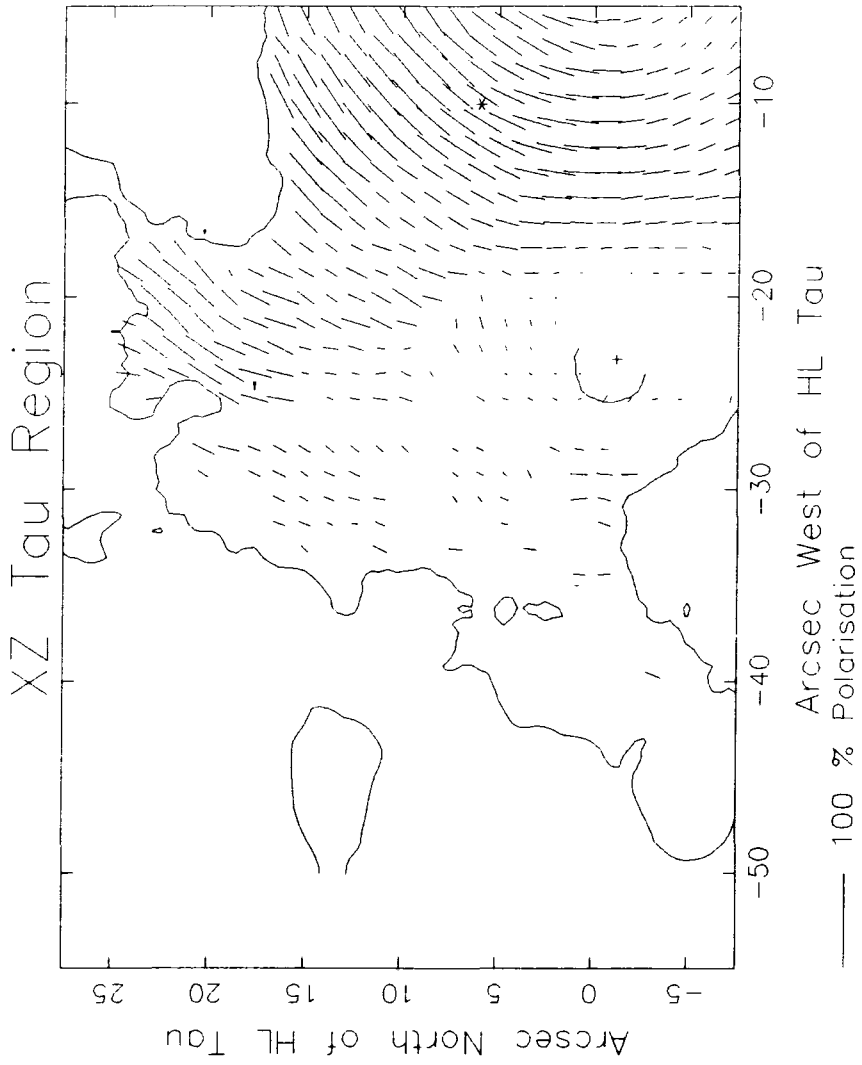
Figure 5.5: A polarisation map of the XZ Tau region as discussed in the text.

The excess polarisation of XZ Tau is small however, and its polarisation is very similar to those of field stars located on the periphery of the L1551 cloud. In contrast, the polarisation level of HL Tau is very large. LkHα358 is polarised to an intermediate extent.

5.3.1 Evidence of a Disc and Outflow Nature for HL Tau

The polarisation pattern surrounding HL Tau, shown in Figure 5.3, provides several clues for the interpretation of this nebulous region and for the formulation of a model consistent with current ideas on PMS stellar evolution. The polarisation of HL Tau itself, 15.2 ± 0.3 per cent at PA 143 ± 0.5 deg. (Table 5.1), whilst being unprecedentedly large is also angled similarly to the group of vectors closely surrounding the star.

It must be explained why regions closely surrounding HL Tau both along the axis of the proposed circumstellar disc and perpendicular to it, show polarisation angles similar to the polarisation angle detected for the star. The observed elliptical distribution of vector orientations and the evidence for null points in the polarisation pattern close to the star cannot be explained in terms of single scattering alone. Instead, an additional polarising mechanism, capable of acting in an antagonistic fashion so as to produce null points, must be invoked. The deviation from circular centrosymmetry of the polarisation pattern is suggestive of the intrusion of a component of the polarisation overlying the central star into the surrounding regions—that is, the pattern appears flattened as if by the superposition of a constant angle polarisation.

Such a polarising mechanism can be accommodated within the context of a magnetic disc of obscuration which, in compliance with the available data, is posited to exist around the star HL Tau. The extinction of light passing through the disc by magnetically aligned dust grains provides the additional source of polarisation, the PA being determined by the orientation of the magnetic field. It is assumed that the geometry of this magnetic field is predominantly toroidal with respect to the disc axis (that is, the field lines lie mostly within the plane of the disc) as seems plausible from simple dynamical considerations of disc systems with significant angular momentum (§2.4.7.1 and §7.4). The extra assumption of DG alignment leads to the proposal of a disc and magnetic field oriented at PA 143 deg.

parallel to the polarisation of HL Tau. The way in which the two polari-
sation patterns (scattering and extinction) may be expected to combine to
produced the features discussed above was detailed in connection with the
Haro 6-5 system in §4.3.3.1 and will also be discussed in chapter 7.

Alternatively, the polarisation of HL Tau and the elliptical distortion
of the surrounding scattering pattern may result if the light leaving the
immediate vicinfiy of the star is intrinsically polarised (Notni 1985). In
this case it would not be necessary to invoke the effects of magnetically
aligned grains.

Further information may be obtained from the map of Figure 5.3. It has
already been mentioned that the polarisation vectors just to the north-east
of HL Tau show a greater element of curvature than their counterparts to
the south-west. Similarly, and moving out from the star, the vector ori-
entations in the north-eastern quadrant of the map appear predominantly
circular whereas those in the south-western quadrant retain a more ellip-
tical distribution. This effect can also be seen in Figure 5.6 which shows
the polarisations plotted radially with respect to HL Tau rather than in a
square matrix.

An explanation may be provided within the context of the aligned grain
model mentioned above if the polarising influence of the disc is more potent
to the south-west of HL Tau than to the north-east. Such a situation may
occur if the disc overlies to a greater extent the former region. To achieve
this the disc may either be more extensive to the south-west or, more likely,
it is tilted out of the plane of the sky. Such a nebular tilt would ensure that
the disc polar axis points out of the sky towards us to the north-east of HL
Tau and into the sky away from us to the south-west. It is interesting to
note that the emission line jet to the north-east of HL Tau is blue shifted
(Mundt *et al.* 1987).

Alternatively, if an intrinsically polarised source is to be prefered, the
range of scattering angles available in the nebular medium must differ be-
tween the north-east and south-west quadrants. An elliptical distribution
of vector orientations may also result if the nebulosity is partially illumi-
nated by light from the extended bright disc in addition to the central point
source of HL Tau.

The enhanced levels of polarisation in the north-eastern and south-
western quadrants of the polarisation map of Figure 5.3 would normally
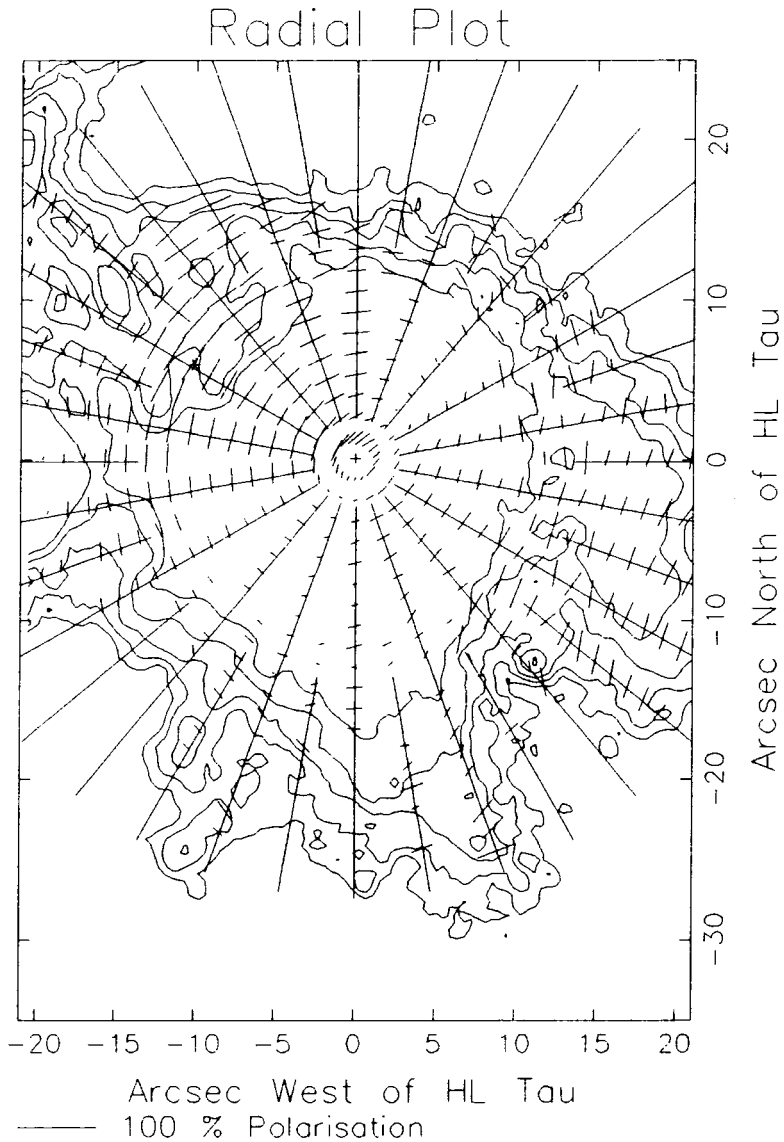signify the presence of two cones of illumination above and below the plane

Figure 5.6: Linear polarisation in the HL Tau region. An integration bin size of 3 pixels ($\approx$ 1.3 arcsec) diameter is used and the bins are spaced regularly at intervals of 3 pixels along lines radiating from the position of HL Tau. Deviations from circular centrosymmetry are apparent by the non-perpendicularity of the vector with the radial line.

of the circumstellar disc posited to exist about HL Tau. However, inspection of Figure 5.1 reveals that such an interpretation is not immediately endorsed by the total intensity data which instead show a general elongation of the brightness contours surrounding HL Tau in a north-west south-east direction—the orientation of the proposed circumstellar disc. Until now, the parallels between the HL/XZ Tau region and the Haro 6-5 system (discussed in the previous chapter) have been notable, however an important difference arises here. The disc around HL Tau is an optically bright structure with more light reaching us through its equatorial regions than through its polar regions. On the contrary, the disc around Haro 6-5B is a dark structure which restricts the illumination of the surrounding nebulosities to a bicone centred on its polar axis. In the case of HL Tau, the polarisation map shows that the most favourable scattering geometries are located in the regions above and below the plane of the circumstellar disc—a situation typical of bipolar reflection nebulae—even though these areas are fainter than the disc regions. The apparent reverse in the *luminosity* structure typical of bipolar reflection nebulae (dark disc, bright nebula) may be explained if the system is particularly youthful, as has been suggested previously (§5.1). In one possible early evolutionary scenario, a loosely bound 'proto-disc' may be sufficiently rarefied to reflect a significant proportion of the light incident upon it into the observer's line of sight, thus appearing as a bright elongated structure. The faintness of the nebulosity above and below the plane of the disc may be due to a paucity of dust in these regions. If the dust in the lobes of bipolar reflection nebulae originates in the disc and is maintained, perhaps, by the disc outflow mechanisms thought to be responsible for, among other things, molecular outflow, then the regions above and below the plane of the disc around HL Tau may be expected to brighten with time. It is therefore proposed that the differences in appearance between the HL Tau and Haro 6-5B systems are due mainly to the two systems being at different stages of PMS evolution. In addition, on the basis of morphological similarity, Haro 6-5A and HL Tau may be at comparable evolutionary stages. An extension of this discussion appears in §5.4

The decrease in polarisation levels in the equatorial disc regions is probably due to a combination of less favourable scattering geometry, competition between polarisation by scattering and polarisation due to extinction by aligned grains and possibly also an element of de-polarisation due to mul-

tiple scattering caused by the higher optical depth for a light path through the plane of the disc.

As well as illustrating the elongation of the central brightness contours along the plane of the proposed circumstellar disc, Figure 5.1 also shows a series of spurs projecting out from these central contours and extending like horns into the faint nebulosity. Four main horns are seen, one at each 'corner' of the disc and, in the light of the preceeding discussion, it is tempting to identify these structures as the first indications of the walls of a bipolar cavity still under construction. Further evidence for this interpretation is provided by the polarised intensity image shown contoured in Figure 5.7. Two disc 'horns' are clearly visible, one to the east of HL Tau and one to the north, indicating that these structures are bright in reflected light as would be expected of the walls of a bipolar cavity. However, because varying exposure times were used in order to limit the effects of charge smearing during observations, the composite image of Figure 5.7 contains one field that is under exposed relative to the remainder leading to the three vertical strips of noisy data. Unfortunately, the region to the west of HL Tau coincides with one of these noisy fields so that the detection of the two horns on this side of the disc in polarised intensity is not clear.

Also visible in Figure 5.7 is the pronounced pinching of polarised intensity contours on either side of the star HL Tau to form the waist-like structure indicative of the lower levels of polarisation along a line at PA ≈ 145 deg. This orientation is nearly parallel to the polarisation angle of HL Tau and to the proposed disc equatorial plane. If the lower levels of polarisation are attributed to a degree of competition between the scattering pattern centred on HL Tau and the polarisation due to extinction by aligned grains within the disc, then the geometry observed in Figure 5.7 supports the earlier contention of a magnetic field lying predominantly within the plane of the disc.

5.3.2 The Jet Region

Previous observations of the jet region in HL Tau were outlined in §5.1 and a brief description of the appearance of the jet in the new data was given in §5.2.1. In the unfiltered CCD data shown contoured in Figure 5.1 the jet consists of three knots arranged in a linear fashion at PA ≈ 40 deg. This structure can also be seen in the Hα CCD images of Mundt *et al.* (1983)
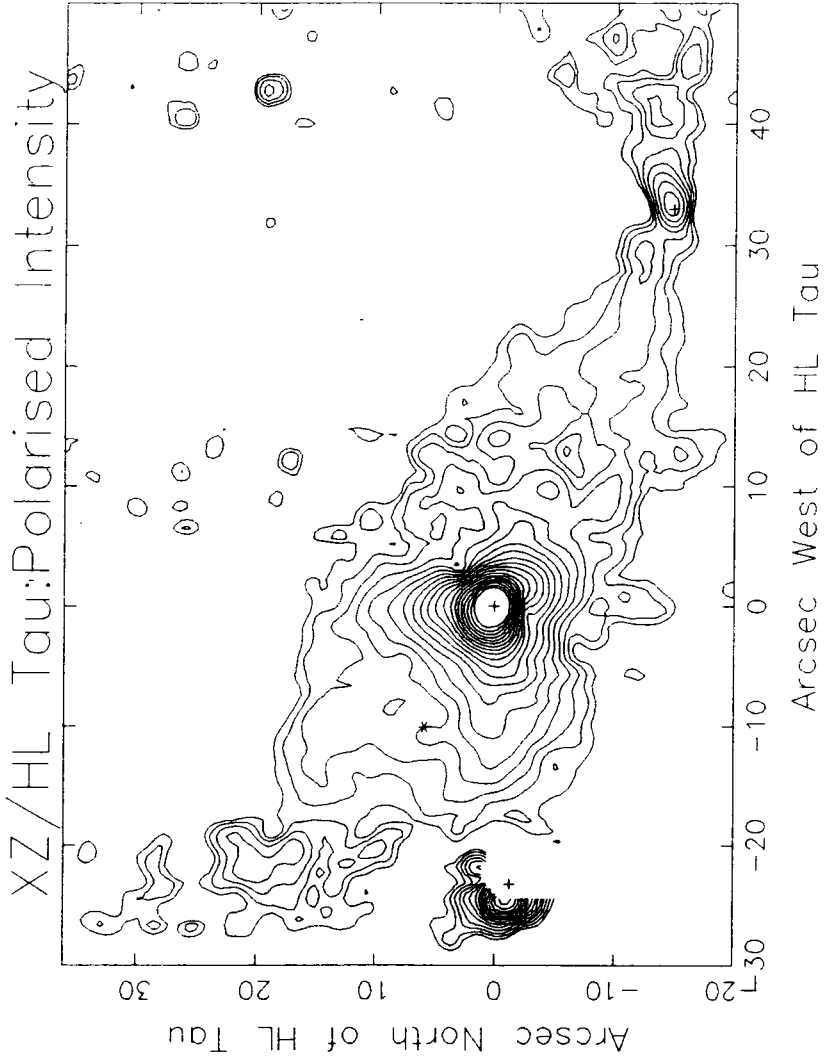
Figure 5.7: Contoured polarised intensity image of the HL/XZ Tau region. The contour spacing is logarithmic with intervals of 0.3 magnitudes.

and to a lesser extent in the narrow band [SII] images of Strom *et al.* (1986). In addition to these three knots, there is a patch of nebulosity to the north-east—apparently detached from the main body of nebulosity—and also a 'spur' on the intensity contours to the south-west near to the location of the VLA source. This spur may correspond to the 'thumb' of [SII] emission detected by Strom *et al.* (1986) at PA 40 deg. to the north-east of HL Tau. Although all of these features are approximately colinear, the manner in which they are related to one another and to the presently known sources in the HL/XZ Tau system is not clear.

In the polarisation maps of Figure 5.2 and Figure 5.3 the vector orientations in the jet region are typical of the uniform curvature scattering pattern centred on HL Tau, with no indication of a correlation between the intensity structure of the jet and the polarisation PAs. This observation is augmented by the radial polarisation plot shown in Figure 5.6 which shows that, although deviations from circular centrosymmetry about HL Tau clearly exist, they do not correlate with the jet structure. In addition, this polarisation map shows no evidence for the illumination of the nebulosity from the position of the VLA source (the optical invisibility of this VLA source does not, on its own, eliminate it as an illuminating source—HH1 and 2 in L1641 appear to be illuminated by an optically invisible VLA source). A further polarisation map with measurements made at selected positions in and around the knots of nebulosity that comprise the jet is shown in Figure 5.8. The polarisation angles have been turned through 90 deg. so that for scattering from a central source the vector orientations should be radial with respect to that source position. The polarisations at the positions of the three knots appear consistent with illumination from the direction of HL Tau as does the remainder of the map. There are two explanations for this observed polarisation structure; either (i) the whole of the jet region (including the knots of nebulosity) is seen by the scattering of light originating from HL Tau or (ii) the jet is purely an emission line feature and, therefore, intrinsically unpolarised. In the latter case the scattering arises in the background reflection nebulosity and on the basis of the polarisation data alone it is not possible to constrain the location of the jet exciting source.

Referring back to the contoured polarised intensity image of Figure 5.7 and comparing with the contoured total intensity image of Figure 5.1 it is evident that the 'inner' two knots of the jet, knots A and B at positions
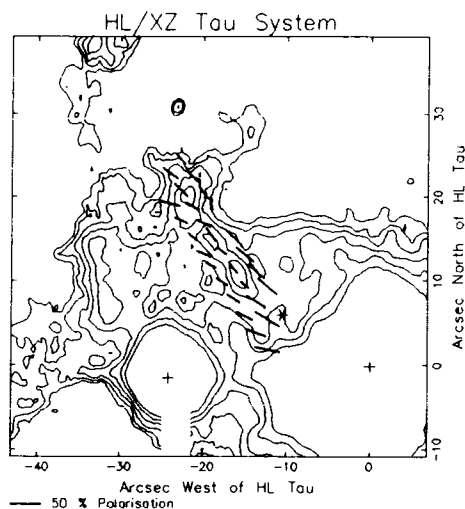
Figure 5.8: Polarisation measurements in the jet region. The vectors are plotted at right angles to the **E** vector so as to appear radial with respect to their source of illumination (assuming simple scattering).

(-19.2,14.9) and (-16.3,10.8) in the arcsec coordinate system centred on HL Tau, are not represented at all in polarised intensity. The third 'outer' knot C of the jet (position (-21.9,20)) corresponds with a region of enhanced polarised intensity which, if intrinsic to the jet, suggests that it contains a significant component of reflected light. However, this region of the map lies within one of the noisy data strips mentioned earlier and so must be treated with increased caution. The detached appearance of the polarsation structure corresponding spatially with the outer knot of the jet may result in part from a less than perfect normalisation between adjacent fields. In view of this an open verdict will be recorded on the polarisation of this outer knot.

The three knots appear approximately colinear on the plane of the sky and, at first sight, would seem to represent a physically coherent structure. However, this does not obviate curvature in or out of the plane of the sky. As mentioned previously, the three knots also appear in the $H\alpha$ CCD images of Mundt and Fried (1983) and in the [SII] CCD images of Strom *et al.* (1986), although the line emission from knot C appears fainter than that from knots A and B. Examination of the narrow band [SII] images

of Strom *et al.* (1986) reveals that the jet appears to change shape with wavelength and in addition, as the wavelength increases, the end of the jet (knot C) gradually disappears.

This suggests that the emission from the outer knot is more blue shifted than that from the rest of the jet material, an effect that could be explained if the jet bends towards us with distance from HL Tau. An alternative explanation would be that the jet material is accelerating/decelerating with distance from its exciting source. The change in shape of the jet with wavelength, if a real effect, is more difficult to account for, but if different regions of nebulosity are being picked up at different wavelengths then this raises the possibility of a system of outflowing gas more spatially extensive than that identified with the original jet.

As well as being bright in [SII], the jet is clearly visible in the $H\alpha$ frame of Strom *et al.* (1986) wherein there is evidence to suggest that the inner knots may be connected to the star (HL Tau) by a faint spur of emission nebulosity. If this is the case, then it would necessitate a curvature of the inner portion of the jet since, as mentioned previously, a projection of the axis defined by the three bright knots would pass to the south of HL Tau. It must be said that, on the basis of the data presently available, it is not possible to distinguish between HL Tau and the VLA source as the exciting source of the jet. There appears to be nothing special about the VLA source except that it lies close to the bright optical region of the jet which is also detected in the VLA survey (Strom *et al.* 1986 referring to Brown *et al.* 1985). However, if it can be shown that the jet is curved, then this factor might prove inconsequential, indeed, there would be a possibility of interpreting the VLA source as a region of higher excitation corresponding to the position at which the jet deflection occurs. A curved jet was proposed in the previous chapter in connection with the star Haro 6-5B, although in that case there were no additional contending sources.

Another interesting feature of the [SII] images of Strom *et al.* (1986) is the bright patch of nebulosity to the south of HL and XZ Tau visible in both the -80km s^{-1} and $+30$km s^{-1} frames (but slightly brighter in the latter) and which these authors refer to as the 'southern jet'. This structure is clearly visible in our unfiltered CCD data (Figure 5.3 for example) although it appears much fainter than the majority of the nebulosity in the region. A polarisation above the imposed cuts is detected in the two brighter knots of the emission structure but it is not possible to confidently attribute it to the

effects of illumination by HL Tau, which is responsible for the vast majority of the polarisation in the region. Another reason to doubt the association of the [SII] structure with HL Tau is that its position, relative to HL Tau, is difficult to reconcile with the disc and outflow theory expounded in the previous section since it lies close to the equatorial plane of the disc and would also appear to lie outside the proposed outflow structure as defined by the 'disc horns'. If we wish to associate this southern [SII] feature with the jet, also quite visible in [SII] emission, then this argument would tend to weaken the association of the jet with HL Tau. The angle subtended by the jet and the southern [SII] feature at the location of the VLA source is less than the 180deg. expected for diametrically opposing outflows but then again it is greater than the angle subtended at the position of HL Tau.

5.3.3 XZ Tau and LkHα358

The suggestion of a link between the star XZ Tau and the nebulosity in the region has so far been avoided on the basis that it does not appear to be responsible for the illumination of any of the observed reflection nebulosity and that its level of polarisation is atypical of values expected from observation of other stars identified with PMS outflow activity (the polarisation of HL Tau is at the opposite extreme). However, the XZ Tau region has been mapped using relatively short exposures and so polarisations of less than about 10 per cent would not be detected.

The polarisation of XZ Tau (Table 5.1) is very similar in level and orientation to the value calculated for the intrinsic polarising effect of the dust within the Taurus clouds (1.8 per cent at PA 75 deg.), suggesting that it is a field star located behind the clouds and not involved with the SF activities in L1551. However, the classification of XZ Tau as a T Tauri star is a testamnent to its youth and supports an association with a SF region such as L1551. Association with L1551 is also suggested by the proper motion measurements of Cudworth and Herbig (1979) which show that XZ Tau, HL Tau and several other emission line stars in the vicinity all share common proper motion vectors within the errors. Two solutions seem possible; either XZ Tau is intrinsically unpolarised and is located at the back of (but still within) the Taurus clouds in which case its apparent association with HL Tau is a line of sight coincidence; or, XZ Tau is intrinsically polarised in which case it could be located anywhere along the line of sight—

but still preferably within the Taurus clouds. In contrast, the polarisation angle of HL Tau is similar to that of L1551 IRS5 (a well identified outflow source) in the IR and VSS4 (situated close to the IRS5 outflow).

The star LkHα358 supports its own reflection nebulosity independent of that associated with HL Tau. The east-west elongation of this nebulosity is apparent (Figure 5.1) as is the brightness spike to the east of the star. This spike is also visible in the contoured polarised intensity image of Figure 5.7 (suggesting that it represents a region of enhanced light scattering) but appears positionally displaced from an axis running east-west through the star. The polarisation of LkHα358 (Table 5.1) is significantly above the 1.8 per cent level of the background stars and the angle of the polarisation is approximately perpendicular to the east-west nebular elongation. It is therefore suggested that the star LkHα358 is surrounded by a disc of obscuring and polarising material oriented with equatorial plane in a north-south direction and is responsible for the illumination/production of a bipolar outflow of material occurring along an east-west axis. In this scheme, the brightness spike could be caused by the reflection of light from the eastern cavity wall, naturally explaining the positional offset from the outflow axis. Such an effect is seen in other PMS systems, for example R Mon (Warren-Smith *et al.* 1987a). The proposed HL Tau and LkHα358 outflows appear to intersect on the plane of the sky to form the 'crossover' region of polarisation seen in Figure 5.4 and described in §5.2.2.2, and their relative size suggests that the LkHα358 outflow may lie some distance behind that of HL Tau (assuming the size differences are not due to evolutionary effects).

5.4 Discussion and Summary

The geometry proposed for the HL/XZ Tau system comprises two bipolar outflows, one centred about HL Tau and one about LkHα358, with axes oriented approximately perpendicular to the equatorial planes of their respective circumstellar discs (which lie at PA 143 deg. in the case of HL Tau and PA 4.2 deg. for LkHα358—as defined by the polarisation data).

The jet of Mundt and Fried (1983) appears to be contained within the north-eastern lobe of the HL Tau bicone (which is envisaged as accounting for the majority of the nebulosity in the region) although it is not entirely

clear whether it is causally associated with HL Tau or with some other source (for example, the VLA source—Mundt *et al.* 1987). The angle between the jet axis ($\approx$ 40 deg.) and the equatorial plane of the disc as determined from the polarisation measurements is about 77 deg. although there is evidence to suggest that the jet is not straight. It is suggested that the HL Tau bicone is tilted relative to the plane of the sky such that the north-eastern lobe projects towards us whereas the south-western lobe projects away from us into the L1551 cloud material. The LkHα358 outflow may also be tilted so that its western lobe is the more obscured explaining, perhaps, why a brightness spike is not seen to the west of this star.

The molecular line observations of Torrelles *et al.* (1987) indicate the presence of both red and blue shifted CO emission in the HL/XZ Tau region (§5.1). If, as they suggest, the red shifted gas is part of the extensive L1551 IRS5 outflow, located to the south, and only the blue shifted component is indigenous to the HL/XZ Tau region, then the location of this blue shifted lobe to the north-east of HL Tau is entirely consistent with the disc-outflow geometry presently suggested for this star. This blue shifted emission may, therefore, represent the molecular counterpart of the optical outflow proposed in §5.3.1.

The map of Figure 5.3 shows evidence for the existence of null points in the polarisation on either side of HL Tau at $\approx$ 5 arcsec from the stellar centroid and within the plane of the circumstellar disc (PA 143 deg.). The generation of such null points will be discussed in §7.1.2 and §7.1.3 in the case of both scattering and aligned grain models. If the nebulosity is illuminated by an intrinsically polarised source, the location of the null points relative to the star may give some indication of the inner radius of the (dusty) circumstellar disc although in the case of the aligned grain model the location of the null points depends upon the degree of overlying polarisation by extinction. At a distance of 140pc, 5 arcsec $\approx$ 700AU and, in addition, the radial extent of the nebulosity in Figure 5.3 along a line at PA 143 deg. is about 17 arcsec suggesting an outer disc radius of $\approx$ 2,500AU. The latter figure can be compared with the outer radius of 1600AU determined by Beckwith and Sargent 1987 (for a distance of 160pc). Assuming a molecular hydrogen density of 10^6cm^{-3}, a disc of radius 2,500AU (and thickness of 700AU) would have a mass of $\sim$ $10^{-1}M_\odot$—of the same order as the mass estimated for the HL Tau disc by Beckwith and Sargent. However, this figure appears to be too small by at least

one order of magnitude to support a disc driven molecular outflow. For example, in order to produce the nearby L1551 IRS5 molecular outflow, the hydromagnetic acceleration model of Pudritz and Norman predicts a disc of mass $\approx 10M_\odot$ around IRS5 (Pudritz and Norman 1986b). Although blue shifted CO emission has been detected to the north-east of HL Tau a bipolar outflow centred on this star is not seen and this, then, may be due to an insufficiently massive circumstellar disc. Three possibilities can be forwarded at this point:

1. HL Tau is one of the youngest PMS stars observed (as suggested by Cohen 1983) and is still in the process of building up a large circumstellar disc. Eventually, this disc will become sufficiently massive (and will have entrained sufficient magnetic flux) to power a molecular flow and will become sufficiently dense in its central regions to collimate the light from HL Tau into channels along its polar axis forming a bipolar nebula. In this scheme, the blue shifted CO to the north-east of HL Tau represents an emerging molecular outflow and the optical structure outlined in Figure 5.1 represents a prototype bipolar nebula, as suggested in §5.3.1.

2. HL Tau is an evolved PMS star and much of the material that surrounded the star has been dissipated to leave the 'remnant' material seen today. Such a dissipation could have been facilitated by a strong stellar wind or by a past molecular outflow phase. In this scenario, the disc material may be in the process of forming planets (as suggested by Cohen 1983 and Beckwith and Sargent 1987). The CO emission to the north-east of HL Tau now represents the remains of the past molecular outflow and what may have once been a bipolar nebula has now become indistinct due to the dissipation of the collimating disc.

3. There was insufficient mass in the protostellar condensation out of which HL Tau formed to produce a circumstellar disc capable of powering a molecular outflow or efficiently collimating the light from HL Tau.

Chapter 6

The PV Cephei System

In 1977, Cohen *et al.* and Gyulbudaghian *et al.* reported remarkable changes in the optical appearance of the nebulosity (GM-29) associated with the variable star PV Cephei near NGC7023. A 1952 August 8th sky survey red print of the region shows a linear 'streak' of nebulosity almost 1 arcmin in length and clearly detached from PV Cephei, whereas in the 1976 December 26th image of Cohen *et al.* (1977) the streak had disappeared to be replaced by a fan shaped nebulosity with PV Cephei at its southern apex. The object had adopted a structure typical of cometary nebulae. Cohen *et al.* (1977) estimate a spectral type A5 V with $A_v = 7.9 \pm 0.2$ magnitudes for PV Cephei and suggest that the star brightened considerably between 1952 and 1976.

Cohen *et al.* present a series of observations detailing variations in the brightness of the star PV Cephei and in the luminous structure of its associated nebulosity between 1977 July and 1979 November. During this period, there is evidence for the intermittent presence of the streak first seen on the 1952 plate and which in the images of Cohen *et al.* (1981) appears as a curving extension of the eastern edge of the northern nebular fan. A bright bar is seen to the north of PV Cephei in several of the images and appears to be separated from the star by a 'gap' or area of decreased nebular brightness. There is also evidence to suggest that the brightness variations of the star are periodic with changes of several magnitudes over periods of months. The model proposed by Cohen *et al.* (1981) involves the conical illumination of ejected material by a T Tauri star—PV Cephei—surrounded by a dense circumstellar torus. In this model, the bar to the north of PV

Cephei is identified with the inner edge of this torus, (shock excited by the strong winds from PV Cephei) and the variations in the luminous structure of the nebular fan are temporally correlated manifestations of the stellar brightness fluctuations.

Levreault (1984) presents CO observations of the region which reveal the presence of a bipolar molecular outflow centred on PV Cephei with the blue shifted lobe to the north of the star and the red shifted lobe to the south. This velocity distribution confirms the nebular tilt suggested by Cohen *et al.* (1981). However, the outflow axis appears skewed relative to the symmetry axis of the optical nebulosity and the blue shifted lobe is spatially more extensive and lies at a greater distance from PV Cephei than the red shifted lobe to the south of the star. The latter observation is taken, by Levreault, as evidence of a density gradient within the surrounding cloud material which operates to restrict the progress of the red shifted outflow which is oriented into the cloud. In contrast, the blue shifted lobe is oriented towards the edge of the molecular cloud and can, therefore, expand more freely. The model invoked by Levreault (1984) is, in many respects, similar to that of Cohen *et al.* (1981) with the exception that the collimated stellar wind excavates two oppositely directed cavities in the molecular cloud and it is the reflection of starlight from the inner walls of the northern cavity that is responsible for the optically visible nebulosity. The location of PV Cephei within a dense globule associated with the L1158 cloud lends further credibility to a PMS interpretation of its nature.

The bipolar nature of Levreault's model predicts the existence of an optical counterpart to the nebulous fan seen to the north of PV Cephei which would correspond to the red shifted molecular flow. Both Levreault and Opal (1987) and Neckel *et al.* (1987) report the presence of an optically visible counterfan to the south of PV Cephei and note its reddened appearance in comparison with the northern fan. In fact, the southern counterfan was first detected in CCD frames taken in 1984 June by Scarrott *et al.* (1986). Additionally, Neckel *et al.* (1987) report the existence of blue shifted HH emission lines at two points in the northern fan.

Torrelles *et al.* (1986) failed to detect ammonia emission towards the PV Cephei region suggesting an upper limit of 1.4 arcmin for the dimensions of any high density gas structure.

Date	Filter	Detector	Mode	Focus
Aug 81	Re	Elec'graph	Direct[1]	f/7
Jun 84	V,R,I	GEC CCD	Direct[1]	f/13.5
Jun 84	None	"	Polarimeter	"
Aug 84	I	"	"	"
Oct 85	R	RCA CCD	Direct	f/7
Jul 86	R	"	Polarimeter	f/13.5

[1](A focal plane reducer, used in all the polarimetric observations, was also used here)

Table 6.1: A summary of the observations to be discussed in this chapter.

6.1 Present Observations

Polarimetric and direct imaging of PV Cephei and its nebulosity is presented covering a 5 year period from 1981 Aug to 1986 Jul. Data were recorded at the 1m telescope of the Wise Observatory, Israel, using a variety of detectors and filters. The observations are summarised in Table 6.1 and the spectral characteristics of the filters appear in Table 3.1. All the data were obtained and reduced in a similar fashion using common observing and reduction techniques (§3.2). The polarimetric observations were made with the Durham CCD Imaging Polarimeter described in §3.2. The exposure times for individual CCD frames are typically between 5 and 10 minutes, a number of these exposures being combined to make a final image.

6.1.1 Imaging Observations

Figure 6.1 shows a greyscale representation of the PV Cephei region covering a field approximately 7 arcmin square (north is up and east is left). The image is derived from a combination of three direct I-band CCD frames taken in 1984 June. The nebulosity associated with PV Cephei is located left of centre and clearly comprises two fan-shaped structures together forming a bipolar or biconical nebula centred on the star. The brighter northern lobe was first observed in 1976 whereas the smaller southern fan is the one
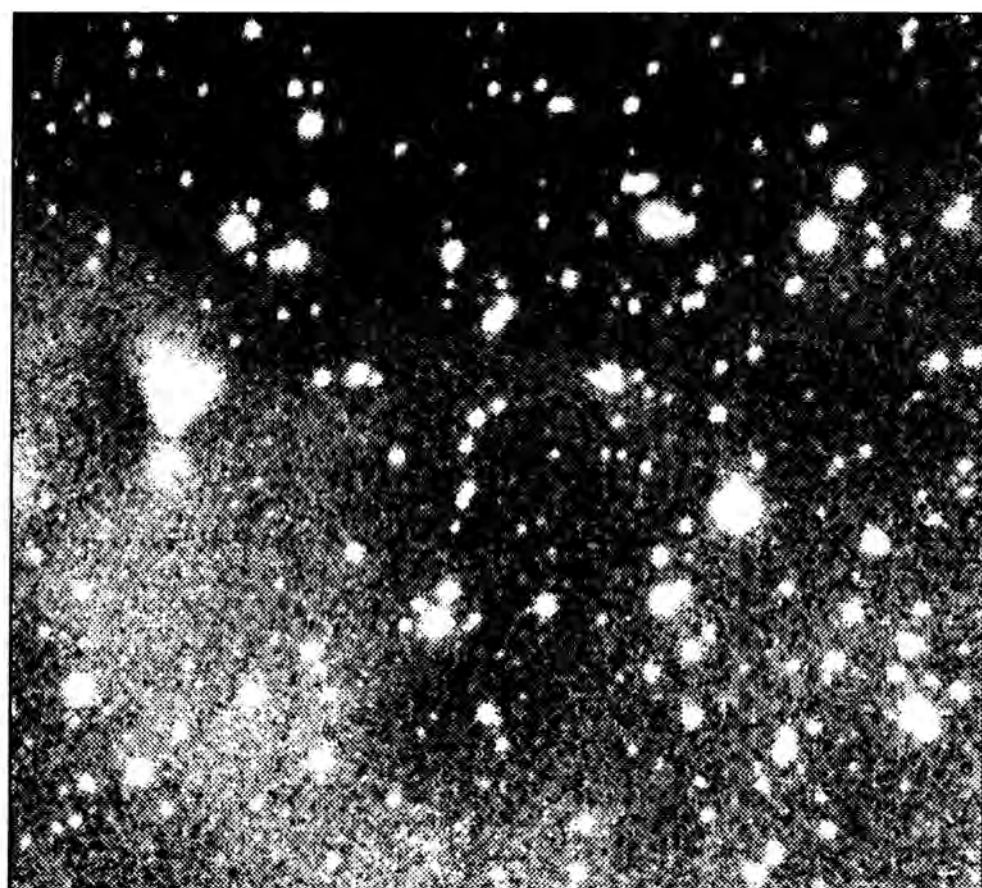
Fig 6.1

PV Cephei region: I band 1984 Jun

first seen by Scarrott *et al.* (1986).

Surrounding the brighter nebular regions is the extensive faintly luminous cloud material which covers most of the field. PV Cephei lies close to the northern boundary of this cloud which is also angled approximately perpendicularly to the biconical axis of the bright nebulosity. A paucity of stars in the vicinity of PV Cephei suggests that the object may have formed within a particularly dense region of the cloud—an observation augmented by the dark area to the immediate east of the star.

Figure 6.2 shows a sequence of greyscale pictures of PV Cephei and its nebulosity derived from V,R and I-band (left to right) CCD images at low and high brightness levels (top and bottom respectively). All of these images were obtained in 1984 June, at which time the object exhibited an 'hourglass' structure typical of bipolar nebulae with no evidence of the previously observed streak, even at the lowest brightness levels. In all three wavebands the northern nebular fan is separated from the image of PV Cephei at brighter levels by a dark lane several arcsec wide which can be identified with the 'gap' described by Cohen *et al.* (1981). A similar dark lane or gap, this time visible at low light levels and especially in the I-band image, separates the southern counterfan from the star. The southern fan is not discernible in the V-band and becomes progressively more evident through R and I. Although the brightness of the northern fan varies between the three wavebands (a conclusion endorsed by Levreault and Opal 1987 for their filter system) the variation is nowhere near as dramatic as that of the southern fan suggesting that the light from the southern fan is much more heavily reddened. This point ties in with the previously proposed models of the system and the CO observations of Levreault (1984) which require that the axis of the PV Cephei bicone be inclined such that the southern lobe projects into the plane of the sky and into the dense interior of the parental cloud.

To the immediate east of PV Cephei and visible against the faintly luminous cloud material, an approximately triangular dark region can be seen which appears to fit neatly into the obtuse angle formed by the eastern edge of the PV Cephei bicone. A similar but smaller and fainter dark region exists to the west of PV Cephei. The appearance of these dark regions varies between the three wavebands as would be expected if they result from the obscuration of the background light by an intervening dense portion of the cloud. However, the level of the cloud luminosity increases from V to
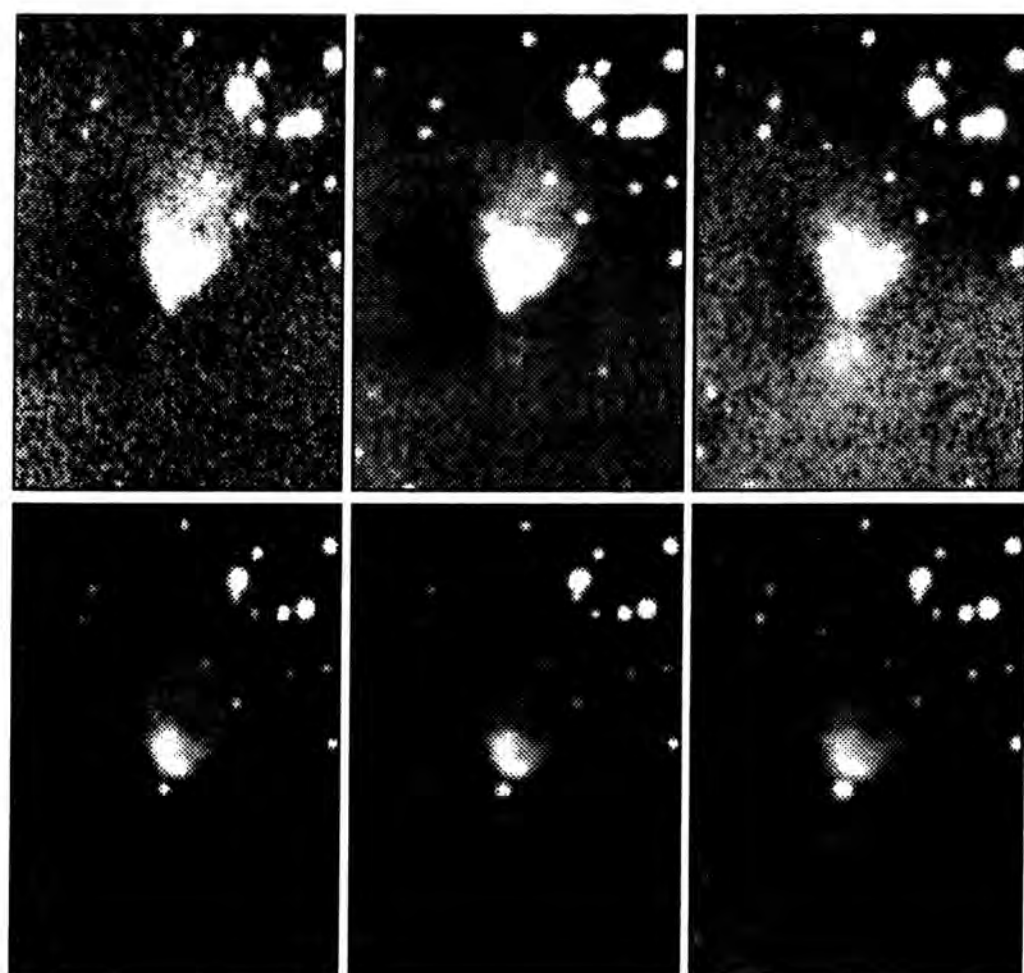
Figure 6.2

V/R/I band images (1984 Jun)

I, as evidenced by the relative prominence of the cloud boundary to the north of PV Cephei, so that optimum contrast between the dark regions and the surrounding cloud occurs in the R-band. Figure 6.2 also shows variations in the structural appearance of the northern fan between the three wavebands (particularly along the eastern and western edges) and in the relative brightness of the star and nebula.

The changes in the optical appearance of the PV Cephei nebulosity with time were followed quite closely in the late 1970s by Cohen *et al.* (1981) and are described briefly in the opening section of this chapter. Prior to 1976, however, little is known of the history of this variable nebula other than its appearance as a linear streak on the 1952 sky survey plates. The observations presented in this chapter extend the monitoring of this object into the 1980s and reveal a continuing sequence of changes in its optical structure during the period 1981 Aug to 1986 Jul. The greyscale pictures of Figure 6.3 show PV Cephei as it appeared at various times during this period. The pictures are derived from direct R-band imaging with both electronographic and CCD detectors and are displayed at low and high brightness levels (top and bottom respectively).

The 1981 electronograph image clearly shows the presence of the streak which has characterised this object well in the past. There is no evidence of the streak in the 1979 Nov image of Cohen *et al.* (1981) suggesting a reappearance of this feature during the interim period of 2 years. As seen in 1981 the streak forms a curving northerly continuation of the eastern edge of the northern fan which was also present at this time and extends for approximately 115 arcsec along its arc from the star. At a distance of 500pc (Cohen *et al.* 1981) 115 arcsec corresponds to approximately 1 lightyear on the plane of the sky which strongly suggests that the secular nature of the streak results from variable illumination. Such a conclusion is supported by the R-band image taken in 1984 Jun (Figure 6.3) at which time the streak was again absent. The change in the luminous structure of the nebula between 1981 and 1984 appears to have resulted almost entirely from the fading of the streak with comparatively little change in the brightness of the northern fan. The latest R-band image of 1986 Jul shows some evidence for a reappearance of the streak although it does not have the prominence of the feature observed in 1981.

Although the southern counterfan was seen for the first time in 1984 it is not possible to say whether or not it was present in 1981 since (at the
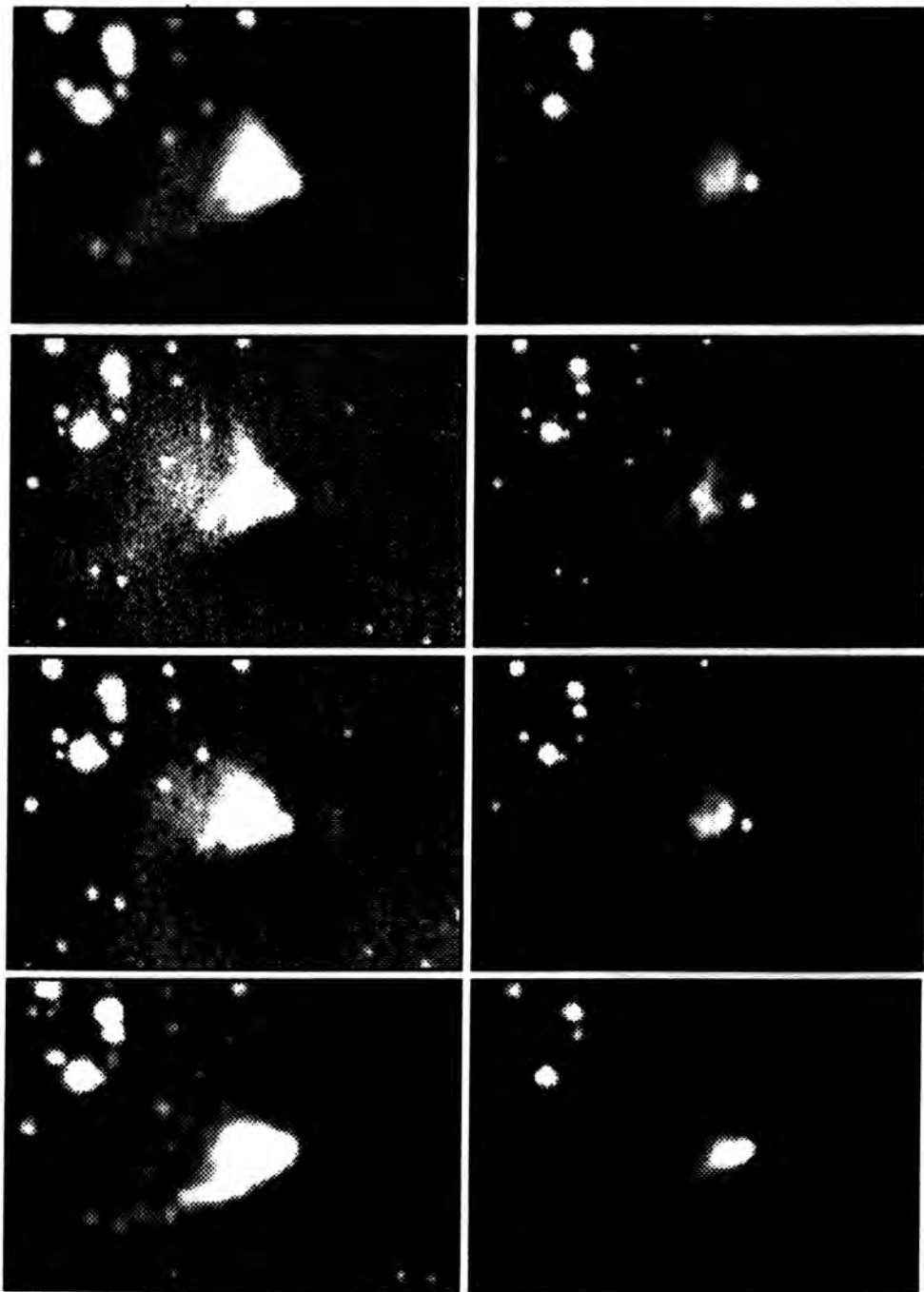
Figure 6.3

R band images 1981 Aug/1984 Jun/1985 Oct/1986 Jul

brightness levels observed in 1984) it would have been below the detection threshold of the electronographic data. Its appearance in the 1984 CCD images may, therefore, result from the increased detector sensitivity rather than from any real brightening.

The luminous bar to the north of PV Cephei, separated from the star by the dark lane and clearly visible in the V, R and I images of Figure 6.2 (1984 Jun), was interpreted by Cohen *et al.* (1981) as the inner shock excited edge of a collimating torus centred on PV Cephei and as such would be expected to represent a relatively permanent nebular feature fixed in space. However, the bar is completely absent from the R-band image of 1985 Oct (Figure 6.3) which instead shows a more extensive and irregular patch of nebulosity further to the north. By 1986 Jul the bar had reappeared, the northern irregular patch of nebulosity had disappeared and the object looked very much as it did in 1984 Jun except for the more extensive appearance of the nebular fan and the observed tendency for the streak to reappear. These changes strongly suggest that the bar, like the streak, is a transient illumination effect.

The fluctuations in the internal structure of the northern fan have been accompanied by changes in its overall shape. Whereas in 1984 Jun the eastern and western edges of the fan were curved convexly so as to form a parabola, by 1985 Oct (when the bar was absent) the edges had straightened and even become slightly concave outwards. Again these changes were reversed by 1986 Jul by which time the convex shape had reasserted itself.

Since 1981, the apparent major axis of the northern lobe has rotated towards the west. In 1981 it was oriented almost exactly north-south whereas in the most recent image (1986 Jul) it is at PA 345 deg. This rotation reduces, but does not eliminate, the difference in PA between the optical axis and the axis of the CO outflow noted by Levreault (1984).

A summary of the main changes in the optical appearance of the nebular features (streak, bar and fan) can be found in Table 6.2.

6.1.2 Polarimetry

The imaging polarimetric observations of PV Cephei to be discussed in this section were obtained on two separate occasions in 1984. A comparison between the direct images and the polarimeter images of 1984 Jun and 1984 Aug suggests that there was very little change in the optical appearance of

Date	Opening Angle deg.	PA of Nebular Axis deg.	Appearance
1981 Aug	73	0	Streak and N fan both present. S fan not detected. Bar and gap seen previously not evident.
1984 Jun	72	347	Streak disappears, bar and gap visible, S fan seen for the first time separated from the star by dark lane.
1985 Oct	70	345	No streak. Bar disappears to be replaced by nebulosity further to the N. Dark gap appears to brighten or fill in. Overall shape of N fan changes.
1986 Jul	73	345	Bar and gap back again. Appearance very similar to 1984 Jun except for slight evidence of the streak.

Table 6.2: A summary of the changes observed in the optical appearance (R-band) of the PV Cephei nebulosity between 1981 Aug and 1986 Jul. The PAs of the nebular axis are for the northern fan only.

PV Cephei and its nebulosity between these two dates. The polarisation maps corresponding to these two observations (the unfiltered and I-band maps—Table 6.1) will, therefore, be discussed jointly on the assumption that any innate differences result from the different passbands used.

Figure 6.4 and Figure 6.5 show two linear polarisation maps derived from the unfiltered and I-band CCD observations of 1984 Jun and 1984 Aug respectively. The maps are superimposed on contours of total intensity (spaced at 0.35 magnitude intervals) which reveal the appearance of the nebulosity at the time of the polarimetric observations. These contours show the star PV Cephei, the bipolar arrangement of the northern and southern fan, the bright bar to the north of the star and the intervening dark gap. The spatial coverage of the observations is incomplete and the polarimeter field is slightly displaced in R.A. between the two maps with the result that only the central regions (± 10 arcsec east-west of the star) are duplicated. In both cases, the integration bins are 5 pixels (≈ 6 arcsec) square with inter-bin spacing of 3 pixels (≈ 3.6 arcsec)

The polarisation maps show little evidence for the centrosymmetric vector pattern typical of many bipolar nebulae (*e.g.* R Mon, Warren-Smith *et al.* 1987a) and symptomatic of the scattering of starlight by the nebular lobes. The classification of the northern fan as a reflection nebula (Cohen *et al.* 1981) is, therefore, immediately in doubt. Instead, the vector patterns appear uncorrelated with the underlying brightness maps, the polarisation levels seem to decrease systematically from south to north and the vectors show a tendency to be oriented in a north-east south-west direction although regional variations are quite evident. A more detailed examination of these polarisation maps reveals a number of unusual features:-

1. Despite the novelty of the majority of the polarisation pattern, a familiar feature can be seen in the vicinity of PV Cephei. A substantial degree of polarisation is recorded for this star, which is similar in level and angle to that measured in the immediately surrounding nebulosity. The result is the band of parallel vectors which has been found to characterise the optical polarisation measurements of other PMS objects associated with bipolar nebulosity and molecular outflow and which seems, therefore, to be an integral part of this energetic phase of early stellar evolution. The discovery of anomalous polarisation patterns in the vicinity of two more identifiably PMS systems (Haro 6-5
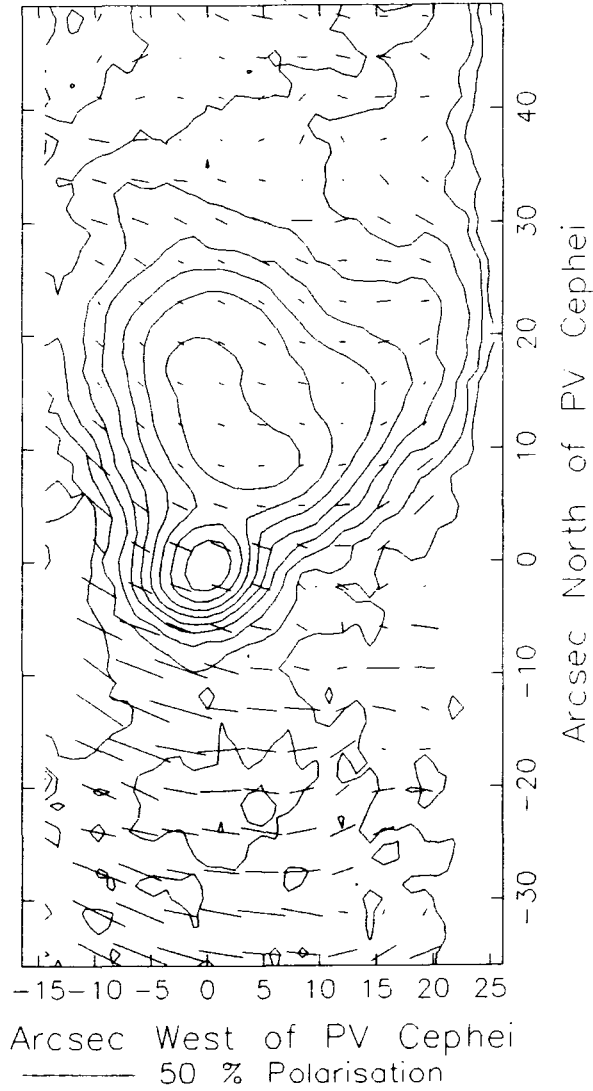
Figure 6.4: An unfiltered linear polarisation map of the PV Cephei nebulosity taken in 1984 Jun and described in the text.
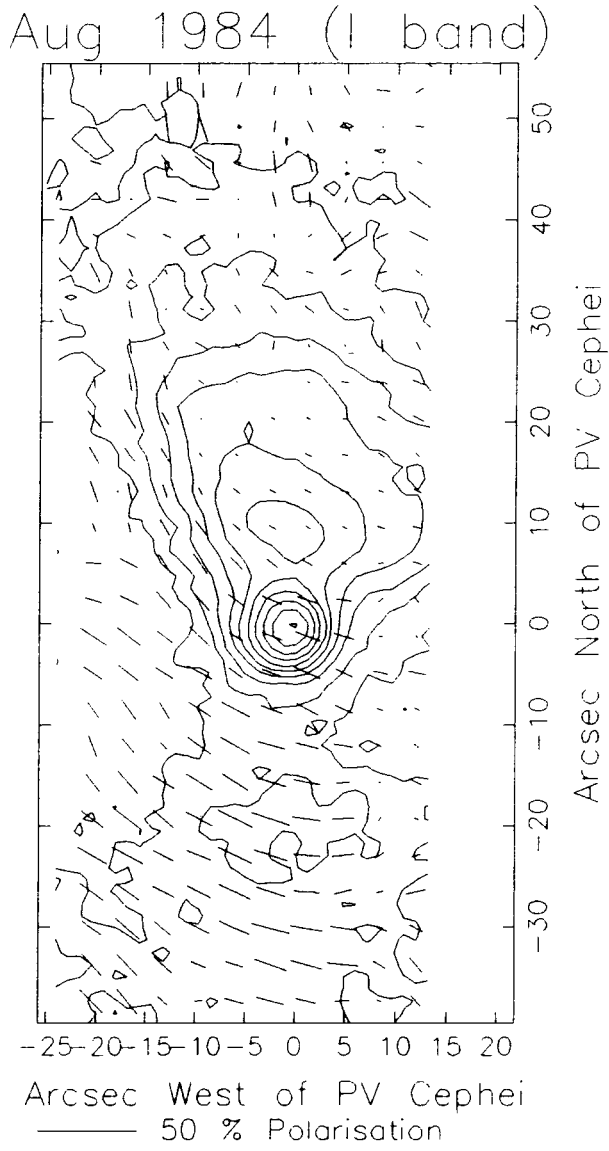
Figure 6.5: An I-band linear polarisation map of the PV Cephei nebulosity taken in 1984 Aug and described in the text.

and HL Tau) has been discussed in the preceeding chapters where an interpretation in terms of the polarising effects of magnetically aligned dust grains within circumstellar discs was found to be an attractive explanation. Since a circumstellar disc around PV Cephei has already been proposed (Cohen *et al.* 1981) a similar interpretation may be viable in the case of this object (§6.2). Polarisation measurements for the star PV Cephei, obtained by integrating within a circular aperture of diameter 5 pixels ($\approx$ 6 arcsec) centred on the star, are listed in Table 6.3. The polarisation angles of the star and the central parallel band region are approximately perpendicular to the major axis of the northern fan (Table 6.2) which is itself rotated about 15 deg. east from the CO outflow axis (Levreault 1984).

2. Towards the southern fan levels of polarisation in the range 10 → 15 per cent are typical with vector orientations contributing to a mildly curved pattern initially suggestive of reflection nebulosity illuminated by PV Cephei. However, a closer inspection of the map reveals that it is not circularly centrosymmetric about PV Cephei but is instead symptomatic of the north-east south-west trend in vector orientations typified by the polarisation band overlying the central star. This trend extends into the dark lane separating the southern fan and the central stellar region and also into the dark material to the east of the star (especially visible in the I-band map) so that the whole area composes a regular pattern indifferent in form to the underlying brightness distribution and the presence of PV Cephei. Some residual evidence of a scattering pattern does exist in the southern fan and a comparison of the two maps reveals a closer approximation to a scattering pattern centred on PV Cephei in the case of the unfiltered data. This suggests a wavelength dependence of the polarisation pattern with the effects of polarisation due to scattering becoming more apparent at longer wavelengths (a combination of the red colour of the object, the I filter passband and the spectral response of the CCD give the unfiltered data the longer effective wavelength).

3. The eastern edge of the northern fan is of particular interest since it corresponds in position with the enigmatic streak (§6.1.1) intermittently visible in this object. Although the streak was absent throughout our polarimetric observations, the vector pattern in this region

is decidedly unorthodox. The streak region is best covered by the I-band map of Figure 6.5 which shows levels of polarisation in the range $7 \to 12$ per cent with vectors oriented along the eastern edge of the fan, being in places parallel to the brightness contours. The resulting pattern forms a band of polarisations matching positionally the luminous streak but persisting when the latter is absent. This band is inclined relative to the band overlying the star but connects smoothly with it to form a single continuous arc. The vector orientations in the streak region are essentially radial relative to PV Cephei and orthogonal to the 'tangential' angles expected for polarisation induced by the scattering of light from this central object. Looking at the unfiltered map, these effects are less obvious than in the I-band map, partly because of the incomplete spatial coverage of the streak region in these data. In addition, however, the vectors do seem more inclined to the eastern edge of the northern fan in the unfiltered map and appear similar in orientation to the parallel band of polarisations in the central (PV Cephei) region. As a result, the continuous arc of polarisation seen in the I-band data does not appear although a scattering pattern centred on PV Cephei is still not evident. Again, a wavelength dependence of the polarisation pattern is suggested with vectors tending to rotate anticlockwise between the I-band and unfiltered maps.

4. The polarisation levels throughout the remainder of the northern fan are identifiably lower than those observed elsewhere in the PV Cephei system with values of 5 per cent or less being representative. In both the unfiltered and I band maps, the polarisation pattern in the vicinity of the bright bar is similar to that overlying the star and the southern fan (with the exception of the lower percentage levels) although between the two maps the previously mentioned anticlockwise rotation of vectors is evident. Further to the north null points in the polarisation pattern are seen in the I-band map which mark the onset of a region of chaotic polarisation extending to the northern edge of the field. A similar chaotic region appears in the unfiltered map but displaced further to the north. These chaotic regions are not due to the effects of noise (since the northern tip of the fan is still quite bright) but must instead represent an unusual combination of polar-

Date	Waveband	P (%)	PA (deg.)
1984 Jun	Unfiltered	9.7 ± 0.9	71 ± 3
1984 Aug	I	11.4 ± 0.8	72 ± 2
1986 Jul	R	13.5 ± 0.9	74 ± 2

Table 6.3: Polarisation measurements of PV Cephei for a 5 pixel ($\approx$ 6 arcsec) diameter circular aperture.

ising influences. In general, the polarisation pattern in the northern fan appears more orderly in the unfiltered data. The western edge of the northern fan is best covered by the unfiltered map which shows a continuation of the polarisation pattern seen in the bright bar region with perhaps a slight increase in the percentage levels. There is also a slight tendency for the vectors to turn up along the edge of the fan as observed on the eastern side. Unfortunately, this region is not covered by the I-band data in which the edge-aligning effect appears to be more prominent.

6.2   Interpretation

An interpretation of the PV Cephei system must address the two main issues raised by the observations of the preceeding section. Firstly, although the PV Cephei system exhibits a typical bipolar morphology, its polarisation is largely atypical. Unlike structurally similar objects (*e.g.* R Mon) the polarimetric observations show no evidence of a reflective origin of the bright nebulosity. Secondly, the northern fan undergoes repeated and dramatic changes in luminous structure on timescales $\sim$ months.

On the basis of the polarisation maps of Figure 6.4 and Figure 6.5 it is not possible to distinguish between the central star and the nebular lobes (except for the lower percentage levels in the northern fan). Instead the vectors form part of a regular pattern covering the great majority of the field suggesting a single polarising mechanism of significant spatial extent. The uniformity of the polarisation pattern and the independence of the nebular brightness imply that the mechanism of polarisation is foreground to the PV Cephei system.

Figure 6.6: R-I colour index. Dark regions are relatively red and light regions relatively blue. The same image is displayed at two levels of contrast.

Figure 6.6 shows a greyscale representation of the R-I colour index derived from the direct imaging observations of 1984 June (Table 6.1). The zero point of the index is arbitrary and regions of nebulosity which are relatively redder or bluer appear darker and lighter respectively. The noise contributed by the faintly luminous surrounding cloud material has been removed by imposing intensity cuts on the constituent R and I images.

Immediately apparent is the difference in colour between the northern and southern fans with the southern fan being considerably redder (this result can be deduced directly from the sequence of images in Figure 6.2 which clearly show the southern fan increasing in brightness with wavelength). The relative reddening of the southern fan correlates with previously proposed models of the PV Cephei system and with the CO observations of Levreault (1984) which require that the axis of the PV Cephei bicone be inclined such that the southern lobe projects into the plane of the sky and into the dense interior of the parental cloud. Levreault and Opal (1987) find a roughly linear increase in R-I colour index (for their filter system) between the northern fan, the central regions and the southern fan and conclude that the tilted nebular geometry offers a plausible explanation of

their observations assuming a standard interstellar gas to dust ratio and reddening. However, an additional feature seen in Figure 6.5 is the reddening of the edges of the northern fan relative to its central region, an effect more prominent along the eastern edge. The existence of two dark regions of obscuration to the east and west of PV Cephei was discussed in §6.1.1. The colour data now suggest that these regions of obscuration, evidently associated with the surrounding cloud structure, overlie and redden the edges of the northern fan, especially the eastern edge.

A comparison of Figure 6.5 with the polarisation maps now reveals that, although the vector pattern is independent of the nebular brightness, it is in fact well correlated with the nebular colour. Where the nebulosity is relatively red—in the north-eastern streak, the southern fan and around the star—the polarisation levels are large and the orientations coherent. In the relatively blue central regions of the northern fan, the polarisation levels are at their lowest with the pattern in places becoming chaotic. Some of the highest polarisations are recorded outside the optical bicone in the region of dense obscuration to the east of PV Cephei (described above). These considerations all point to an association of the polarisation with the nebular environment (rather than with the nebulosity itself) and the induction of polarisation by extinction by aligned dust grains contained within the complicated density distribution surrounding this object. Such an interpretation explains naturally the correlation of the polarisation pattern with the nebular colour, since both effects depend directly upon the amount of intervening dust.

If it is assumed that the grain aligning agent is the magnetic field, then this field must be intimately associated with the dark material surrounding and overlying the nebulosity and with the proposed circumstellar disc around PV Cephei. Evidence for a circumstellar disc around PV Cephei includes collimated molecular outflow, collimated optical nebulosity, strong IR excess (Neckel and Staude 1984), dark lanes and patches of obscuration. Evidence that the disc contains a grain-aligning magnetic field is provided by the parallel band of polarisations overlying the star, the relative PAs indicating a toroidal field configuration within the disc. The polarisation measurements for the star can be easily accommodated; assuming a spectral type A5, and a distance of 500pc (Cohen *et al.* 1981) then V= 17.76 (Levreault and Opal 1987) requires a visual extinction of $\approx$ 7 magnitudes which is sufficient to account for the polarisation levels of Table 6.1 assum-

ing a polarising efficiency of about 2 to 3 per cent mag^{-1} which is typical of interstellar dust and DG alignment. If we assume DG alignment in the rest of the nebula then the observed polarisation pattern, at least in the reddened regions, should form a map of the magnetic field projected onto the plane of the sky. The local field lines thus appear to run along the eastern edge of the northern fan— following the streak—and curve round and connect smoothly with the toroidal field trapped within the circumstellar disc. The polarisations in the vicinity of the southern fan suggest this region may be seen through the polarising grains aligned by this disc field.

Polarisation of the nebula by aligned dust grains within the circumnebular and circumstellar material allows a convenient explanation of the observed variation of the polarisation pattern with waveband in terms of a shifting balance between the two polarising mechanisms in operation (scattering and extinction). In the longer wavelength unfiltered data (Figure 6.4) the remnant of an underlying scattering pattern begins to show through the extinction pattern. This is particularly evident along the eastern edge of the northern fan where it is suggested that the magnetic field orientation is essentially orthogonal to the polarisation angles expected for a scattering pattern centred on PV Cephei. In the unfiltered data, an intermediate vector orientation (neither parallel nor perpendicular to the eastern edge) persists.

Relative to the eastern streak, the central region of the northern fan appears conspicuously blue in the greyscale image of Figure 6.5 suggesting that the extinction thought to be responsible for the anomalous polarisations in the former region is less prevalent here. The polarisation maps of Figure 6.4 and Figure 6.5, however, provide little evidence for a scattering pattern (centred on PV Cephei) in this region, indeed, the polarisation levels throughout the majority of the northern fan are unusually low. Such a situation (low polarisation in conjunction with bright nebulosity) would be expected if the northern fan is an emission nebula and, therefore, intrinsically unpolarised. The small polarisation levels observed could then originate within a thin overlying screen of aligned dust grains. Although emission lines are observed in the light from the northern fan, the nebular spectrum appears very similar to that of the star. On the assumption that the emission line spectrum is not emitted isotropically—now a natural consequence of the bipolar morphology— Cohen *et al.* (1981) conclude that

the northern fan is seen by reflection. A reflective origin of the northern fan is suggested by the more recent spectroscopy of Neckel *et al.* (1987) who also detect two small regions of HH emission in the vicinity. In addition, it seems unlikely that the northern fan is an emission line nebula for the following reasons:

1. The optical imaging observations presented in §6.1.1 detail the dramatic changes in the luminous structure of the northern fan over periods $\sim$ months. In addition, the CCD observations of Levreault and Opal (1987) between 1984 August and 1985 August suggest that there were "...no obvious changes in the morphology of the nebula ..." during this period. These images appear very similar to the 1984 June images of Figure 6.2. However, by 1985 October, the appearance of the northern fan had altered radically (as detailed in Table 6.2) indicating that major changes in luminous structure can occur in 2 months or less, which, at 500pc, is the approximate light travel time across the northern fan. In the case of an emission line nebula, changes in the flux of ionising radiation followed by rapid recombination are necessary to explain this. For a typical HII region (Dyson and Williams 1980) an order of magnitude calculation shows that recombination times of $\sim$ months require gas densities $\sim 10^6 \mathrm{cm}^{-3}$. Assuming a gas-to-colour-excess ratio of 5×10^{21} atoms cm^{-2} mag^{-1}, normal interstellar reddening (R=3) and a distance of 500pc, then for $n_H \sim 10^6 \mathrm{cm}^{-3}$ a path length of 1 arcsec on the sky would correspond to $\approx$ 10 magnitudes of extinction in the visual. Such high obscuration is not indicated by the optical appearance of the northern fan.

2. Cohen *et al.* (1981) suggest a spectral type A5 for PV Cephei corresponding to a main sequence effective temperature of $\approx$ 8500K which is insufficient to radiatively ionise the northern fan. Since PV Cephei is most likely a T Tauri star and to the right of the mainsequence it will be even cooler.

3. The shock excitation of nebular material (by strong stellar winds) can provide an alternative source of ionising radiation. T Tauri stars are characterised by strong stellar winds and Cohen *et al.* (1981) suggest that the bright bar to the north of PV Cephei is such a region of

shock excitation. However, the disappearance of this feature between 1985 August and 1985 October implies that it results from variable illumination and is not a source of UV emission.

4. The northern fan does not have the colours of a hydrogen emission nebula, particularly, it appears bright in the I waveband.

Since it is not possible to satisfactorily interpret the northern fan as an emission nebula and since photometric and spectroscopic evidence points to a reflective origin, then an explanation of the unusually low polarisation levels, other than by an intrinsic lack of polarisation, must be sought.

It is in fact possible to reconcile these difficulties using the polarising mechanism held to be operative in the more highly polarised regions of the PV Cephei system—polarisation due to extinction by magnetically aligned grains—on the assumption of a suitable magnetic field geometry. In order to explain the low polarisation levels in the northern fan, polarisation by extinction and the underlying polarisation by scattering must combine antagonistically so that a high degree of cancellation occurs. Assuming DG alignment, such a combination may prevail if the magnetic field lines threading the nebula are essentially radial with respect to the star in contrast with the 'tangential' scattering polarisations. Although exact cancellation is unlikely the residual effects of inexact cancellation may explain the chaotic nature of the polarisation pattern observed in parts of the northern fan. The structure in the polarisation pattern of the whole PV Cephei system then results from the changing balance between polarisation by extinction and polarisation by scattering, this balance being affected by the relative orientation of the magnetic field and the radius vector to the star and by the amount of overlying dust.

6.3 Summary

The geometry proposed for the PV Cephei system is illustrated in Figure 6.7 and will now be summarised.

1. The PV Cephei system consists of a biconical nebula centred on the star which is in turn surrounded by a circumstellar disc oriented with equatorial plane perpendicular to the axis of the bicone. In the latest

image (1986 July) the PA of this axis is 355 deg. and the opening angle of the northern cone is $\approx$ 73 deg. In common with previous models, it is supposed that the bicone is inclined to the plane of the sky so that the brighter northern cone projects towards us whereas the fainter southern cone is angled into the sky and presumably therefore into the dense interior of the surrounding cloud. In addition, such a nebular tilt ensures that the equatorial disc partially overlies and obscures the southern cone creating the dark lane to the south of the star. These effects result in the colour and luminosity differences between the southern and northern cones.

2. There is substantial evidence for the presence of a circumstellar disc around PV Cephei oriented as shown in Figure 6.7 (§6.1.2). In addition it is suggested that the disc is threaded by a predominantly toroidal magnetic field component responsible for the alignment of dust grains contained within the disc (by the DG mechanism) causing the polarisation by extinction of light transmitted through this region. The result is the parallel band of vectors seen in the vicinity of PV Cephei in the polarisation maps and the large polarisation level observed for the star itself (Table 6.3). Similar features are seen in many other bipolar objects with more orthodox (*i.e.* scattering) polarisation patterns. In these objects grain alignment by a magnetic field *via* the DG mechanism has been found to provide a satisfactory explanation of the polarisation measurements (see, for example, Scarrott *et al.* 1987d). The correlation in PA between the polarisation of PV Cephei, the biconical axis, the circumstellar disc and other nebular features strongly suggests that the polarisation by extinction (and, therefore, the aligning magnetic field) is associated with the circumstellar and circumnebular material rather than with foreground cloud material which would not be expected to show such a close correlation with the nebular geometry.

3. A detailed examination of the polarisation, colour and brightness data suggests that the PV Cephei system is a highly obscured reflection nebula. In order to explain the peculiar polarisation measurements it is necessary to invoke the magnetic field geometry shown in Figure 6.7. The field lines associated with the northern cone are oriented approximately north-south but curve round smoothly in the vicinity

of PV Cephei to connect with the toroidal field in the disc. To the south of the star the nebulosity is seen through this (tilted) circumstellar disc and its embedded magnetic field. It is not possible to construct a self consistent model of the northern cone as an emission line nebula nor can the observed polarisations be produced by intrinsic polarisation of the light from PV Cephei.

There is evidence in both the imaging and polarimetric observations for a distribution of dense obscuring material around the entire PV Cephei system, probably representing the remains of the protostellar condensation out of which the star has formed. If so, then this material would be expected to share a close association with the circumstellar disc, which presumably results from the infall of such material, and may exist in the form of a disc 'halo' or envelope. There also appears to be more obscuration to the east of PV Cephei than to the west, suggesting that the circumnebular condensation is non-axisymmetric.

Neckel and Staude (1984) conclude from their spectroscopic observations that the material in the northern lobe of the PV Cephei system is "highly rarefied" in comparison with the surrounding cloud material, *i.e.* it is a relatively empty cavity situated within the dense cloud. It is thought that such cavities may be excavated within clouds by the action of energetic winds, either from the star itself or from the surrounding disc. In particular, hydromagnetically powered disc winds are expected to be intrinsically collimated (§2.3.7) and should result, therefore, in the formation of two diametrically opposed structures. The subsequent illumination of the inner walls of these cavities (by the central star or perhaps by another source) may present an elegant explanation of bipolar nebulae.
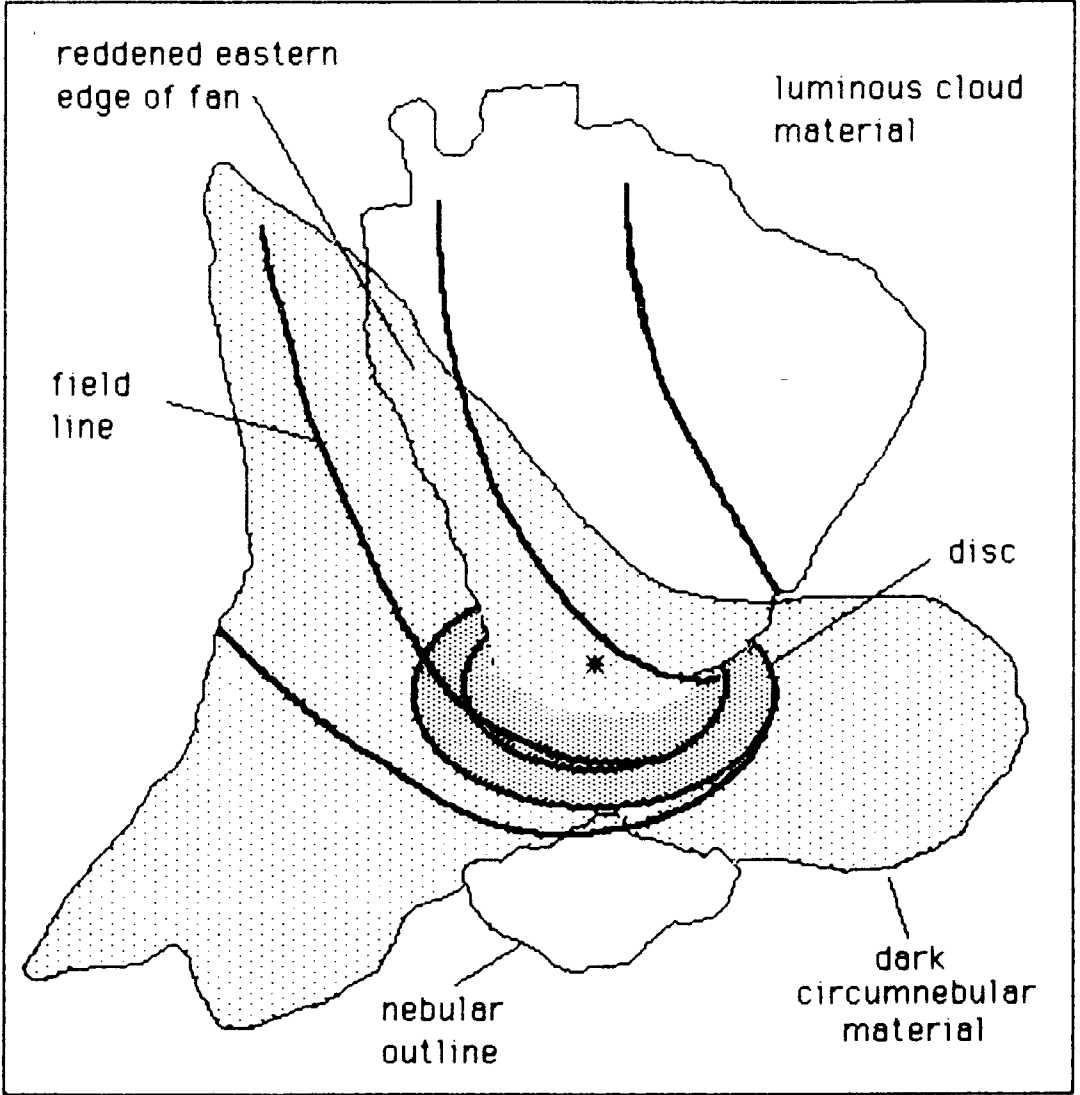
Figure 6.7: The proposed geometry for the PV Cephei system as discussed in the text.

Chapter 7

General Discussion

The previous three chapters present in some detail the polarimetric observations of candidate PMS objects and their immediate environs. Each of the sources considered is associated with some permutation of features considered typical of regions of SF (collimated optical nebulosity, collimated molecular outflow, jets, circumstellar discs *etc.*) many of which are described in chapter two. Although only three separate regions of SF are considered here, they provide quite a representative cross section of these features. In order to reach more general conclusions concerning the processes involved in the formation of stars in molecular clouds, it will be necessary to interpret the results of chapters four to six in the light of observations (both polarimetric and otherwise) of a wider sample of objects, and to discuss the implications in terms of existing theories of SF.

In the past, imaging polarimetry has been used to model reflection nebulae on the assumption of both single and multiple scattering of light originating from a central stellar source and symmetric biconical or biparaboloid geometries (*e.g.* Shirt 1984). Although such scattering geometries were originally only intended to be ideallistic, it is evident now that there are nebular systems which are too complex to allow the application of these models at all. Consider, for example, the Haro 6-5 system described in chapter four. Although a bicone centred on the star Haro 6-5B is required, to explain the polarisation of all the nebulosity contained within the boundaries of the bicone (as it appears on the plane of the sky at least) it is necessary to assume illumination by three distinct optical sources in combination with spatially variable polarisation due to extinction by aligned

grains. In other cases where only one source of illumination is required the geometry may appear more sophisticated, for example PV Cephei where asymmetry is evident in the luminous structure of the nebulosity, the distribution of circumnebular obscuring material and the polarisation pattern.

Consideration of the deviations from circular centrosymmetry of a polarisation map can provide important information on polarising processes alternative to simple scattering. In particular, polarisation by extinction due to magnetically aligned dust grains is of considerable interest in view of the correlation between high densities (extinction) and enhanced magnetic fields predicted by the cloud collapse scenarios described in chapter one. If it can be shown that grain alignment by the magnetic field *via* the DG mechanism (chapter 3) is a viable process in SF regions, then imaging polarimetry should prove a useful technique for directly investigating the field geometry in regions where alignment occurs. This is particularly important since, as well as being instrumental in the cloud collapse leading to the formation of a stellar precursor, it is becoming increasingly apparent that the cloud magnetic field should evolve with the protostar in such a way as to play a crucial role in its PMS development and, to some extent, control its interaction with the environment.

These interactions may take the form of magnetically mediated and controlled outflows of material from the circumstellar environment, which forms an important component of the hydromagnetic disc wind theories of Uchida and Shibata (1985) and Pudritz and Norman (1986b). These theories offer alternative magnetic topologies in the vicinity of the central object—in the case of Uchida and Shibata, the field near to the star is predominantly toroidal (relative to the outflow axis) whereas in the models of Pudritz and Norman the field in this region is predominantly polloidal (§2.3.7). Although the expectation of such field configurations is theoretically well grounded, whether or not they represent in reallity the conditions under which stars form is still unknown. If the magnetic field structure close to the PMS object can be determined, it should be possible to distinguish between these two disc wind theories and to further constrain future modelling.

7.1   Polarisation of the Source Regions

It has been seen in chapters four to six that the structure in the polarisation patterns close to all of the major optical sources examined (Haro 6-5A and B, HL Tau, LkHα358 and PV Cephei) is anomalous in the sense that it cannot be explained in terms of polarisation due to single scattering alone. In each case, in order to explain the deviations from circular centrosymmetry about the central source it is necessary to invoke a secondary polarising mechanism additional to single scattering.   Such additional polarisation may arise from the effects of extinction by aligned dust grains or, alternatively, from the effects of secondary or multiple scattering. In chapters four to six, discussion of the source region polarisation was oriented primarily toward the former polarising mechanism for the simple reason that it provides an interpretation of all of the observations. However, the two mechanisms will now be debated on a more equal basis.

7.1.1   The Observational Evidence

As a group, the central objects discussed in chapters 4, 5 and 6 are polarised at levels in the range 7 to 15 per cent. In each case, however, the precise manner in which the vector pattern in the surrounding nebuloisty deviates from circular centrosymmetry about the star is in some way different— particularly, the degree of curvature incorporated into the central vector pattern appears to vary between objects. In the case of PV Cephei, for example, there is very little evidence for a scattering pattern and the polarisation of the star forms part of a band of vectors of similar length and orientation covering quite an extensive region. The polarisations in the vicinity of Haro 6-5A also show a tendency to form a band of parallel orientations, although this structure is less spatially extensive. On the other hand, the polarisation patterns centred on Haro 6-5B and HL Tau are characterised by an element of curvature so as to appear 'elliptical'. This elliptical pattern is accompamied by two null points in polarisation which lie on the major axis of the ellipse (which passes through the star and is oriented parallel to its polarisation) on either side of the star and approximately equidistant from it.

Similar polarisation structure has been observed in other objects all of which show some degree of collimation of the optical nebulosity implying the

Object	Illum. Source	Optical Struc.	References
Boomerang	double star	bipolar	1,2
L1551/HH102	IRS 5	cometary[a]	3
Parsamyan 21	Apical star	cometary	4
Serpens	SVS 2	bipolar	5
Chamaeleon	IR source	bipolar	6
NGC6729	R CrA	cometary	7
NGC2261	R Mon	bipolar	8

[a]bipolar in CO.

Table 7.1: Collimated optical nebulae with anomalous source region polarisation structure.

References for Table 7.1

1. Neckel *et al.* 1987
2. Taylor and Scarrott 1980
3. Draper *et al.* 1985a
4. Draper *et al.* 1987b
5. Warren-Smith *et al.* 1987b
6. Scarrott *et al.* 1987e
7. Ward-Thompson *et al.* 1985
8. Warren-Smith *et al.* 1987a

presence of a circumstellar disc. A summary of some of these observations appears in Table 7.1. In each case a parallel band or elliptical distribution of vector orientations overlies the source region—even if the source itself is optically invisible. In addition to the observations in Table 7.1, the case of HH24 may be mentioned. In this object a band of parallel vector orientations overlies the elongated knot B region adjacent to the IR source SSV 63. However, it is not possible to say whether SSV 63 is located within this band or not since it lies at the edge of the optical nebulosity (Scarrott *et al.* 1987a).

7.1.2 Polarisation by Scattering

Aperture polarimetric observations of candidate PMS objects associated with collimated optical nebulosity and/or collimated molecular outflow reveal a tendency for the angle of polarisation to be approximately perpendicular to the axis of collimation. In the case of the spatially resolved po-

larisation maps discussed above and those listed in Table 7.1, the parallel band of vectors or the major axis of the elliptical distribution of vectors is also oriented preferentially perpendicular to the collimation axis. The two results are in most cases the same since the polarisation angle of the central object usually defines the orientation of the anomalous polarisation structure further out. Hodapp (1984) and Sato *et al.* (1985) present aperture polarimetry of sources associated with bipolar outflow at IR wavelengths and note this orthogonality between polarisation angle and collimation axis. Both authors suggest that the polarisation of the sources results from the scattering of light within anisotropic circumstellar dust shells (or discs) in the manner described by Elsässer and Staude (1978).

The asymmetrical dust distribution is necessarily located close to the star in order for the scattered light to contaminate the polarimetric aperture centred on the star. In effect the star lies at the centre of a mini-bipolar nebula which may have dimensions of a few hundred AU. The scattering geometry of Elsässer and Staude (ES) is illustrated in Figure 7.1. Most of the features of aperture polarimetry can be explained with the ES model; for example, the range in polarisation (4.6 → 22.1 per cent) of the sources within the sample of Sato *et al.* (1985) can be explained by assuming variations in the degree of circumstellar extinction causing changes in the fraction of intrinsically unpolarised direct starlight included within the aperture. Although polarisation by scattering appears to be favoured in the literature, these results can be accommodated just as easily by an aligned grain model (of the type discussed in previous chapters).

However, the results of aperture polarimetry cannot usefully constrain the nature of the polarising mechanism since the parameters associated with the dust in SF regions are not accurately known and are not necessarily the same as those derived for dust in the ISM. Hodapp (1984) shows that the IR polarisations of some objects may adequately fit a modified Serkowski curve (for instance, HL Tau) whereas others do not. But there would seem to be no reason, *a priori*, to assume that polarisation by extinction in special environments such as SF regions should follow an interstellar polarisation curve.

A more stringent requirement that must be satisfied by any polarising mechanism is the explanation of the polarisation *patterns* in the central and head regions of bipolar and cometary nebulae. Notni (1985) demonstrates how an elliptical polarisation pattern centred on a star may be produced
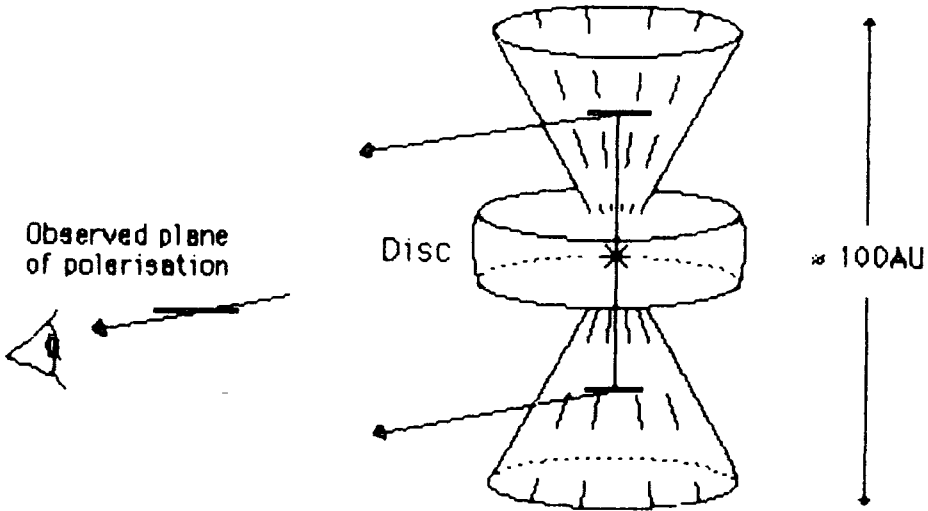
Figure 7.1: The scattering geometry of Elsässer and Staude (1978).

on the assumption of a scattering model similar to that of ES in which
the starlight is in some way 'intrinsically' polarised before scattering in the
nebular medium. However, many factors, particularly optical morphology,
require the presence of large discs of obscuring material around bipolar
and cometary nebulae, oriented with equatorial plane perpendicular to the
nebular collimation axis. The centrifugal outflow theory of Pudritz and
Norman (*e.g.* 1986) suggests disc radii of $\sim 10^{3-4}$ AU. Since light in the
ES and Notni models is assumed to be 'intrinsically' polarised close to the
star, then to proceed with this polarising mechanism within the context of
bipolar and cometary nebulae it seems necessary to assume the existence
of two obscuring discs, a big one and a small one—or to conform with pre-
existing terminology, a circumstellar and an interstellar disc. The existence
of two discs is by no means unlikely and may in some cases be necessary
(Ward-Thompson *et al.* 1985). In addition, parallel bands of polarisation
may be produced, according to Notni, in "moderately optically thick" envi-
ronments in which forward scattering angles are preferred. These bands of
parallel vector orientations are characterised by almost constant percentage
levels across the central/head regions of bipolar/cometary nebulae—for ex-

ample, PV Cephei and the Chamaeleon (Scarrott *et al.* 1987e). Although, as suggested by Notni (1985), an increase in extinction may favour more forward scattering angles (causing the circumstellar region to be polarised similarly to the star itself), the scattering must still occur within the confines of the bipolar/cometary geometry causing a range of scattering angles to be deployed and a change in the percentage levels of polarisation with angular offset from the star. The effects of illumination by an intrinsically polarised source need to be modelled in detail in order to ascertain whether or not the source region polarisation patterns observed can be explained in this way.

7.1.3 Polarisation by Aligned Grains

The most well studied occurrence of polarisation by aligned grains is the polarisation of direct starlight during transit through the interstellar medium. Under interstellar conditions the dominant grain alignment process is the Davis-Greenstein (DG) paramagnetic relaxation mechanism (discussed in chapter 3) which causes the grain major axis to be oriented perpendicular to the Galactic magnetic field resulting in a polarisation angle parallel to the field.

Optical aperture polarimetric observations of stars seen through, or embedded within, dusty (molecular) clouds associated with SF (*e.g.* Vrba *et al.* 1976, Moneti *et al.* 1985 and Cugnon 1987 for a review) suggest that polarisation by magnetically aligned grains is also operative in at least the peripheral regions of these clouds. Such a conclusion is supported by (i) the observation of polarisation levels in excess of the expected interstellar polarisation at the distance of the cloud suggesting that a component of polarisation is induced within the cloud itself; (ii) the correlation between polarisation levels and line of sight obscuration indicative of polarisation by extinction; (iii) the uniform nature of polarisation angles over large areas on the sky suggesting a spatially extensive grain aligning influence such as may be provided by the large scale magnetic field threading the cloud. The subsequent assumption of DG alignment allows a determination of the magnetic field configuration in the cloud periphery (where the majority of stars shine through) which often reveals a field orientation in accordance with the observed cloud geometry (for example, the cloud may appear flattened along the field lines in a manner consistent with the predictions of

magnetically controlled cloud collapse—§1.3.5 and also §4.5).

However, the extension of this mechanism of polarisation to the dense central regions of SF clouds and circumstellar environments must necessarily take account of the disparate nature of these regions and the ISM. In particular, the efficacy of the thermal spinning (TSA) mode of the DG alignment process is subject to the temperature constraint $T_{gra} < T_{rot}$ (chapter three) which may become a severe impediment in SF regions where gas densities are high and cooling mechanisms efficient and where grains may be heated by radiation from YSOs.

However, the applicability of TSA is becoming increasingly doubtful in regions *other* than SF molecular clouds, for example, in the ISM efficient TSA requires magnetic field strengths consistently in excess of those suggested by observation. A more effective grain aligning process is afforded by the suprathermal spinning (SSA) mode of the DG mechanism in which the ejection of hydrogen molecules from the grain surface causes the grain to rotate rapidly. The particular advantage of SSA in circumstellar environments is that the temperature constraint mentioned above is circumvented since the grain rotation is independent of the kinetic temperature of the gas. Additionally, under the assumption of SSA, the internal temperature of the grain should never exceed its rotational temperature so that the angular momentum axis of the grain will always line up parallel to the magnetic field (that is, 'inverse' DG alignment does not occur) and (assuming that the grain spins about its minor axis) the resultant polarisation angles will also be parallel to the field. However, the adoption of SSA involves the two extra assumptions mentioned in chapter 3. Firstly, there must be sufficient hydrogen present in atomic form to drive the suprathermal spin-up process, which is by no means a foregone conclusion in the interior of a 'molecular' cloud. In these situations dissipative processes such as magnetic flux slippage may ensure that there is a constant turnover of atomic hydrogen. Secondly, the timescale for grain re-surfacing must be much greater than the timescale for magnetic alignment. With these reservations in mind, SSA appears to be the most attractive grain aligning mechanism in circumstellar environments.

Assuming, then, the feasibility of SSA in these environments, the characteristic source region polarisation patterns described above may be simply explained in terms of a combination of polarisation by scattering and polarisation by extinction with no necessity for the existence of an intrin-

sically polarised source. The elliptical and parallel band vector patterns are then generated by the superposition of a constant position angle vector pattern resulting from polarisation by aligned grains and a scattering pattern circularly centrosymmetric about the illuminating source. In order to explain the observed alignments of the major axes of the elliptical patterns or the axes of the parallel vector patterns with the equatorial planes of the circumstellar discs seen in many PMS systems (or, if no disc is seen, the preferential alignment of these polarisation axes perpendicular to the outflow or nebular axis) it is necessary for the component of polarisation due to extinction to be also parallel to the plane of the discs.

The adoption of SSA immediately requires that the grain aligning magnetic field also be oriented predominantly parallel to the disc plane. The close correlation seen in many PMS systems between the polarisation pattern of the central region and the nebular morphology suggests that the deviations from circular centrosymmetry arise close to the source within the circumstellar material. Specifically, the situation is best explained if the grain aligning magnetic field lies within the circumstellar disc and exhibits a predominantly toroidal configuration with respect to the nebular or outflow axis. Such toroidal field geometries may result during the anisotropic collapse of clouds with significant angular momentum (§1.3.6).

Variations in the precise manner in which the central polarisation patterns deviate from circular centrosymmetry may be attributed to the changing level of competition between polarisation by aligned grains and polarisation by scattering. This level of competition will in turn be influenced by such factors as the line of sight extinction to the object, the nebular geometry—particularly the extent of the circumstellar disc and its magnetic field, the degree of nebular tilt and the parameters affecting the polarising ability of the grains and the extent to which they are aligned. Where a parallel band of polarisation vectors is seen, the effects of polarisation by extinction dominate whereas in the case of an elliptical distribution of vector orientations, an element of curvature due to the underlying scattering pattern is perceived. The existence of null points in some polarisation patterns is a natural consequence of this competition in which the polarising mechanisms combine most antagonistically along a line parallel to the equatorial plane of the disc and its entrapped grain aligning magnetic field.

7.2 Scattering or Aligned Grains?

In previous chapters, the source region polarisation patterns have been interpreted in terms of a combination of polarisation by aligned grains and polarisation by single scattering, in the manner described above, since this mechanism can provide a simple explanation for all of the observed polarisation features given a suitable magnetic field geometry. The same cannot be said however, of the pure scattering mechanism described in §7.1.2 which, although it may adequately generate elliptical vector patterns, could not be responsible for the polarisation pattern seen in the PV Cephei system where very little evidence for scattering exists. Indeed, the polarisation pattern in the majority of the PV Cephei system is what might be expected if the underlying scattering pattern was 'turned off' to reveal the distribution of obscuring material and the topology of the overlying grain aligning magnetic field. This object shows strong evidence for the existence of a toroidal magnetic field component within the circumstellar material. However, even if the existence of toroidal magnetic fields within circumstellar discs is generalised to include all PMS objects, this still does not obviate a contribution to the polarisation by scattering from a polarised source.

In the Serpens nebula it seems probable that the optical condensation identified with the central IR source SVS2 is, in fact, a region of intense scattering with the star itself remaining optically invisible (Warren-Smith *et al.* 1987b). If such is the case, then it is likely that a significant portion of the Serpens nebula may be illuminated by an 'intrinsically polarised' source—an effect that should increase with polar angle from the nebular axis. However, within the same object there is strong evidence for the existence of spiral irregularities in the polarisation pattern of both the inner and outer nebular regions (again, Warren-Smith *et al.* 1987b). Such polarisation structure cannot be reconciled with scattering alone but can be accommodated by an aligned grain model on the assumption of an appropriate (spiral) magnetic field geometry. A similar effect is observed in the northern lobe of the nebulosity associated with R Mon (NGC2261) wherein subtle deviations from a circularly centrosymmetric vector pattern betray the presence of aligned grains and suggest a field configuration with helical symmetry (Warren-Smith *et al.* 1987a). Effects such as these, in which the polarisation pattern appears distorted and in a manner which is asymmetric, cannot be explained by scattering from an intrinsically polarised source

(which should lead to symmetry about the polar axis).

Temporal variations in the polarisation levels and angles of PMS objects such as T Tauri stars and young IR sources are quite well known. In principle, variations in polarisation level can be explained in terms of changes in the line of sight obscuration which may arise from the bulk motion of clumpy material close to the star. It is more difficult to account for changes in the polarisation angle, however, since it is unlikely that grain re-alignment can occur on such short timescales ($\sim$ years). Magnetically aligned grains within precessing discs offer a possible solution close to the star provided that the dynamical timescales are short enough. Where variations in polarisation are accompanied by and correlated with fluctuations in the brightness of an object or where changes in the polarisation angle of the source are correlated with changes in polarisation angle further out in the disc or nebula, then an interpretation of the polarisation in terms of scattering is favourable (§7.1.2). In addition, the polarisation reversals exhibited by some stars (changes in the polarisation angle of 90 deg. at certain wavelengths) are best interpreted in terms of scattering (Bastien 1987).

It seems likely, therefore, that in order to satisfactorily interpret the complete range of polarimetric observations, both polarising mechanisms (scattering from a polarised source and extinction by aligned grains) will be required. The same conclusion is reached by Bastien (1987) and by Heckert and Zeilick (1985) who suggest that the relative importance of the two polarising mechanisms should be determined for each object on an individual basis.

7.3 Models Involving Magnetic Fields

The importance of the magnetic field at various stages in the dynamic evolution of a SF molecular cloud was briefly reviewed in chapter 1. Particularly, the flux to mass ratio in the diffuse ($\sim 10^3 cm^{-3}$) initial pre-collapse phase is a critical factor in determining whether or not a cloud is unstable to gravitational contraction (§1.3.3). Once contraction ensues, its progress is likely to be regulated by the process of magnetic braking (§1.3.5) by which angular momentum is transported outwards from the central condensing regions into the surrounding cloud material. As long as the flux-freezing

assumption holds then the magnetic field will continue to be influential in the development of any protostellar condensations.

In dense cloud cores, the magnetic field may begin to decouple from the neutral mass at densities as low as $10^6 cm^{-3}$ (Mouschovias *et al.* 1985) which is of the same order of magnitude as the gas density obtained by Kaifu *et al.* (1984) for the molecular disc around L1551 IRS5. It seems necessary that the flux-freezing assumption must break down at some point during the collapse of the central dense region of the cloud in order to allow the formation of condensations with stellar densities but without the enormous magnetic fields predicted by a constant mass to flux ratio (the so called 'magnetic flux problem'). In addition, magnetic fields appear to inhibit the formation and growth of fragments (Phillips 1986) whereas the majority of stars seem to be associated with binary or multiple systems.

On a simplistic level, it seems likely that there will exist a volume of space in the densest region of the contracting cloud within which the bulk of the material will be free to evolve independently of the magnetic field. The size of this region will depend upon the range in density over which the field is able to effectively decouple from the neutrals. The material within the volume is fated to become part of a protostellar object and, if magnetic braking has been particularly efficient in the previous stages of cloud contraction, it may collapse in approximate free fall to form a slowly rotating star. A range of angular momenta at the point at which the field decouples from the neutral material, resulting from the varying efficiency of magnetic braking in different collapse situations, may be the cause behind the range of angular velocities seen in stars and stellar systems. If a significant amount of angular momentum is present at the onset of the non-magnetic central collapse, then the resulting protostar, as well as spinning rapidly, may be surrounded by a rotating (centrifugally supported) disc of accreting material.

If we assume that, outside the decoupled volume, the neutral material is still essentially well coupled to the field then, during the formation of the central protostar, magnetic braking should continue to operate in these regions resulting in a condensed circumstellar environment. The presence of the frozen-in magnetic field means that the contraction will be anisotropic producing a massive magnetised disc (much larger than the centrifugally supported central disc mentioned above). Even if this assumption is not well founded, a magnetised circumstellar disc may still be expected to occur for

the following reasons; (i) Once the central star forms and hydrogen fusion begins, the ionisation fraction of the surrounding material will rise and any field present will again be locked into the majority neutral material; (ii) During any temporary decoupled phase, although neutral material is relatively free to move inwards across the field lines under the force of self-gravitation, a loss or exclusion of magnetic flux from the central regions of the cloud will not necessarily occur so that a significant field component may be retained in the 'remnant' material after the formation of the star.

These considerations allow the formation of two circumstellar discs—a small inner one and a large outer one. If this is the case, then both of the polarising mechanisms discussed in the previous sections may be accommodated within the same system.

- The inner disc is expected to be in approximate centrifugal equilibrium having decoupled from the cloud field during the protostellar stage although it may at some point become associated with the magnetic field generated by the central object. The collimation of starlight by the inner disc may result in the production of an 'intrinsically' polarised source if it has dimensions of ≈ 100 AU or less and is, therefore, unresolved at optical wavelengths. The material in this central disc may eventually form planets or fall onto the star. Alternatively, it could be dispersed by an energetic stellar wind. In addition, an inner disc may be associated with highly collimated outflow structures such as the optical jet observed in the HH34 region.

- The large outer disc carries most of the mass and angular momentum of the system and is expected to remain strongly coupled to the cloud field. This large magnetised disc may be responsible for the polarisation by extinction of starlight passing through it, in which case the threading magnetic field must have a predominantly toroidal configuration in order to reproduce the observations. In addition, the molecular outflows to be discussed in the next section are expected to be associated with this structure.

It is not clear how the process of fragmentation fits into this scheme although it may have something to do with the amount of angular momentum present when the inner cloud regions collapse to form the protostar (for example, instead of an inner disc occurring around the protostar, a satelite object may form instead).

7.4 Implications for Outflow Acceleration

The scenario outlined above suggests the formation of a star surrounded by a disc of predominantly molecular material which will be threaded by and coupled to the central part of the magnetic field that has evolved with the contracting cloud. These are the conditions under which the hydro-magnetically accelerated molecular outflows of Pudritz and Norman (1986) and Uchida and Shibata (1985) are expected to occur. However, the efficacy of these acceleration mechanisms depends to a large extent of the geometry of the magnetic field as it leaves the circumstellar disc regions and this in turn will be determined by the way in which the cloud has collapsed—particularly, the degree of magnetic braking that has occurred.

The results of imaging polarimetry suggest that (at least some) circumstellar discs contain a grain-aligning magnetic field with an approximately toroidal (with respect to the disc polar axis) geometry. Such a conclusion seems necessary in order to explain the source region polarisation pattern in the PV Cephei system. A way in which a central toroidal magnetic field can be generated was outlined in §2.3.7.1 and involves the twisting of field lines by the differential rotation of a circumstellar disc. This process should be generally applicable and suggests that toroidal fields resulting from the rotational winding of field lines may be a natural consequence of the evolution of a magnetised rotating circumstellar disc.

The acceleration models of Uchida and Shibata (1985) suggest that the large scale molecular mass outflows seen in many regions of SF (and reviewed in §2.3) can be driven by the induction of a toroidal field component within a rotating molecular disc. Relaxation of the twisted field lines converts angular momentum in the disc to linear momentum in the outflow, thus braking the disc in the process. However, the model calculations begin at a point where the disc is assumed to be threaded by a purely polloidal field ($B_\phi = 0$) and so fail to take account of any previous evolution of the cloud which may lead to a B_ϕ component within the disc. In addition, the models assume axisymmetry ($\partial/\partial\phi = 0$) which is bound to be an over-simplification. For example, in the case of the PV Cephei system (chapter 6) there is strong evidence to suggest that the distribution of circumstellar and circumnebular material is non-axisymmetric with a greater accumulation of obscuration to the east of the star than to the west. If we assume that the local magnetic field is closely associated with this material

(and perhaps partly responsible for its distribution) then it too is likely to be non-axisymmetric. The detection of spiral structure in the density and magnetic field distributions in the Serpens nebula (Warren-Smith *et al.* 1987b) provides further evidence of non-axisymmetry.

The assumption of axisymmetry is also inherent in the centrifugal acceleration mechanism of Pudritz and Norman (1986) wherein the field threading the disc is predominantly polloidal and rigid body (disc) rotation is normally assumed. The efficiency of centrifugal acceleration depends to a large extent upon the geometry of the field as it leaves the disc surface or envelope. If the field in these regions is inclined to the plane of the disc *i.e.* if it has a polloidal component then centrifugal acceleration is possible. A transition between toroidal and polloidal field geometries in the vicinity of a circumstellar disc features in the model proposed for the PV Cephei system (Figure 6.7) and in this situation it is possible that both centrifugal acceleration and magnetic twist acceleration can operate simultaneously.

Pudritz and Silk (1987) model the evolution of rotating magnetised 'pancakes' in axisymmetric geometries and note that the build up of a toroidal field component is opposed by the effects of ambipolar diffusion with the ratio B_ϕ/B_z never exceeding unity in their calculations. However, these conclusions may not be significant in situations in which the angular momentum and local magnetic field axes are inclined. In such 'obliquely' rotating systems toroidal field components may develop more readily in the circumstellar region. In addition, if the condition that the disc is self-gravitating is relaxed then it may be considered likely that in the presence of ambipolar diffusion there will exist a central keplerian portion of the disc within which rotational wind up of the field lines may occur. Beckwith and Sargent (1987) find evidence for a keplerian velocity curve in the case of the disc around HL Tau.

In any case, a departure from axisymmetry (in which the rotation axis is aligned with the large scale magnetic field) in outflow acceleration and cloud collapse models seems necessary if the non-axisymmetric field and density distributions observed in some circumstellar environments are to be explained. In particular, the processes of cloud collapse, magnetic braking and magnetic acceleration need to be studied in situations were the angular momentum axis of the system is inclined relative to the magnetic field. It has been shown that magnetic braking is more efficient in the case of a perpendicular rotator than a parallel one (Dorfi 1982) leading to heav-

ier damping of the perpendicular component of angular momentum and, hence, a gradual alignment of the rotation axis with the magnetic field. This argument has sometimes been used to justify the selection of models in which the rotation/outflow axis is exactly parallel with the local field (hence considerably simplifying the model) but in reality it is more likely that a dispersion of outflow orientations will exist (perhaps centred about parallelism with the field). The hydromagnetic acceleration mechanisms are most efficient when the rotation axis is aligned with the field (axisymmetry as normally assumed) and in cases where the rotation axis lies perpendicular to the field it is difficult to envisage how any outflow acceleration could occur at all. A distribution of field-rotation axis inclinations may go some way, therefore, to explaining the observed diversity of molecular outflow parameters such as velocity and degree of collimation (the latter of which cannot be explained in terms of geometry alone—§2.3.3).

In addition, CO observations of bipolar molecular outflows suggest that, in general, the major axes of the outflows are significantly inclined to the local magnetic field. Table 7.2 lists the projected (onto the plane of the sky) PAs of the major axes of several bipolar molecular outflows (and collimated optical nebulosities) and the local magnetic field (as determined by interstellar polarisation measurements). These results are displayed in Figure 7.2 which clearly shows a clustering of outflows around the local magnetic field direction. With the exception of GL 490, all of the outflows are oriented within 40 deg. of the magnetic field suggesting that it has been influential in their formation (although the errors on some of the measurements are quite large). However, after taking the errors into account, the orientations of nine of the fifteen outflows deviate significantly from parallelism with the field emphasising the importance of considering oblique rotation.

Object	PA^b_{flow} (deg.)	PA^c_{field} (deg.)	$\vert PA_{flow}\text{-}PA_{field}\vert$
Cep A	102 ± 5	86 ± 17	16 ± 18
DG Tau[a]	226 ± 2^1	45 ± 5^5	1 ± 5
GGD 12-15	137 ± 5	170 ± 20	33 ± 21
GL 490	35 ± 5	116 ± 7	81 ± 9
GL 961	145 ± 5	170 ± 20	25 ± 21
GL 2591	45 ± 20^2	40 ± 31	5 ± 37
H6-5A[a]	355 ± 1^3	23 ± 5^6	28 ± 7
H6-5B[a]	53 ± 6^3	23 ± 5^6	30 ± 7
HH7-11	142 ± 5^4	147 ± 9^7	5 ± 10
HL Tau	56 ± 3^3	75 ± 5^8	19 ± 7
L1551	62 ± 5	75 ± 5^8	13 ± 7
Mon R2	134 ± 5	170 ± 20	36 ± 21
Orion KL	128 ± 5	109 ± 22	19 ± 23
R Mon	177 ± 5	170 ± 20	7 ± 21
S106	20 ± 4	58 ± 9	38 ± 10

a Optical nebulosity rather than molecular outflow

b From Cohen *et al.* 1984 (with a token error of ± 5 deg. added) unless otherwise annotated

c From Dyck & Lonsdale 1979 unless otherwise annotated

Table 7.2: Projected PAs of the major axes of 12 bipolar molecular outflows and 3 collimated optical nebulosities and their local magnetic fields.

References for Table 7.2

1. Mundt *et al.* 1987

2. Measured from Lada *et al.* 1984—axis indis¢tinct

3. This work

4. Hodapp 1984

5. Moneti *et al.* 1984

6. Vrba *et al.* 1985

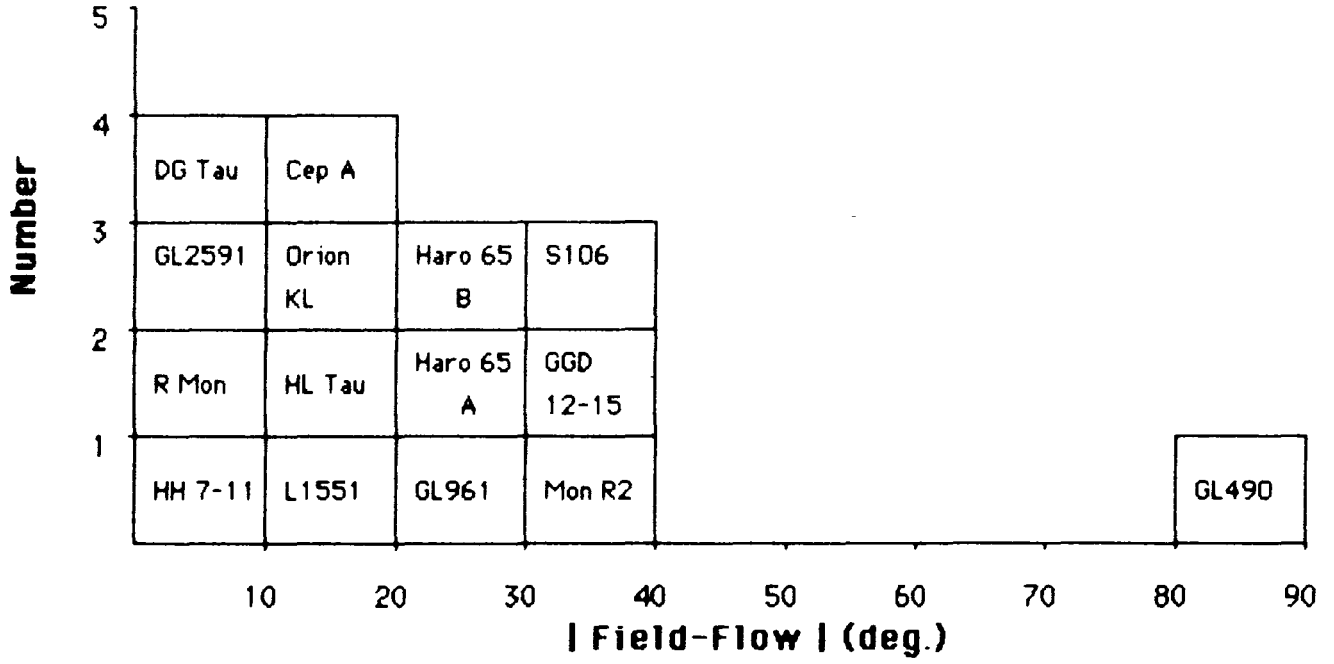7. Turnshek *et al.* 1980

8. See §5.2.2

Figure 7.2: The distribution of 15 outflow orientations with respect to the local magnetic field direction.

Concluding Remarks

There is evidence for bipolar structure in each of the three SF regions considered although in each case the nebulosity is in some way morphologically unique. Optical polarimetry has been used to determine the illuminating sources in each system.

- The reflection nebulosity surrounding Haro 6-5B has been interpreted in terms of a straight edged bicone centred about this star. The nebulosity to the north-east of the star appears to outline the edges of one cone whereas the 'counterlobe' structure lies within the bounds of the south-west projecting cone. Haro 6-5A (FS Tau) also illuminates nebulosity, however, this nebulosity does not appear to have a well determined geometry. In addition to these two stars, a further centre of illumination exists in the Haro 6-5 system (Haro 6-5C) and may result from the intense scattering of light originating from Haro 6-5B by circumstellar or circumnebular material.

- A bipolar configuration has been suggested for the reflection nebulosity surrounding the star HL Tau although the geometry is less well defined than in the case of Haro 6-5B. The nearby star LkHα358 also appears to be associated with bipolar nebulosity.

- PV Cephei illuminates a well defined bipolar nebula whose edges appear curved rather than straight as in the case of Haro 6-5B. The optical structure of this nebulosity has varied dramatically and continuously throughout the period of the observations presented. Changes can occur on timescales of $\sim$months.

The ubiquity of dense obscuring discs of gas and dust in systems exhibiting bipolarity is becoming evident. These discs play central roles in both the theoretical attempts to explain the collimation and acceleration of bipolar flows and in the explanation of unusual source region polarisation patterns.

- In the Haro 6-5 system there is strong evidence for the existence of discs of obscuration around both Haro 6-5A and Haro 6-5B. The

Haro 6-5B disc is probably responsible for the collimation of the optical bicone, the disc equatorial plane being oriented perpendicular to the biconical axis. The polarimetric observations support previous suggestions of discs around the PMS stars HL Tau and PV Cephei—in each case the disc plane lies approximately perpendicular to the collimation axis.

Speculation on the nature of bipolar nebulae can only be useful within a larger context encompassing other forms of bipolarity, particularly the large scale molecular outflows associated with many PMS sytems (§2.3). Theoretical interpretation of molecular outflow appears to be converging under the weight of evidence towards the hydromagnetic disc wind theories described in §2.3.7. In particular, the magnetic twist acceleration model of Uchida and Shibata predicts the accumulation of a significant magnetic field component in the plane of a circumstellar disc.

- The existence of such toroidal magnetic field configurations can account for the polarimetric observations described in chapters 4, 5 and 6 and the assumptions and implications are discussed in chapter 7. An alternative interpretation of some (but not all) of the source region polarimetry is available in the form of illumination by an intrinsically polarised source. In order to interpret the wider body of polarimetric evidence it is necessary to assume that illumination by intrinsically polarised sources and polarisation by magnetically aligned grains are both viable processes. Each object must be considered on an individual basis in order to assess the relative importance of these processes.

- The hydromagnetic acceleration models predict the establishment of disc outflows which have cylindrical geometries and are concentrated into shells surrounding relatively hollow cavities. The illumination of the inner walls of these cavities by a centrally located source would provide a simple and natural explanation of the bipolar nebulae observed, assuming that the outflow contains dust—presumably swept up from the disc material.

- Of the three regions considered, only the PV Cephei system exhibits a bipolar molecular outflow although blue shifted CO emission exists to the north-east of HL Tau.

Imaging polarimetry is an ideal tool for investigating the nature of the magnetic field in the region surrounding an accreting protostellar object as long as the effects of scattering (single or otherwise) can be distinguished. Current theoretical models of cloud collapse and outflow acceleration envisage axisymmetric magnetic field distributions, usually with the angular momentum axis aligned with the parental cloud field direction and must therefore represent idealisation.

- The axes of the nebulosity in both the Haro 6-5 and HL Tau systems are significantly inclined to the local magnetic field as determined by polarisation measurements of background stars. This indicates that oblique rotation may have been important in these regions at the cloud collapse stage (§7.4).

The observation of field geometries around regions of collimated nebulosity is of great value and needs to be extended. Deep CCD imaging has already shown that, in some systems, dark matter associated with a disc forms part of a more spatially extensive structure. These structures may be seen in silhouette against any background luminosity and can extend quite a way out from the central disc regions. The mapping of the polarisation in these regions should prove useful in determining the way in which the cloud magnetic field connects with the disc and how it is oriented relative to the axis of symmetry.

- The imaging polarimetric observations of the PV Cephei system reveal a non-axisymmetric distribution of matter and magnetic field around the star. It is expected that this material represents the remnant protostellar material out of which the star has formed and that it is closely associated with the more symmetric central disc.

Deep CCD polarimetry of other bipolar outflow regions promises to reveal circumstellar discs as but the central, dense, symmetric components of more extensive and irregular accretion complexes. Observational determination of the density and magnetic field distributions is necessary in order to accurately constrain and check the theoretical models. Without such constraint models concerned with hydromagnetic acceleration, magnetic braking and cloud collapse may become unrealistic.

Both the Haro 6-5 and HL/XZ Tau systems contain linear emission line features that have previously been interpreted as 'jets' of material emanating from identified PMS sources in the area. An alternative explanation is provided by Cantò *et al.* (1986) who suggest that the observed emission line structures may result from the thermalisation of a stellar wind by the walls of an ovoid cavity. In any case it seems likely that the emission line radiations are generated by recombination behind weak shock fronts (in common with HH object spectra) and typically they show red and blue shifts $\sim 100 \mathrm{km\ s^{-1}}$. These factors can be accommodated by both models (in the jet model the shocks may result from succesive compression and rarefaction of the highly collimated jet material as it passes through the ambient cloud) although in individual cases the optical morphology may favour one or the other.

In the Haro 6-5 system the jet appears to curve away from the most likely exciting source, Haro 6-5B. If this feature is indeed a jet emanating from this source then it must undergo a considerable deflection close to the star. Alternatively if the 'jet' results from the interaction of an energetic (but not highly collimated) outflow from Haro 6-5B (or some other source) with the wall of an excavated cavity or perhaps with the edge of a particularly dense cloud region then the shape of the jet will be determined by the geometry of the interaction. However, it is then necessary to explain why the brightest part of the jet in the optical lies on the axis defined by the proposed Haro 6-5B bicone and disc.

Similar arguments apply in the case of the jet in the HL Tau system which lies close the axis defined by the disc around HL Tau but appears to curve away from this star. The mechanism by which these jet like features are produced and their exact points of origin clearly remains uncertain.

The streak feature intermittently visible in the PV Cephei system is best interpreted in terms of the transient illumination of a cavity wall.

Abbrieviations

DG .... Davis-Greenstein
ES .... Elsässer-Staude
HH .... Herbig-Haro
ISM .... Interstellar Medium
PA .... Position Angle
PMS .... Pre-mainsequence
SF .... Star Formation/Star Forming
SSA .... Suprathermal Spinning Alignment
TSA .... Thermal Spinning Alignment
YSO .... Young Stellar Object

Acknowledgements

References

Journal abbrieviations:

A.A. .... Astronomy and Astrophysics
A.J. .... Astronomical Journal
Ap. J.................................Astrophysical Journal
A.R.A.A. ....Annual Review of Astronomy and Astrophysics
M.N.R.A.S. .... Monthly Notices of the R.A.S.
P.A.S.J. .... Publications of the Astronomical Society of Japan
P.A.S.P. .... Publications of the Astronomical Society of the Pacific

Aannestad, P. & Greenberg, J.M. 1983 Ap. J. **272** 551

Bally, J. & Lada, C.J. 1983 Ap. J. **265** 824

Bania, T.M. 1977 Ap. J. **216** 381

Bastian, U. & Mundt, R. 1985 A.A. **144** 57

Bastien, D. & Landstreet, J.D. 1979 Ap. J. **229** L137

Bastien, P. 1982 A.A. Suppl. **48** 153

Bastien, P. 1987 Ap. J. **317** 231

Beckwith, S., Zuckerman, B., Skrutskie, M.F. & Dyck, H.M. 1984
        Ap. J. **287** 793

Beckwith, S. & Sargent, A. 1987 I.A.U. Symp. No. 122
'Circumstellar Matter' p81

Beiging, J.H., Cohen, M. & Schwartz, P.R. 1984 Ap. J. **282** 699

Bhat, C.L., Mayer, C.J. & Wolfendale, A.W. 1986
        Phil. Trans. R. Soc. Lond. A **319** 249

Bhat, C.L., Issa, M.R., Houston, B.P., Mayer, C.J. & Wolfendale, A.W.
        1985 *Nature* **314** 511

Blandford, R.D. & Payne, D.G. 1983 M.N.R.A.S. **199** 883

Blitz, L. & Shu, F.H. 1980 Ap. J. **238** 148

Bodenheimer, P. I.A.U. 1980 Symp. No. 93 *'Fundamental Problems
        in the Theory of Stellar Evolution'* 5

Böhm, K.-H., Böhm-Vitense, E. & Brugel, E.W. 1981
        Ap. J. **245** L153

Boss, A.P. 1987 Ap. J. **316** 721

Brown, A., Mundt, R., & Drake, S.A. 1985 *'Radio Stars'* p105

Burton, W.B. & Gordon, M.A. 1978 A.A. **63** 7

Calvet, N., Cantò, J. & Rodriguez, L.F. 1983 Ap. J. **268** 739

Cantò, J. 1980 A.A. **86** 327

Cantò, J. & Rodriguez, L.F. 1980 Ap. J. **239** 982

Cantò, J. 1981 *'Investigating the Universe'* p95

Cantò, J. Rodriguez, L.F., Barral, J.F. & Carral, P. 1981
       Ap. J. **244** 102

Cantò, J. 1983 *Revista Mexicana de Astronomia y Astrofisica*
       7 109

Cantò, J., Sarmiento, A. & Rodriguez, L.F. 1986 *Revista*
       Mexicana de Astronomia y Astrofisica **13** 107

Chan, K.L., & Henricksen, R.N. 1980 Ap. J. **241** 534

Clark, F.O. & Laureijs, R.J. 1986 A.A. **154** L26

Cohen, M. & Kuhi, L.V. 1976 Ap. J. **210** 365

Cohen, M., Kuhi, L.V. & Harlan, E.A. 1977 Ap. J. (letters) **215** L127

Cohen, M. & Kuhi, L.V. 1979 Ap. J. Supp. **41** 743

Cohen, M., Kuhi, L.V., Harlan, E.A. & Spinrad, H.
       1981 Ap. J. **245** 920

Cohen, M., 1983 Ap. J. (letters) **270** L69

Cohen, M., Harvey, P.M. & Schwartz, R.D. 1985 Ap. J. **296** 633

Cohen, M. & Jones, B.F. 1987 Ap. J. **321** 846

Cohen, R.J., Rowland, P.R. & Blair, M.M. 1984 M.N.R.A.S. **210** 425

Cohen, R.S., Cong, H.I., Dame, T.M., & Thaddeus, P. 1980
       Ap. J. (letters) **239** L53

Cudworth, K.M. & Herbig, G. 1979 A.J. **84/4** 548

Cugnon, P. 1987 *'Interstellar Magnetic Fields'* eds. Beck, R. &
       Gräve, R. p100

Davis, L. & Greenstein, J.L. 1951 Ap. J. **114** 206

Dopita, M.A., Binette, L. & Schwartz, R.D. 1982 Ap. J. **261** 183

Dopita, M.A., Caganoff, S., Schwartz, R.D. & Cohen, M 1987
       I.A.U. Symp. No. 115 *'Star Forming Regions'* p346

Dorfi, E. 1982 A.A. **114** 151

Draine, B.T., Roberge, W.G. & Delgrano, A. 1983 Ap. J. **264** 485

Draper, P.W., Warren-Smith, R.F. & Scarrott, S.M. 1985a
       M.N.R.A.S. **216** 7p

Draper, P.W., Warren-Smith, R.F. & Scarrott, S.M. 1985b

M.N.R.A.S. **212** 1p

Draper, P.W. 1987 Ph. D. Thesis, Univ. of Durham

Dyck, H.M. & Lonsdale, C.J. 1979 A.J. **84/9** 1339

Dyson, J.E. & Williams, D.A. 1980 *'The Physics of the Interstellar Medium'*

Edwards, S. & Snell, R.S. 1984 Ap. J. **281** 237

Edwards, S., Strom, S.E., Snell, R.L., Jarrett, T.H., Beichman, C.A. & Strom, K.M. 1986 Ap. J. **307** L65

Elias, J.H. 1978 Ap. J. **224** 857

Elmegreen, B.G. 1987 I.A.U. Symp. No. 115 *'Star Forming Regions'* p457

Elmegreen, B.G. & Elmegreen, D.M. 1986 Ap. J. **311** 554

Elsässer, H. & Staude, H.J. 1978 A.A. **70** L3

Falgarone, E. & Puget, J.L. 1986 A.A. **162** 235

Fischer, J., Sanders, D.B., Simon, M. & Solomon, P.M. 1985 Ap. J. **293** 508

Gledhill, T.M., Warren-Smith, R.F. & Scarrott, S.M. 1986 M.N.R.A.S. **223** 867

Gledhill, T.M., Warren-Smith, R.F. & Scarrott, S.M. 1987 M.N.R.A.S. in press

Goldreich, P. & Kwan, J. 1974 Ap. J. **189** 441

Goldsmith, P.F., Snell, R.L., Hemeon-Heyer, M. & Langer, W.D. 1984 Ap. J. **286** 599

Greenberg, J.M. 1978 in *'Cosmic Dust'*

Gyulbudaghian, A.L., Magakian, T.Yu. & Amirkhanian, A.S. 1977 Akad. Nauk. SSR. **3** No. 4 162

Haro, G. 1952 Ap. J. **115** 572

Haro, G. 1953 Ap. J. **117** 73

Hartigan, P., Mundt, R. & Stocke, J. 1984 A.J. **91** 1357

Hayashi, S.S, Hayashi, M., Uchida, Y., Kaifu, N., Hasegawa, T. & Shibata, K. 1987 I.A.U. Symp. No. 115 *'Star Forming Regions'* p348

Hecht, E. 1987 *'Optics'* 2nd Ed.

Heckert, P.A. & Zeilick, M. 1985 A.J. **90** 2291

Herbig, G.H. 1951 Ap. J. **113** 697

Herbig, G.H. 1977 Ap. J. **217** 693

Herbig, G.H. 1985 *'Birth and Infancy of Stars'* p535

Heyer, M.H., Vrba, F.J., Snell, R.L., Schloerb, F.P., Strom, S.E.,
    Goldsmith, P.F. & Strom, K.M. 1987a Ap. J. **321** 855
Heyer, M.H., Snell, R.L. & Goldsmith, P.F. 1987b Ap. J. **321** 370
Hodapp, K.-W. 1984 A.A. **141** 255
Hoyle, F. 1953 Ap. J. **118** 513
Hulst, H.C. van de, 1957 *'Light Scattering by Small Particles'*
Johnson, P.E. 1982 *Nature* **295** 371
Kaifu, N., Suzuki, S., Hasegawa, T., Morimoto, M., Inatane, J., Nagane, K.,
    Miyazawa, K., Chikada, Y., Kanzawa, T. & Akabane, K. 1984
    A.A. **134** 7
Kaifu, N. 1987 I.A.U. Symp. No. 115 *'Star Forming Regions'* p275
Königl, A. 1982 Ap. J. **261** 115
Kuhi, L.V. 1978 *'Protostars and Planets'* I p708
Kwan, J. & Scoville, N.Z. 1976 Ap. J. (letters) **210** L39
Kwan, J. 1979 Ap. J. **229** 567
Kwan, J. & Valdes, F. 1983 Ap. J. **271** 604
Lada, C.J. 1980 *'Giant Molecular Clouds in the Galaxy'* p239
Lada, C.J., Thronson, H.A., Smith, H.A., Schwartz, P.R. & Glaccum, W.
    1984 Ap. J. **286** 302
Lada, C.J. 1985 A.R.A.A. **23** 267
Larson, R.B. 1978 M.N.R.A.S. **184** 69
Larson, R.B. 1986 M.N.R.A.S. **218** 409
Levreault, R.M. 1984 Ap. J. **277** 634
Levreault, R.M. & Opal, C.B. 1987 A.J. **93** 669
Lo, K.Y., Ball, R., Masson, C.R., Phillips, T.G., Scott, S. & Woody, D.P.
    1987 Ap. J. (letters) **317** L63
Margulis, M. & Lada, C.J. 1985 Ap. J. **299** 925
Mestel, L. & Paris, R.B. 1984 A.A. **136** 98
    'Star Formation' ?
Michel, F.C. 1969 Ap. J. **158** 727
Mirabel, I.F. 1987 I.A.U. Symp. No. 115 *'Star Forming Regions'* p315
Moneti, A., Pipher, J.L., Helfer, H.L., McMillan, R.S. & Perry, M.L.
    1984 Ap. J. **282** 508
Moriarty-Schieven, G.H., Snell, R.L. & Strom, S.E. 1987
    Ap. J. (letters) **317** L95
Morrish, A.H. 1965 *'The Physical Principles of Magnetism'* p87
Moushovias, T.Ch. , Shu, F.H. & Woodward, P. 1974 A.A. **33** 73

Moushovias, T.Ch. 1976a Ap. J. **206** 753

Moushovias, T.Ch. 1976b Ap. J. **207** 141

Moushovias, T.Ch. 1980 I.A.U. Symp. No. 93 *'Fundamental Problems in the Theory of Stellar Evolution'* 41

Moushovias, T.Ch. , Paleologou, E.V. & Fiedler, R.A.
1985 Ap. J. **291** 772

Mundt, R. & Giampapa, M.S. 1982 Ap. J. **256** 156

Mundt, R. & Fried, J.W. 1983 Ap. J. (letters) **274** L83

Mundt, R. & Witt, A.N. 1983 Ap. J. **270** L59

Mundt, R., Bührke, T., Fried, J.W., Neckel, T., Sarcander, M.
& Stocke, J. 1984 A.A. **140** 17

Mundt, R., Brugel, E.W. & Bührke, T. 1987 Ap. J. **319** 275

Mundt, R. 1987 I.A.U. Symp. No. 122 *'Circumstellar Matter'* p147

Neckel, T. & Staude, H.J. 1984 A.A. **131** 200

Neckel, T., Staude, H.J., Sarcander, M. & Birkle, K. 1987
A.A. **175** 231

Norman, C. & Silk, J. 1979 Ap. J. **228** 197

Norman, C. & Silk, J. 1980 Ap. J. **238** 158

Notni, P. 1985 Astron. Nachr. **306** 265

Ortolani, S. & D'Odorico, S. 1980 A.A. **83** L8

Osterbrock, D.E. 1958 P.A.S.P. **70** 399

Phillips, G.J. 1986 M.N.R.A.S. **221** 571

Pudritz, R.E. 1985 Ap. J. **293** 216

Pudritz, R.E. & Norman, C.A. 1983 Ap. J. **274** 677

Pudritz, R.E. & Norman, C.A. 1986a Ap. J. **301** 571

Pudritz, R.E. & Norman, C.A. 1986b Can. J.Phys. **64** 501

Pudritz, R.E. & Silk, J. 1987 Ap. J. **316** 213

Purcell, E.M. 1979 Ap. J. **231** 404

Rieke, G.H. & Lebofsky, M.J. 1985 Ap. J. **288** 618

Rodriguez, L.F., Moran, J.M., Ho, P.T.P. & Gottlieb, E.W. 1980
Ap. J. **235** 845

Ròzyczka, M. & Tenorio-Tagle, G. 1985 A.A. **147** 22

Rydbeck, G., Hjalmarson, Å& Rydbeck, O.E.H. 1985 A.A.
144 282

Sanders, D.B., Scoville, N.Z. & Solomon, P.M. 1985 Ap. J.
289 373

Sanders, D.B., Solomon, P.M. & Scoville, N.Z. 1984 Ap. J.

276 182

Sargent, A.I., Scoville, N.Z., Masson, C.R., Lo, K.Y.
         & Phillips, T.G. 1987 I.A.U. Symp. No. 115 *'Star*
         Forming Regions' p329

Sato, S., Nagata, T., Nakajima, T., Nishida, M., Tanaka, M.
         & Yamashita, T. 1985 Ap. J. **291** 708

Scarrott, S.M., Warren-Smith, R.F., Pallister, W.S., Axon, D.J.
         & Bingham, R.G. 1983 M.N.R.A.S. **204** 1163

Scarrott, S.M., Warren-Smith, R.F., Draper, P.W.
         & Gledhill, T.M. 1986 Can. J.Phys. **64** 426

Scarrott, S.M., Gledhill, T.M. & Warren-Smith, R.F. 1987a
         M.N.R.A.S. **227** 1065

Scarrott, S.M., Gledhill, T.M. & Warren-Smith, R.F. 1987b
         M.N.R.A.S. **227** 701

Scarrott, S.M., Gledhill, T.M., Warren-Smith, R.F.
         & Wolstencroft, R.D. 1987c M.N.R.A.S. **228** 533

Scarrott, S.M., Gledhill, T.M. & Warren-Smith, R.F. 1987d
         'Interstellar Magnetic Fields' ed. Beck, R.
         & Grave, R. 161

Scarrott, S.M., Warren-Smith, R.F., Wolstencroft, R.D.
         & Zinnecker, H. 1987e M.N.R.A.S. **228** 827

Schwartz, R.D. 1975 Ap. J. **195** 631

Schwartz, R.D. 1978 Ap. J. **223** 884

Schwartz, R.D. & Dopita, M.A. 1980 Ap. J. **236** 543

Schwartz, R.D. 1981 Ap. J. **243** 197

Schwartz, R.D. 1983a A.R.A.A. **21** 209

Schwartz, R.D. 1983b *Revista Mexicana de Astronomia y Astrofisica*
         7 27

Schwartz, R.D. 1985 *'Protostars and Planets'* II p405

Schwartz, R.D. 1986 Can. J.Phys. **64** 414

Scoville, N.Z., Sanders, D.B. & Clemens, D.P. 1986 Ap. J.
         (letters) **310** L77

Scoville, N.Z. & Solomon, P.M. 1974 Ap. J. (letters)
         187 L67

Scoville, N.Z. & Solomon, P.M. 1975 Ap. J. (letters)
         199 L105

Scoville, N.Z., Solomon, P.M. & Sanders, D.B. 1979 I.A.U. Symp.

No. 84 *'The Large Scale Structure of the Galaxy'* 277-283

Shibata, K. & Uchida, Y. 1987 I.A.U. Symp. No. 115
'*Star Forming Regions*' p385

Shirt, J.V. 1984 Ph. D. Thesis, Univ. of Durham

Shu, F.H. 1978 I.A.U. Symp. No. 52 '*Interstellar Dust
and Related Topics*' 257

Silk, J. 1983 '*Birth and Infancy of Stars*' 349

Smith, B.A. & Terrile, R.J. 1985 Science **226** 1421

Snell, R.L., Scoville, N.Z., Sanders, D.B. & Erickson, N.R. 1984
Ap. J. **284** 176

Snell, R.L. & Schloerb. F.P. 1985 Ap. J. **295** 490

Snell, R.L. 1987 I.A.U. Symp. 115 '*Star Forming
Regions*' p213

Solomon, P.M. & Wickramasinghe, N.C. 1969 Ap. J. **158** 449

Spitzer Jr. L. 1968 '*Stars and Stellar Systems*' **7** 1

Spitzer Jr. L. 1978 '*Physical Processes in the
Interstellar Medium*'

Spitzer Jr. L. & McGlynn, T.A. 1979 Ap. J. **231** 417

Strom, K.M., Strom, S.E. & Kinman, T.D. 1974 Ap. J.
191 L93

Strom, S.E., Strom, K.M. & Grasdalen, G.L. 1975 A.R.A.A.
13 187

Strom, K.M., Strom, S.E., Wolff, S.C., Morgan, J. & Wenz, M. 1986
Ap. J. Suppl. **62** 39

Taylor, K.N.R. & Scarrott, S.M. 1980 M.N.R.A.S. **193** 321

Tenorio-Tagle, G. & Ròzyczka, M. 1984 A.A. **137** 276

Torrelles, J.M., Rodriguez, L.F., Cantò, J., Carral, P.,
Marcaide, J., Moran, J.M. & Ho, P.T.P. 1983 Ap. J.
274 214

Torrelles, J.M., Ho, P.T.P., Rodriguez, L.F. & Cantò, J.
1985 Ap. J. **288** 595

Torrelles, J.M., Ho, P.T.P., Moran, J.M., Rodriguez, L.F.
& Cantò, J. 1986 Ap. J. **307** 787

Torrelles, J.M., Anglada, G., Rodriguez, L.F., Cantò, J.
& Barral, J.F. 1987 A.A. **177** 171

Turnshek, D.A., Turnshek, D.E. & Craine, E.R. 1980 A.J.
85/12 1638

Uchida, Y. & Shibata. K. 1985 P.A.S.J. **37** 515

Uchida, Y., Kaifu, N., Shibata, K., Hayashi, S.S. &
        Hasegawa, T. 1987 I.A.U. Symp. No. 115 *'Star Forming*
        Regions' p287

Vrba, F.J., Strom, S.E. & Strom, K.M. 1976 A.J. **81** 11

Vrba, F.J., Rydgren, R.E. & Zak, D.S. 1985 A.J. **90** 2074

Ward-Thompson, D.W., Warren-Smith, R.F., Scarrott, S.M.
        & Wolstencroft, R.D. 1985 M.N.R.A.S. **215** 537

Warren-Smith, R.F. 1979 Ph.D. Thesis, Univ. of Durham

Warren-Smith, R.F., Draper, P.W. & Scarrott, S.M. 1987a
        Ap. J. **315** 500

Warren-Smith, R.F., Draper, P.W. & Scarrott, S.M. 1987b
        M.N.R.A.S. **227** 749

Weber, E.J. & Davis, L. 1967 Ap. J. **148** 217

Wright, J.S. & MacKay, C.D. 1981 Proc. Soc. Phot. Inst. Eng. **290** 160

Zuckerman, B., Kuiper, T.B.H. & Rodriguez-Kuiper, E.N. 1976
        Ap. J. (letters) **209** L137